

Nanomechanical characterisation methods for cellulosic fibres

Nanomechanische Charakterisierungsmethoden für cellulosehaltige Fasern

Zur Erlangung des Grades: Doktor der Ingenieurwissenschaften (Dr. Ing.)
Genehmigte Dissertation von Julia Auernhammer (M.Sc.) aus Darmstadt

1. Gutachten: Prof. Dr. Robert W. Stark
2. Gutachten: Prof. Dr. Regine von Klitzing

Fachbereich Material- und Geowissenschaften
Fachgebiet Physics of Surfaces



TECHNISCHE
UNIVERSITÄT
DARMSTADT



Nanomechanical characterisation methods for cellulosic fibres
Nanomechanische Charakterisierungsmethoden für cellulosehaltige Fasern

Zur Erlangung des Grades: Doktor der Ingenieurwissenschaften (Dr. Ing.)
Genehmigte Dissertation von Julia Auernhammer (M.Sc.) aus Darmstadt

Tag der Einreichung: 05.10.2021

Tag der Prüfung: 10.12.2021

1. Gutachten: Prof. Dr. Robert W. Stark
2. Gutachten: Prof. Dr. Regine von Klitzing

Fachbereich Material- und Geowissenschaften
Fachgebiet Physics of Surfaces

Bitte zitieren Sie dieses Dokument als:

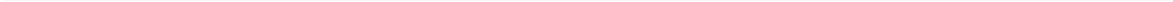
URI: <https://tuprints.ulb.tu-darmstadt.de/id/eprint/20198>

URN: urn:nbn:de:tuda-tuprints-201981

Dieses Dokument wird bereitgestellt von tuprints, E-Publishing-Service der TU Darmstadt

Die Veröffentlichung steht unter Creative Commons Lizenz:

CC BY-SA 4.0 international



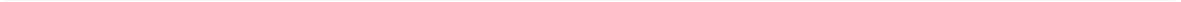
Erklärung zur Dissertation

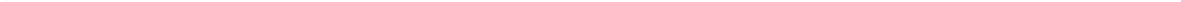
Hiermit versichere ich, die vorliegende Dissertation ohne Hilfe Dritter nur mit den angegebenen Quellen und Hilfsmitteln angefertigt zu haben. Alle Stellen, die aus Quellen entnommen wurden, sind als solche kenntlich gemacht. Diese Arbeit hat in gleicher oder ähnlicher Form noch keiner Prüfungsbehörde vorgelegen.

Darmstadt, den 13.12.2021



Julia Auernhammer





Abstract:

Paper is a material that has been used for thousands of years. It is made from natural and renewable raw materials. It consists of randomly distributed fibres that form a whole sheet of paper through their connections. Because paper is also recyclable and can be produced in large quantities, it is a promising substrate material for various applications such as sensor technologies or microfluidics. However, the technical application of paper is impeded by the loss of mechanical stability when paper comes into contact with moisture. Thus, the loss of mechanical properties must be understood under the influence of relative humidity and the wet strength must be improved. In this work, advanced atomic force microscopy-based methods are introduced to characterise the mechanical behaviour of cellulosic fibres under humid conditions. Furthermore, hydrophobic terpolymers are introduced as wet strength polymers and investigated as function of the relative humidity to show the enhancement of the wet strength of the cellulosic fibres.

At first, the mechanical properties of individual, freely suspended cotton linter fibres were investigated as a function of the relative humidity. Individual fibres were bent stepwise by static atomic force microscopic bending tests along the longitudinal axis with a colloidal probe. This created a detailed picture of the mechanical behaviour of the fibre as a function of the relative humidity. The data were evaluated in combination with confocal laser scanning microscopy and scanning electron microscopy. This enabled insights into the dependency of swelling, bending ability, contact stress, and stress-strain diagrams and the macroscopic fibril orientation on the fibre surface.

In addition, the intrinsic mechanical properties of cellulosic fibres were determined by force-volume mapping with atomic force microscopy. Here, the mechanical properties of unprocessed cotton fibres were compared with processed cotton linter fibres in the dry and wet state. By measuring the local elastic modulus as function of the fibre depth, the wall structure of the fibres could be assumed. The wall structure was also observed by dyeing the fibres with fluorescence-active protein markers using confocal fluorescence laser scanning microscopy. This allowed the investigation of the papermaking process and the removal of the upper layers. In addition, the influence of fibre wetting on the predicted wall structure was investigated.

Subsequently, the influence of the relative humidity on the mechanical properties of cotton linter and eucalyptus fibre bundles as well as single fibres was examined. In addition, the

effectiveness in improving the wet strength of a promising polymer coating (terpolymer P(S-co-MABP-coPyMa)) was determined. The polymer coating distribution was revealed with scanning electron microscopy and fluorescence microscopy. Contact angle measurements confirmed the hydrophobic character. With the help of Raman spectroscopy, it could be demonstrated that the amount of water that was absorbed differed between the coated and uncoated fibres. Static and quasi-static atomic force microscopy measurements revealed differences in the mechanical properties between the cotton linter and eucalyptus fibres and the polymer-coated fibres in different states of relative humidity.

In a last step, the stability of fibre-fibre joints was investigated *via* a static atomic force microscopy-based method. Through static force-distance curves and a high spring constant cantilever the fibre-fibre joints could be displaced and the maximum applied force was determined. Additionally, the relative humidity was varied to investigate the behaviour of the joints under these humid conditions. The maximum applied force on the fibre-fibre joint was related to the bonded area and the angle between the two fibres to identify the more characteristic parameter for fibre joint strength. Furthermore, a technology promising terpolymer coating P(DMAA-co-MABP-co-RhodBMA) was investigated to prevent softening of the joints with increasing RH. The polymer coatings were tested on a H₂O and an IPA solution basis and exhibited both an increase in fibre-fibre joint strength under dry and humid conditions.

Kurzbeschreibung:

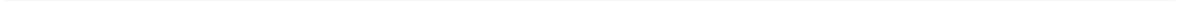
Papier ist ein seit Jahrtausenden genutztes Material, welches aus natürlichen und erneuerbaren Rohstoffen hergestellt wird. Es besteht aus zufällig verteilten Fasern, die durch ihre Verbindungen ein ganzes Blatt Papier formen. Dadurch, dass Papier zudem recyclebar ist und in großen Mengen produziert werden kann, ist es ein vielversprechendes Substratmaterial für verschiedene Anwendungen wie Sensortechnik oder Mikrofluidik. Die technische Anwendung von Papier wird jedoch durch den Verlust der mechanischen Stabilität, wenn Papier in Kontakt mit Feuchtigkeit kommt, erschwert. Dadurch muss der Verlust der mechanischen Eigenschaften unter Feuchte verstanden werden und die Nassfestigkeit verbessert werden. In dieser Arbeit werden fortgeschrittene Rasterkraftmikroskopie basierende Methoden vorgestellt, um das mechanische Verhalten von Cellulosefasern in feuchten Umgebungen zu charakterisieren. Darüber hinaus werden hydrophobe Terpolymere eingeführt und untersucht, um die Nassfestigkeit der Cellulosefasern zu verbessern.

Zunächst wurden die mechanischen Eigenschaften in Abhängigkeit der relativen Luftfeuchte von einzelnen Baumwollinters Fasern untersucht. Die freihängende Faser wurde durch statische Rasterkraftmikroskopische Biegeversuche entlang der longitudinalen Achse mit einer kolloiden Sonde Stück für Stück gebogen. Dadurch entstand ein detailliertes Gesamtbild des mechanischen Verhaltens der Faser in Abhängigkeit der Luftfeuchte. Die Daten wurden in Kombination mit konfokaler Laserrastermikroskopie und Rasterelektronenmikroskopie ausgewertet. So konnten Einblicke in die Abhängigkeit von Quellen, Biegefähigkeit, Kontaktspannung und Spannungs-Dehnungs Diagramme und der makroskopischen Fibrillenorientierung an der Faseroberfläche gewonnen werden.

Außerdem wurden mittels der statischen Kartierung (Force-Volume Mapping) in der Rasterkraftmikroskopie die intrinsischen mechanischen Eigenschaften von Cellulosefasern bestimmt. Hierbei wurden unverarbeitete Baumwollfasern mit verarbeiteten Baumwollintersfasern verglichen. Durch die Messung des lokalen E-Moduls in die Tiefe der Fasern konnte die Wandstruktur der Fasern angenommen werden. Die Wandstruktur wurde durch die Einfärbung der Fasern mit fluoreszenz-aktiven Markern mit der konfokale Fluoreszenz-Laserrastermikroskopie überprüft. So konnten der Papierherstellungsprozess und das Abtragen der oberen Schichten untersucht werden. Zudem wurde der Einfluss von der relativen Luftfeuchte auf die Wandstruktur der Fasern untersucht.

Danach wurde der Einfluss von relativer Luftfeuchte auf die mechanischen Eigenschaften bei Baumwolllinters und Eukalyptus Faserbündel und einzelnen Fasern untersucht, sowie die Effektivität einer Polymerbeschichtung (Terpolymer P(S-co-MABP-coPyMa)). Die Polymerbeschichtung wurde mit Hilfe von Rasterelektronenmikroskopie und Fluoreszenzmikroskopie sichtbar gemacht und Kontaktwinkelmessungen bestätigten den hydrophoben Charakter. Mit Hilfe von Ramanspektroskopie konnte nachgewiesen werden, dass die Menge von Wasser, die absorbiert wurde, Unterschiede zwischen den beschichteten und unbeschichteten Fasern aufwies. Die statische und quasi-statische Rasterkraftmikroskopie offenbarte Unterschiede in den mechanischen Eigenschaften zwischen den Linters- und Eukalyptus Fasern und den polymerbeschichteten Fasern in verschiedenen Zuständen der relativen Luftfeuchte.

Zuletzt wurde die Stabilität von Faser-Faser-Verbindungen untersucht. Über eine statische AFM-basierte Methode konnten die mechanischen Eigenschaften und die Festigkeit der Faserverbindungen untersucht werden. Durch statische Kraft-Abstands-Kurven und eine hohe Federkonstante konnten die Faser-Faser-Verbindungen auseinander gedrückt und die maximal aufgebrachte Kraft erfasst werden. Zusätzlich wurde die Variation der relativen Luftfeuchtigkeit einbezogen, um das Verhalten der Faserverbindungen in einer feuchten Umgebung zu untersuchen. Die maximal auf die Faser-Faser Verbindung ausgeübte Kraft wurde auf die Kontaktfläche und dem Winkel zwischen den beiden Fasern bezogen, um einen weiteren wichtigeren Parameter für die Festigkeit der Faserverbindung zu identifizieren. Darüber hinaus konnte gezeigt werden, dass neue Terpolymerbeschichtungen P(DMAA-co-MABP-co-RhodBMA) an den Faser-Faser-Verbindungen ein Aufweichen der Fugen bei steigender relativer Luftfeuchte verhindern. Die Polymerbeschichtungen werden auf H₂O- und Isopropanol-Lösungsbasis getestet. Beide Polymerbeschichtungen zeigten eine erhöhte Festigkeit sowohl im trockenem als auch in den Luftfeuchten Zuständen.



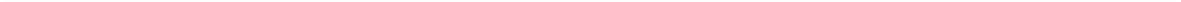


Table of contents

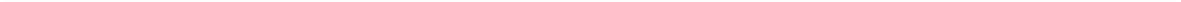
Table of contents	XIV
1 Introduction	1
2 Fundamentals	5
2.1 Paper	5
2.2 Cellulose	5
2.2.1 <i>Cellulose at the Molecular Level</i>	5
2.2.2 <i>Fibrillar Structure of Cellulose and Composition of a Fibre</i>	6
2.2.3 <i>Wet Strength of Cellulose</i>	9
2.2.4 <i>Increasing the Wet Strength of Cellulose</i>	9
2.2.4.1 <i>Terpolymer P(S-co-MABP-co-PyMA)</i>	11
2.2.4.2 <i>Terpolymer P(DMAA-co-MABP-co-RhodBMA)</i>	13
2.3 Cotton Linter and Eucalyptus Fibres	16
2.3.1 <i>Cotton Fibres</i>	16
2.3.2 <i>Eucalyptus Fibres</i>	16
2.4 Fibre-Fibre Joints	17
2.5 Sheet Formation Process	19
2.5.1 <i>Rapid Köthen Prozess for Sheet Formation</i>	19
2.6 The Atomic Force Microscope	21
2.6.1 <i>Working Principle</i>	21
2.6.2 <i>Interactions between Tip and Sample Surface</i>	23
2.6.3 <i>Description of the Cantilever Dynamics</i>	23
2.6.4 <i>Operating Modes in Atomic Force Microscopy</i>	25
2.6.5 <i>PeakForce-Tapping Mode</i>	26
2.6.6 <i>Force-Volume Mapping</i>	29
2.6.7 <i>Cantilever and Tip Geometries</i>	31
2.7 Confocal Laser Scanning Microscopy	32
2.7.1 <i>Working principle</i>	32
2.8 Raman Spectroscopy	33
2.8.1 <i>Working Principle</i>	33
2.9 Contact Angle Goniometry	35
2.10 Scanning Electron Microscopy	36
2.10.1 <i>Working Principle</i>	36

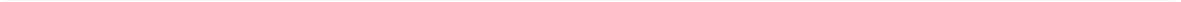
3	Mapping humidity-dependent Mechanical Properties of a Single cellulosic Fibre	41
3.1	Introduction	42
3.2	Materials and Methods	44
3.2.1	<i>Materials</i>	44
3.2.2	<i>Methods</i>	44
3.2.2.1	<i>Confocal Laser Scanning Microscopy</i>	45
3.2.2.2	<i>Atomic Force Microscopy</i>	46
3.2.2.3	<i>Estimation of Contact Area A and Elongation ΔL</i>	50
3.2.3	<i>Scanning Electron Microscopy</i>	54
3.3	Results and Discussion	55
3.3.1	<i>Fibre Geometry</i>	55
3.3.2	<i>Colloidal Probe Mapping</i>	57
3.3.3	<i>Determination of virtual Young's moduli</i>	62
3.4	Repeatability of the measurement technique	64
3.5	Conclusions	69
4	Nanomechanical Subsurface Characterisation of cellulosic Fibres	73
4.1	Introduction	74
4.2	Materials and Methods	76
4.2.1	<i>Materials</i>	76
4.2.2	<i>Methods</i>	76
4.2.2.1	<i>Atomic Force Microscopy</i>	76
4.2.2.2	<i>Scanning Electron Microscopy</i>	79
4.2.2.3	<i>Preparation of Recombinant His- and Fluorescence-Tagged Carbohydrate-Binding Proteins (CBMs)</i>	79
4.2.2.4	<i>3D Fluorescence CLSM Measurements</i>	80
4.3	Results and discussion	81
4.3.1	<i>Subsurface properties of dry fibres</i>	81
4.3.2	<i>Verification of fibre wall structure by fluorescent protein markers</i>	85
4.3.3	<i>Subsurface properties of hydrated fibres</i>	88
4.3.4	<i>Comparison of dry and wet state subsurface properties</i>	89
4.3.5	<i>Influence of tip geometry</i>	91
4.4	Conclusion	92

5	Nanomechanical Characterisation of a Water-repelling Terpolymer Coating of Cellulosic Fibres	95
5.1	Introduction	96
5.2	Materials and Methods	97
5.2.1	<i>Materials</i>	97
5.2.2	<i>Methods</i>	97
5.2.2.1	<i>Contact Angle Goniometry</i>	97
5.2.2.2	<i>Scanning Electron Microscopy</i>	97
5.2.2.3	<i>Fluorescence Microscopy</i>	97
5.2.2.4	<i>Raman Spectroscopy</i>	98
5.2.2.5	<i>Atomic Force Microscopy</i>	100
5.2.2.6	<i>Indentation Experiments</i>	100
5.2.2.7	<i>Nanomechanical mapping</i>	101
5.3	Results and Discussion	103
5.3.1	<i>Hydrophobicity of terpolymer P(S-co-MABP-co-PyMA)</i>	103
5.3.2	<i>Spatial distribution of the polymer coating</i>	104
5.3.3	<i>Water uptake in plain and polymer coated fibre bundles</i>	107
5.3.4	<i>Mechanical property changes in dry and humid states</i>	109
5.3.4.1	<i>Analysis via indentation experiments</i>	109
5.3.4.2	<i>Analysis via nano mechanical mapping</i>	112
5.4	Conclusion	119
6	Mechanical Characterisation of Plain and Polymer coated Fibre-Fibre Joints depending on the Relative Humidity	123
6.1	Introduction	124
6.2	Materials and Methods	126
6.2.1	<i>Materials</i>	126
6.2.2	<i>Methods</i>	127
6.2.2.1	<i>Contact Angle Goniometry</i>	127
6.2.2.2	<i>Confocal fluorescence microscopy</i>	127
6.2.2.3	<i>Atomic force microscopy</i>	127
6.3	Results and discussion	129
6.3.1	<i>Hydrophobicity and spatial distribution of the terpolymer P(DMAA-co-MABP-co-RhodBMA)</i>	129
6.3.2	<i>Stability of plain fibre-fibre joints depending on the RH</i>	131

6.3.3	<i>Relation of maximum force to bonding area and bonding angle</i>	133
6.3.4	<i>Stability of polymer coated fibre-fibre joints depending on the RH</i>	135
6.3.4.1	<i>Mechanical stability differences between H₂O- and IPA-based polymers</i>	135
6.3.5	<i>Comparison of stability of plain and polymer coated fibre-fibre joints</i>	137
6.4	Conclusion	139
7	Summary	141
8	Supplementary	146
8.1	Supplementary Information to chapter 3	146
8.1.1	<i>Supplementary Figures</i>	146
8.1.2	<i>Strategy for calculation the eccentricity</i>	147
8.1.3	<i>DMT moduli</i>	149
8.1.4	<i>Repeatability of measurement</i>	150
8.2	Supplementary information to chapter 4	152
8.2.1	<i>Force-distance curves with local fits</i>	152
8.2.2	<i>Imprints in force-volume mapping</i>	154
8.3	Supplementary Information to chapter 5	155
9	Table of Figures	159
10	List of Abbreviations	169
11	References	171
12	Publications	182
13	Curriculum Vitae	184
14	Acknowledgement	184







1 Introduction

Paper is a material, produced from renewable resources, which was used for thousands of years. It is a porous and flexible, but hardly elastic material, which is built up by randomly orientated fibre-like units which are connected to each other. One could assume, that paper is becoming out-dated a more and more digitalised world. However, the paper production is increasing. The worldwide consumption of paper in 2020 was 420 million tons. Compared to 1980 with 171 million tons of production volume, this corresponds to an increase in global consumption of more than 250 % (1, 2). In Germany only, a total of 22 million tons of paper, cardboard and paperboard were produced in 2020. This puts Germany in fourth place in a global comparison and into the leader position in Europe. Most of the 49 % is made up of packaging paper. The production volume of graphic papers is 38.4 % and that of hygiene and specialty papers 6.3 % each (3).

Additionally, the necessity for construction materials and functional materials made out of renewable resources puts paper in the focus of research. Paper is recyclable and can be produced in high amounts. Thus, it can be one of the most promising substrate materials in different fields of applications such as in electronics, sensor technologies, micro fluidic or medicine (4-10). For example, micro fluidic systems consists predominantly of silicon, glass or plastic. By the easy handling and the cost-efficient production of paper, it could be applied as carrier medium in “lab-on-a-chip” products. Since the fibres can be functionalised in a defined way, paper could be coated with hydrophobic polymers in such a manner that small channels are built on the sheet of paper. By the capillary attraction only, the fluid could be guided without external pumps. A crucial factor why cellulose based papers from plants such as cotton are of high research interest is that, in the long term, cellulose is the only renewable raw material that is directly available in sufficient quantities and does not have to be produced from other raw materials such as wood. The wood price was rising up by 70 %. The application of plant based cellulose supplies will definitely increase in the near future. These include applications in the construction area and especially packaging or in the building industry.

But, the use of paper as substrate material in technical applications is raising some challenge, for example, the production of paper from natural fibres or the loss of the mechanical stability in wet state. The main bonding mechanism between the fibres are supposed to be the hydrogen bonds. Also, fibre properties such as length, width, wall thickness, fibrillation degree, flexibility or the arrangement of the fibres in the paper sheet play an important role

for the bonding between fibres in the dry state. At increasing relative humidity (RH), the hydrogen bonds are weakened. The fibres begin to swell, they become more flexible and thus, the strength of the paper sheet is decreasing (11-18). Thus, the loss of mechanical properties in wet state has to be understood in detail. As paper is consisting of single fibres, the understanding of the reason for the loss of mechanical stability has to be built from bottom up. Therefore, this work is focussed on single fibres and fibre-fibre joints and their nano mechanical behaviour at dry state and increasing RH. However, for applications in which papers are already being used as so-called “wet-strength papers”, an understanding of fibre stability is of crucial interest, since the chemical modifications with which papers are made wet-strength must be replaced by biodegradable alternatives. A characterisation of the fibre stability is therefore a central component in order to promote the use paper as a sustainable material in as many tasks as possible in the future.

Furthermore, the challenge to improve the wet-strength has to be tackled. So far, Polyamidoarminepichlorohydrin resins (PAAE resins) are the most commonly used wet strength agents (19, 20). In addition to all the advantages of increasing strength in dry and wet conditions, PAAE resins in particular have some disadvantages. The use of paper-based products is to be expanded primarily from an ecological point of view, as the production is based on renewable raw materials and paper can be recycled. However, if a network of resins is introduced into the paper, the reusability is greatly reduced (17). In addition, by-products (such as organic halogen compounds) can also be absorbed by the paper. If these products enter the wastewater unfiltered, it causes severe environmental pollution (21). Thus, alternative polymers have to be investigated to increase the wet-strength of paper. A possible method to increase the wet-strength is the photothermal linking of hydrophobic terpolymers such as P (S-co-MABP-co-PyMA) or P(DMAA-co-MABP-co-RhodBMA) (22, 23). These terpolymers can be linked independently from the production process and can be deposited at any location, which reduces drastically the environmentally harmful of chemicals.

An excellent tool to study and characterise the physical properties of solid samples at the nano and micro scale is the atomic force microscope (AFM). The AFM is not only useful for imaging the topography, but also to quantify the mechanical properties. In AFM measurements it is possible to extract mechanical properties based on force-distance curves. These curves can be recorded in a static manner (force-volume mapping) or in a quasi-static manner (PeakForce-Tapping mode). Thus, mechanical properties such as elastic modulus, adhesion, dissipation and deformation of the sample at the nanoscale could be determined. Furthermore, from mapping with force vs. distance curves it is possible to reconstruct the

topography or mechanical properties such as the Young's modulus and the maximum indentation depth into the sample. Thus, a three-dimensional nanomechanical characterisation can be obtained. AFM measurements are not only limited to the use in dry conditions, also measurements in liquid or humid conditions can be accomplished at high resolution.

In this work, different advanced AFM-based methods are introduced, described and discussed to investigate the mechanical behaviour of cellulosic fibres. With the novel AFM-based analysis methods, paper fibres were investigated in dry, increasing RH and wet conditions. Hence, the loss of the mechanical properties is analysed and quantified in an improved way, which gives new insights in the wetting behaviour of fibres. Also, the prevention of the loss of mechanical stability by coating the fibre with the terpolymer (P (S-co-MABP-co-PyMA) and P(DMAA-co-MABP-co-RhodBMA) was demonstrated. The AFM measurements are supported and supplemented with confocal Raman microscopy, confocal laser scanning microscopy, confocal fluorescence microscopy and scanning electron microscopy to obtain a thorough mechanical image in combination with the microscopic observation of the fibre structure.



2 Fundamentals

2.1 Paper

Paper is consisting of cellulose, the most abundant bio molecule (24). It is a natural occurring material, mostly located in cell walls of plants and is recyclable. Thus, cellulose is the most important material in the paper production. Fresh wood fibres are used as the primary raw material in the production of paper. These are obtained by mechanical processing of fresh wood. In a chemical defibration process, the end product is called pulp. Recovered paper can be used as secondary fibres in paper production. In Germany, the use rate of recovered paper is 74 % (25). A pure paper production from recovered paper is not possible, because the fibres lose their ability to form sheets during processing and fresh fibres have to be added again and again to support this (26). The different types of paper can be produced using different paper or sheet-forming processes.

2.2 Cellulose

The mechanical properties or the strength of a paper are of enormous importance for later use. These properties are decisively determined by the proportion of cellulose within the individual paper fibres. Therefore, the molecular structure and the structure of a cellulose fibre are described below.

2.2.1 Cellulose at the Molecular Level

The molecular structure of cellulose consists of recurring units that are covalently linked to one another. The repeating units are referred to as D-anhydroglucopyranose units (AGE), these being linked to one another via acetal functions β -1,4-glycosidically. This means that the equatorial groups of a C4 atom and the C1 atom are thus covalently linked to each other (27). The repeat unit, which is made up of two AGEs, is called cellobiose. The molecular structure of cellulose is shown in Figure 1. The C1 and C4 atoms are marked in green.

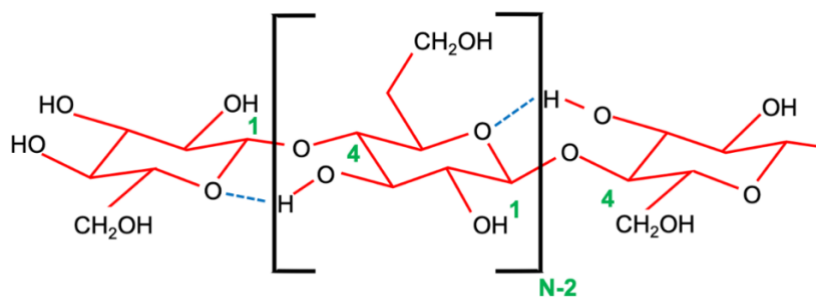


Figure 1: Molecular structure of cellulose. The hydrogen bonds are indicated in the dashed blue lines. N displays the degree of polymerisation.

As shown schematically in Figure 1, cellulose is a polydispersive, linear syndiotactic polymer that has a large number of hydroxyl groups. The degree of polymerization describes the length of the polymer chains and can be calculated from the number of AGEs. It is indicated by N in Figure 1. Typical degrees of polymerisation are 300–1700 in wood pulp or 800–10000 in cotton linter (27). Due to the linearity and the formation of hydroxyl groups between and within the chains, cellulose molecules are stiff and tend to parallel, crystalline arrangements (27-29). The cellulose polymer can occur in several allomorphs. Cellulose I is the natural form of cellulose that occurs naturally in plants or cell membranes. It has the highest relevance in papermaking. In addition, cellulose can adopt other crystal structures. Cellulose II can be produced through mercerization, i.e. chemical treatment with an aqueous solution of sodium hydroxide or solutions with semi-stable derivatives. In this form, the chains are not arranged parallel to each other, but antiparallel. Cellulose II is the most stable form as well as the most technically relevant form. There are other forms such as cellulose III, which is obtained through ammonia treatment, or cellulose IV, which is modified through thermal treatment. In all allomorphs, however, the molecular shape is retained, whereas the hydrogen network and the alignment of the molecular chains to one another are modified (27, 29, 30).

2.2.2 Fibrillar Structure of Cellulose and Composition of a Fibre

If a larger network is formed from the cellulose molecules, the highly ordered, linear chains can form a unit cell, which is surrounded by unordered areas. These unordered areas are known as amorphous cellulose. The fact that a polymer chain usually runs through successive crystalline and amorphous areas creates a strongly connected network of cellulose molecules. The crystallinity gives the ratio of crystalline to amorphous areas and varies depending on the type of preparation or origin. In the case of cotton seed hair, the crystallinity is approximately 70 %, in wood approximately 60 % and in regenerated cellulose only 40 % (31). If crystalline and amorphous areas are arranged, fibrillar structures develop. They are a few nano meters in diameter and a few micro meters long, which is why they are also called micro fibrils. If the microfibrils aggregate with each other, the macro fibrils form with a diameter of 60 - 400 nm and a length of a few millimetres (32). Together with hemicellulose, lignin, pectins or wax, these fibrils form the cell walls of plant fibres. The composition and structure of the fibres differ depending on the type of plant. Figure 2 shows a schematic representation of the cellulose molecules via the fibrillar structures to the paper fibre.

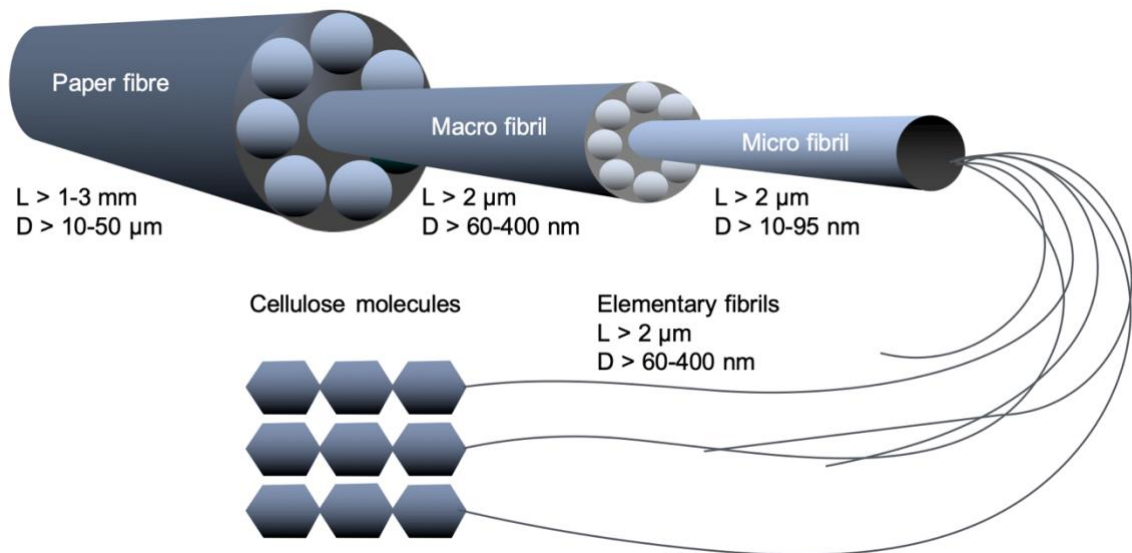


Figure 2: Schematic composition of a paper fibre. The elementary fibrils are formed by the cellulose molecules. They are connecting to microfibrils, which form together the macrofibrils. Those are forming the final paper fibre.

The individual paper fibres formed from the fibrillar structures have a hierarchical layer structure. This differs depending on the type of plant. As an example, Figure 3 shows a morphological structure of a cotton fibre.

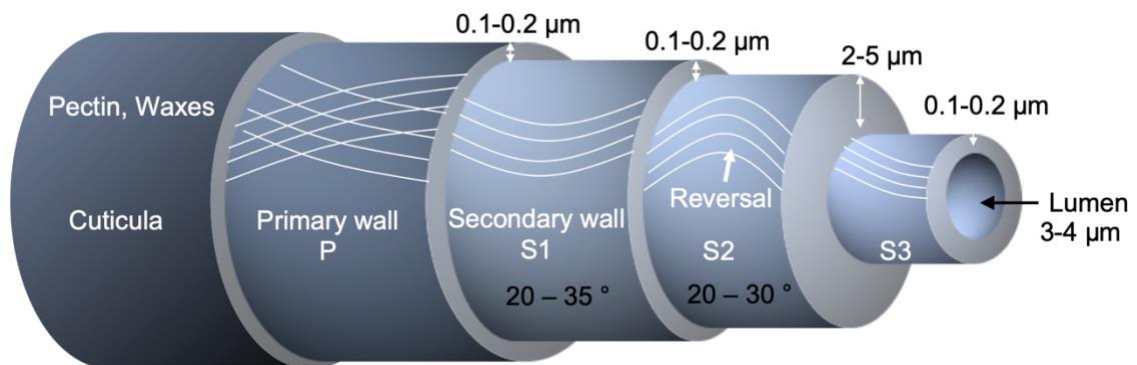


Figure 3: Schematic composition of the layer structure of a cotton fibre. The lines within the different layers represent the arrangement of the fibrils.

As shown in Figure 3, a cotton fibre has a central, hollow lumen. This is where the secondary walls S3, S2 and S1 are located. These are in turn surrounded by the primary wall. The cuticle is a waxy protective layer that is only a few molecules thick. Before the cotton fibre can be processed further, this layer must be removed. Directly below is the primary wall (P), which consists of cellulose fibrils. These are arranged in a spiral network around the fibre axis. The

P wall has a layer thickness of about 0.1-0.2 μm , is flexible and contains a high proportion of pectins, minerals and wax. This layer is often lost during the production of a paper. Below the P wall is the secondary wall, which is divided into three more walls. The secondary wall S1 is 0.1-0.2 μm and also has a high proportion of pectins, minerals and wax. The fibrils have a preferred direction here and are uniformly at an angle of 20° to the lumen. The most relevant layer of the fibre in papermaking is the secondary wall S2. A reversal of the fibril direction can be seen at the border with S1. The fibrils here also lie side by side in a preferred direction around the fibre axis. Due to its thickness of 1-5 μm , this wall represents 90 % of the fibre mass and is therefore decisive for the mechanical properties of the fibre. The S3 wall separates the lumen from the S2 wall and is 0.1-0.2 μm thick. The angle of the fibrils is 45° to the fibre axis. This alternating, spiral arrangement of the fibrils gives the fibre a high inherent resilience. During the growth of a fibre, the lumen is the pore through which sugar, proteins or minerals can pass. When the seed pod opens, however, the lumen dries up, leaving a hollow centre in the middle of the fibre (33-35).

In general, the physical properties of cellulose fibres are not only determined by the molecular structure or chemical composition, but mostly by the hierarchical structure just described. If the fibrils are arranged in a spiral around the fibre axis, the ductility of the entire fibre increases (13, 36). If the proportion of crystalline regions increases, the flexibility of the fibre decreases. The flexibility and stiffness are further influenced by the angle of the fibrils around the fibre (15, 34).

2.2.3 Wet Strength of Cellulose

Cellulose is insoluble in water and most organic solvents and is described as hygroscopic. Therefore, the mechanical properties decrease drastically when the fibres are brought into a moist state, since the fibres begin to swell (11, 12). The swelling process depends on the crystallinity, the degree of polymerisation, the degree of fibrillation and the size of pores within the cellulose fibre (13-18). It is considered a complex process. Because water molecules can diffuse through the pores from the fibre surface into the cell walls, the hydrogen bonds within the fibres are broken. The broken bonds are replaced with the solvent molecules, which leads to an expansion of the crystal structure. Therefore, the space between the fibrils is enlarged and swelling in the lateral direction is brought about. In the dry state, the distance between two fibres is approximately 1 nm, while in the wet state it increases to 1.2 - 5 nm (13, 37, 38). The swelling first takes place in disordered areas (39). If the RH is 50 %, so many bonds have already been broken or weakened that the strength is only 3-10 % compared to the original value (17).

2.2.4 Increasing the Wet Strength of Cellulose

Since cellulose and the associated produced paper products drastically reduce their strength and mechanical properties through the influence of solvents, wet strength agents are used to increase wet strength. This enables the use of paper products in new areas of application.

In industrial paper production, two main mechanisms are used to increase wet strength. The additives are introduced in dissolved form and then preferably collect at fibre-fibre intersection points. This is also known as the "webbed effect". The mechanisms of the "Protection Mechanism" and the "Reinforcement Mechanism" are shown in Figure 4. In the "protection mechanism", the wet strength agent forms covalent bonds with itself during thermal crosslinking. This is known as homo crosslinking. The cross-linking points are indicated in light blue in Figure 4. The formed network thus protects the fibres and the points of intersection against penetration of water and the associated reduction in strength properties. Most of the wet strength agents used here are based on formaldehyde (40). In the "reinforcement mechanism", the wet strength agent can, in addition to homo-crosslinking, also form covalent bonds to the carboxyl groups of the fibres. This is known as co-crosslinking. Because the polymer chains are now linked to each other and to the fibres, a more stable network is formed. The associated increase in strength can be seen in both dry and wet conditions. Polyamidoaminepichlorohydrin resin (PAAE resin) is one of the most commonly used wet strength agents in this mechanism (19, 20).

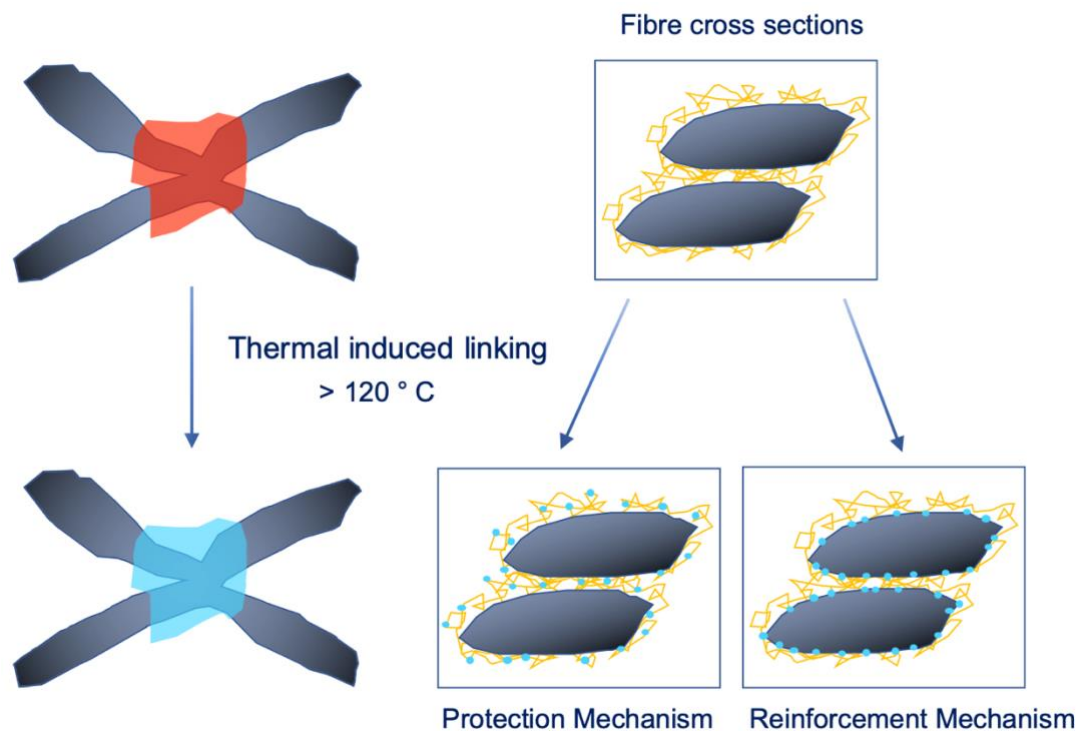


Figure 4: Mechanisms for increasing the wet strength of cellulose. The wet strengthening agents is presented in red before the thermal induced linking and in light blue afterwards. The linking points in the protection mechanism and in the reinforcement mechanism are indicated in blue.

In addition to all the advantages of increasing strength in dry and wet conditions, PAAE resins in particular have some disadvantages. The use of paper-based products is to be expanded primarily from an ecological point of view, as production is based on renewable raw materials and paper is also recyclable. However, if a network of resins is introduced into the paper, the reusability is greatly reduced (17). In addition, when paper is made with PAAE resins, by-products (such as organic halogen compounds) can also be absorbed in the paper. If these products enter the wastewater unfiltered, this causes severe environmental pollution (21). The resins also have a disadvantage from an economic point of view. The water created during crosslinking must first be removed again to dry, but must be added again later for better storage of papers. Therefore, this is associated with a high energy input (41). The use of resins also restricts the possible applications. The current research on the possible uses of paper is mainly based on the "lab-on-a-chip" model. To improve the sensitivity in microfluidic papers is also part of our PAK62 project (C02). For this purpose, paper test strips should function as a "laboratory" in medical tests and provide evidence of pathogens (4-9). Functional groups or antibodies are applied to the surface of the paper. Bringing in and accessing the groups is almost impossible when resins are used as wet strength agents. Therefore, alternative crosslinking options are being sought in order to increase the wet strength of the papers.

2.2.4.1 Terpolymer P(S-co-MABP-co-PyMA)

An alternative to wet strength agents is the hydrophobic terpolymer P(S-co-MABP-co-PyMA) (23). It consists of three monomer units. The polystyrene (PS) is the bulk polymer and ensures the hydrophobicity. The MABP unit is photoreactive and provides with its benzophenone units the crosslinking to the cellulose molecules. The polymer is also covalently bound to the cellulose fibres by means of homo-crosslinking and reinforcement crosslinking through UV irradiation (42, 43). The 1-pyrenemethyl methacrylate (PyMA) unit is fluorescence active and is used for the investigation of the distribution of the polymer.

Böhm et al. developed the synthesis of the polymer as part of his dissertation and showed the application potential of the photo lithographic micro structuring (44). Via this method they implemented channel structures inside paper substrates and investigated the capillary driven fluid transport. They observed a linear relationship between the covered distance of the fluid and the square root of the time. Furthermore, the influence of the fibre type, of the weighted area of the paper substrate and of the width of the implemented channel on the flux rate (45). *Wendenburg et al.* did further research in her dissertation on the retention of different model analytes to optimise the sensibility and specificity of μ PAD systems (23). In that way they provided a first platform for the control of the retention as proteins in papers. *Bell et al.* examined papers for wet strength with the terpolymer P(S-co-MABP-co-PyMA) by Raman spectroscopy. Here, a hydrophobicity of the papers coated with the polymer was demonstrated (46).

The reaction scheme and the representation of the terpolymer P(S-co-MABP-co-PyMA) is shown in Figure 5.

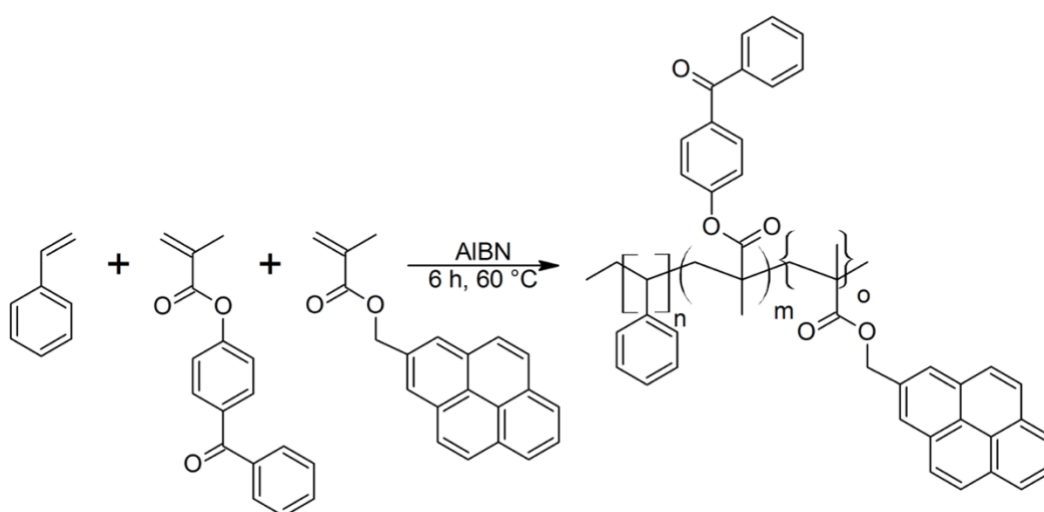


Figure 5: Reaction scheme and representation of the terpolymer P(S-co-MABP-co-PyMA).

The free radical block polymerization took place according to Böhm and was carried out by Sonja Wendenburg, Department of Macromolecular and Paper Chemistry, TU Darmstadt (47). The compositions used for the copolymerization are listed Table 1.

Table 1: Used masses for copolymerisation of P(S-co-MABP-co-PyMA).

Chemical	mg
PS	7.87
MABP	533
PyMA	121
AIBN	38.7

The MABP and PyMa portions were placed in a Schlenk flask. The PS and AIBN were added under an N₂ atmosphere. The yellow-colored solution obtained was then degassed by freezing-vacuum-roughening three times. After stirring for six hours at 60 ° C, the solution became viscous. The reaction was then stopped by adding 30 mL tetrahydrofuran (THF) and then placed in an ice bath. 600 mL of methanol was added dropwise to the polymer solution. The polymer was dried in vacuum until a constant weight was reached.

2.2.4.2 Terpolymer P(DMAA-co-MABP-co-RhodBMA)

Jocher researched an alternative hydrophobic polymer to increase the wet strength of papers in his dissertation (22). He used a copolymer with photoreactive groups. The terpolymer consisted of 3 monomers N, N'-dimethylacrylamide (DMAA), 4-methacryloyloxybenzophenone (MABP) and rhodamine B methacrylamide (Rhod B MA). The photoreactive co-monomer MABP carries benzophenone side groups which, when exposed to UV light, can form cross-links within the polymer through homo-crosslinking and also connection to the cellulose fibers through co-crosslinking. *Jocher* investigated the influence of the irradiation time, the influence of the mass fraction of the polymer in relation to the dry weight of the paper and the influence of the molar fraction of the photoreactive groups in the polymer. It was found here that an increase in wet strength could be achieved through UV irradiation, but no further increase in strength could be achieved after a certain period of time. This could also be found in the influence of the mass fraction of the polymer in relation to the dry weight of the paper. The molar proportion of the photoreactive groups in the polymer could not be assigned any far-reaching influence. By means of fluorescence microscopy it could be shown that the polymer mainly accumulates on the fibrils of the fibers as well as on the crossing points. To make this visible through fluorescence, *Janko et al.* the polymer around the Rhodamine B methacrylamide (Rhod B MA) unit (11). The polymer system was further investigated by *Schäfer* in 2018 with regard to the questions regarding the influence of pre-swelling and the use of different solvents on the tensile strain curves. In addition, the local connection of the copolymer in the fiber braid and on the fiber was made visible (48). It was found that when the polymer was dissolved in water, it accumulates in the lumens and in the fiber walls. When the polymer was dissolved in isopropanol, it could only be observed between the fibers. It was therefore interpreted that the local attachment of the polymer has a strong influence on the tensile strengths of the paper.

The reaction scheme of the terpolymer P(DMAA-co-MABP-co-RhodBMA) is displayed in Figure 6.

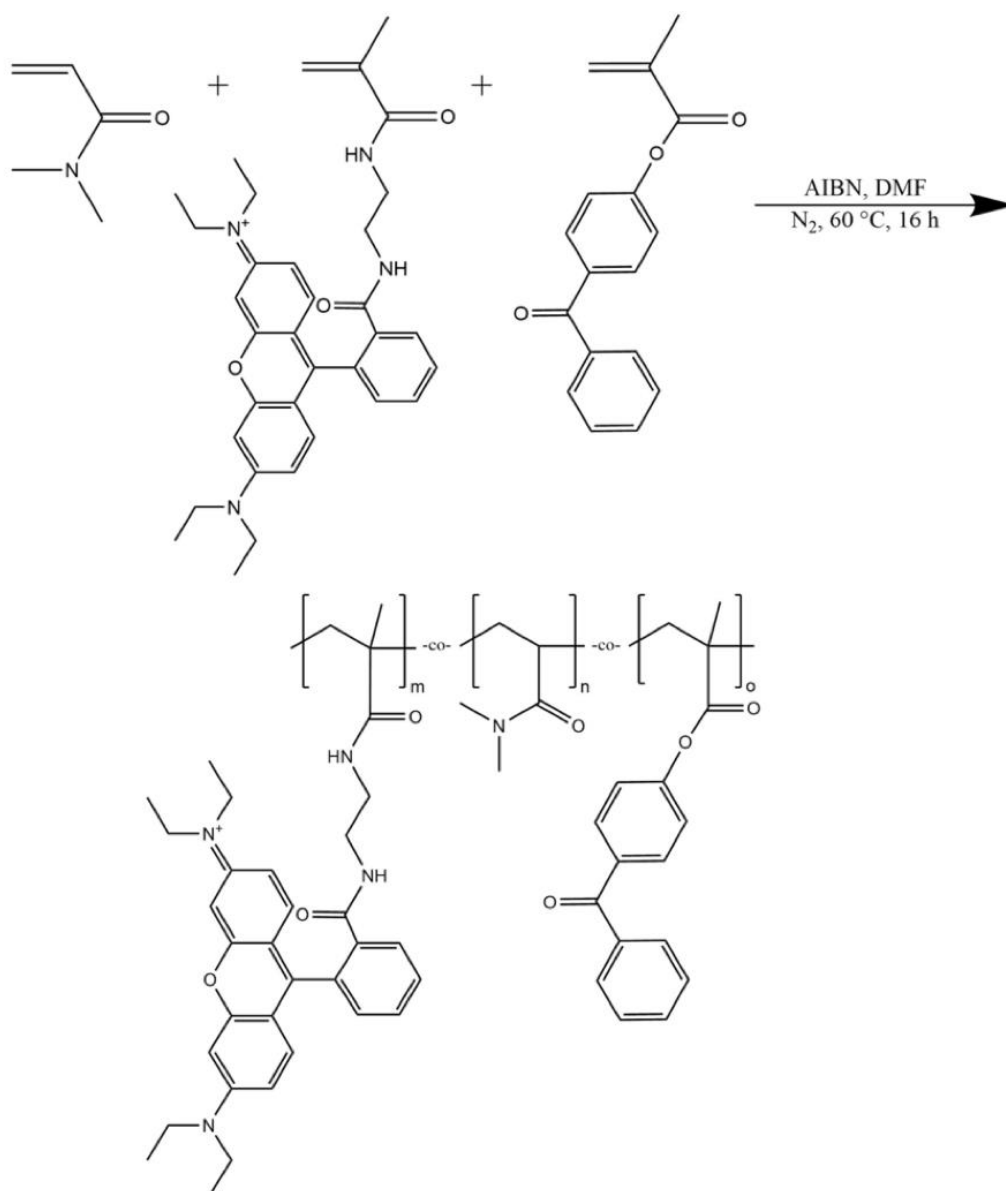


Figure 6: Reaction scheme and representation of the terpolymer $P(S\text{-}co\text{-}MABP\text{-}co\text{-}RhodBMA)$.

The free radical solution polymerization was carried out according to *Böhm* and was carried out by *Jan-Lukas Schäfer*, Department of Macromolecular and Paper Chemistry, TU Darmstadt (47). The used masses for the copolymerisation are listed in Table 2.

Table 2: Used masses for copolymerisation of P(DMAA-co-MABP-co-RhodBMA).

Chemical	g/mol	g/mL	mg	mL	mmol	mol%
DMAA	99.13	0.962	3960	4.11	39.9	97.79
MABP	266.30	-	213	-	0.8	1.96
Rhod B MA	553.73	-	53.4	-	0.1	0.25
AIBN	164.21	-	40	-	0.12	-

The proportions of MABP, Rhod B MA, DMAA and AIBN were dissolved in ~ 30 mL dimethylformamide (DMF) in a Schlenk flask with stirring. The mixture was then degassed by freeze-vacuum-roughening three times. The reaction was then started under an N₂ atmosphere in an oil bath at 60 °C. The reaction was ended after 16 hours, since the reaction mixture was stuffed into 600 mL diethyl ether. The pink polymer precipitate formed was decanted off and then precipitated twice from 50 mL chloroform. The precipitate was left to dry overnight at 40 °C. in a vacuum cabinet. The polymer was stored in the refrigerator until used.

2.3 Cotton Linter and Eucalyptus Fibres

The fibres examined in this work are cotton linter and eucalyptus fibres. Therefore, the properties of the respective fibres are explained below

2.3.1 Cotton Fibres

Cotton fibres typically have a length of 20-45 mm, a diameter of 12-22 μm with a wall thickness of 2.5-6 μm . The fibre has a flat, flattened shape. The lumen has a flat, bean-shaped shape. Due to its dimensions, the cotton fibre, which is obtained directly from the cotton plant, is suitable for the textile industry. The much shorter cotton linter fibres are used for paper production. These linter fibres also grow in the cotton plant but are not suitable for weaving textiles due to their short length. The cotton seed boll is processed in an oil mill. This uses rotating knives that separate the linter fibres. This is followed by an alkaline digestion, which removes accompanying substances or lignin and hemicellulose (49). The cotton linter fibres consist of almost pure cellulose and therefore serve as a reference. *Mather, R. et. al.* and *Young, R. et. al.* describe the composition of cotton fibres as 94-95 % cellulose and 5-6 % impurities (34, 37). Pectins and waxes are mostly found as impurities in the fibre. The length of a linter fibre is 2-6 mm with a diameter of 17-27 μm . The wall thickness is given as 6-12 μm . The fibre is cylindrical in shape and has a curled surface. The lumen has a round shape (35).

2.3.2 Eucalyptus Fibres

Eucalyptus fibres belong to the group of hardwoods. Here, the cellulose content is about 42 %. The remaining part consists of other accompanying substances, hemicelluloses and lignins. The cellulose is embedded in an amorphous matrix of hemicelluloses and lignins. The hemicellulose is bound to the cellulose by hydrogen bonds and serves as a supporting matrix. Furthermore, hemicellulose is not crystalline and has a hydrophobic character. The lignin increases the stiffness of the fibre due to the hydrophobic network formed. It is also amorphous. Therefore, the eucalyptus fibre is a much more complex system compared to the cotton linter fibres. The other accompanying substances are removed from the wood digestion using a sulphate process (Kraft pulping). The disadvantage of this process is that the cellulose chains can start to break down and therefore reduce the degree of polymerization, which affects the fibre properties (1, 34, 37). The length of eucalyptus fibres is given as 0.7-0.84 mm in the literature. The diameter is 18-19 μm (50, 51).

2.4 Fibre-Fibre Joints

The description of mechanical properties of paper is difficult due to the very high number of fibres and the complex geometry. The strength of a paper is largely determined by the number of fibre-fibre connections, the strength and distribution of the connections and the contact area between the connections. Lindström et al. describe the most important bonding mechanisms as mechanical entanglements, hydrogen bonds, electrostatic interactions, interdiffusion and induced dipoles (52). Furthermore, it is assumed in the literature that capillary bridges, micro-compressions or the pressure during drying also play a role in the strength of fibre-fibre connections (53-55). Which of the various mechanisms now plays the most dominant role is still unclear.

The mechanical interlocking, i.e. the bonds between the individual fibres, occurs on the micrometer scale. The fibrils hook or intertwine on the two surfaces, which leads to an increase in strength. It can be increased by beating. Unbeaten fibres often cannot form strong paper if they are not mixed with other pulps (53). The mechanical interweaving also includes the size of the contact area between the individual fibres. This can also be increased by striking it (53, 56, 57). Figure 7 shows a schematic of a fibre-fibre connection. It can be seen here that a distinction must be made between the visible and the molecular contact surface. The visible contact area is the top view of the fibre-fibre connection. This area is shown in yellow in Figure 7. The real area that is in contact between the two fibres is called the molecular contact area. This is shown in red in Figure 7. It depends on the modulus of elasticity of the wet fibre in the drying process, the roughness of the surface and the pressure applied during sheet formation (55, 58). Hydrogen bonds and van der Waals bonds are formed in this contact area, since the two fibre surfaces are brought closer than 1 nm together. The determination of the exact molecular contact area is considered difficult, but can be carried out by polarized light microscopy (59) and microtomography (60). Thomson et al. determined the degree of the molecular contact area with the help of Förster Resonance Energy Transfer (FRET) to 10 - 100 Å² (61).

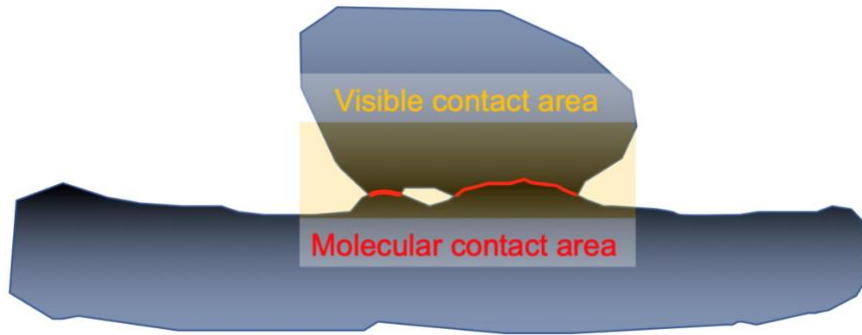


Figure 7: Schematics of the contact area between two fibres. It is divided in visible and molecular contact area. The visible contact area is marked in yellow and the molecular contact area in red.

The contribution of interdiffusion to the bond strength depends on the contact area. During the wet state in sheet formation, polymer chains spread from one surface to the other surface. Therefore, the mechanism of interdiffusion can be seen as a multiplier of the molecular binding mechanisms such as hydrogen bonds, van der Waals bonds or Coulomb interactions. Whether the hydrogen bonds or the van der Waals bonds are more relevant is still unclear in the literature. While theoretical studies attach more importance to the van der Waals bonds between cellulose molecules (62-65), experimental studies support the thesis that higher polarity between the bonds promotes strength (66). This could lead to the assumption that hydrogen bonds are more relevant (67), which has long been considered the most important binding mechanism (68). The more carboxyl groups there are on the fibre surface, the greater the bond between the two fiber surfaces, since the Coulomb interactions are attractive.

In 2015 *Hirn und Schennach* quantified the different bonding mechanisms (65). The results are shown in Table 3. Additionally, *Rohm et al.*, *Schmied et al.* und *Stratton et al.* characterised the binding energy between cellulose fibres. The values are displayed in Table 4.

Table 3: Energies of the different bonding mechanisms.

Bonding mechanism	Energy for an individual bond [kJ]
Van der Waals	6.8×10^{-24}
Hydrogen Bond	1.9×10^{-23}
Coulomb	1.2×10^{-20}

Table 4: Bonding energies between two fibres.

Author	Bonding energy
Rohm et al. (56)	$0,8 \pm 0,2 \times 10^{-22} \text{ kJ/nm}^2$
Schmied et al. (69)	$10^{-10} - 12^{-12} \text{ kJ/Bond}$
Stratton et al. (70)	$10^{-16} - 10^{-10} \text{ kJ/Bond}$

2.5 Sheet Formation Process

The sheet formation process is around 2000 years old and has hardly changed to this day. The random arrangement of vegetable fibres and accompanying substances creates a network known as paper (71). The fibres are initially in a suspension (pulp suspension) that is drained and pressed through a sieve. The fibres are first deposited on the sieve, then the water is drained off. Through the subsequent pressing, the fibres connect with each other and form intersection points with each other. The liquid bridges between the fibres are reduced by the drying and thus the capillary forces are increased, which pulls the fibres together. In this way the network is mechanically linked. This is called the Campbell effect (72). Depending on the properties of the individual fibres, the finished paper has different mechanical properties. If the fibres have a high degree of flexibility, strong fibre-fibre connections with large contact areas are formed. If the fibres also have high individual fibre strength, the fibres interlock mechanically and a strong leaf structure is created (73).

2.5.1 Rapid Köthen Prozess for Sheet Formation

All experiments were carried out on laboratory papers made from cotton and eucalyptus cellulose. Jan-Lukas Schäfer, Faculty of Macromolecular and Paper Chemistry, TU Darmstadt was responsible for producing the papers. Production was carried out in accordance with DIN EN ISO 5269-2 with a "Rapid Köthen" sheet forming system. Round sheets with a basis weight of 80 g / m² and an average weight of 2.51 g are produced. Cellulose cardboard is torn into 1 x 1 cm pieces and swollen in 1.5 L deionized water for 24 h. The pulp was comminuted at 75.000 revolutions by a HAAGE whipper (regulations V / 4/61 of the Association of Pulp and Paper Chemists / Engineers, ISO 5263 compatible). These steps were omitted for the cotton pulp, as this was supplied directly by the manufacturer in suspension. Then water was added until the desired pulp concentration was reached. Before starting the sheet formation, a test sheet was produced in order to check the calculated basis weight for a sheet. The amount of pulp was then transferred from the tank to the HAAGE Sheet Former BBS (DIN EN ISO 5269-2 (DIN 54 358) compatible). This is where the leaf was formed. The leaf former was then filled

up to 7 L with water and the content was "swirled" and "calmed down" for 5 seconds each. The water could be drained from the sieve by "falling through" until the leaf was recognizable. The sheet was further dehydrated using a vacuum system. Then a "Gautsch card" was placed on the sheet and fixed with a DIN / ISO roller. The paper could be removed from the sieve by lightly tapping a rubber plate and a cover sheet was placed on the paper. This was then dried under reduced pressure and at 93 ° C. for 10 minutes. In order to determine the grammage, the paper was then weighed and the oven weight was determined. The paper was stored at 23 ° C and 50 % RH until use.

2.6 The Atomic Force Microscope

The atomic force microscope (AFM) was firstly presented in 1968 by Binnig, G. et al. [67]. It belongs to the category of the scanning probe microscopes (SPM). In general, SPMs consist of a sharp tip that scans the sample line by line while the interactions between the surface and the tip are detected and a feedback system that controls the scanning process. The SPMs also include the Scanning Tunneling Microscope (STM) (74), which characterizes a surface using a tunnel current between the tip and the surface, and the Scanning Nearfield Optical Microscope (SNOM) (75), which is detected by light through extremely thin glass fibres. Under certain circumstances, atomic resolution can be achieved in AFM measurements.

2.6.1 Working Principle

One advantage of AFM compared to other SPM methods is that insulating and very soft samples can also be examined. Furthermore, electrical or magnetic properties can also be recorded. All measurements can be carried out in air, vacuum and liquid. A schematic set up of an AFM is shown in Figure 8.

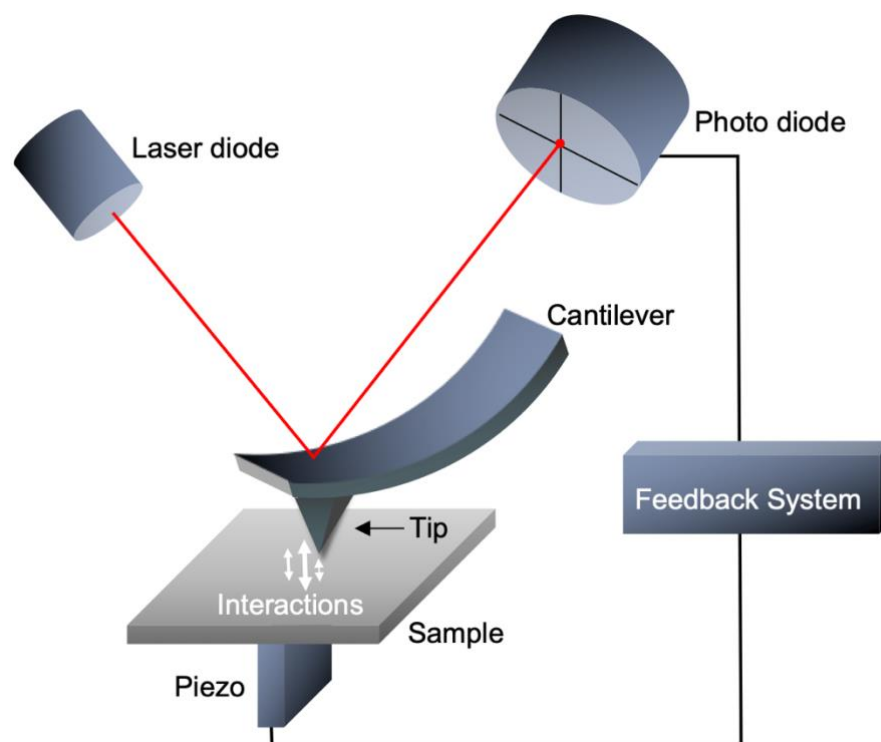


Figure 8: Schematic set up of an atomic force microscope (AFM).

The set up of an atomic force microscope in Figure 8 shows a laser diode, a sample, a cantilever with a sharp tip, a four-segment photodiode, a feedback system, and a piezo element for an x, y, z Movement of the sample and the cantilever. The working principle behind the AFM is to detect the interactions between the tip and the surface atoms of the sample. For this purpose, the laser beam is focused on the back of the cantilever, which is directed onto the four-segment photodiode by means of applied reflective materials. In the rest position, the laser beam hits the exact centre of the photodiode, which induces the same proportion of current in each segment due to the photoelectric effect. When interactions between tip and surface are detected, the cantilever bends and the laser beam changes its position on the photodiode. Therefore, a different proportion of current is now induced in each segment. The difference in the induced current is detected. The difference between the upper and lower segment is an indicator of the vertical bending of the cantilever and is used to record the topography. The difference between left and right is described as an indicator of the lateral forces acting on the tip. The evaluated signal from the photodiode is processed further in the feedback. The feedback mechanism is shown schematically in Figure 9.

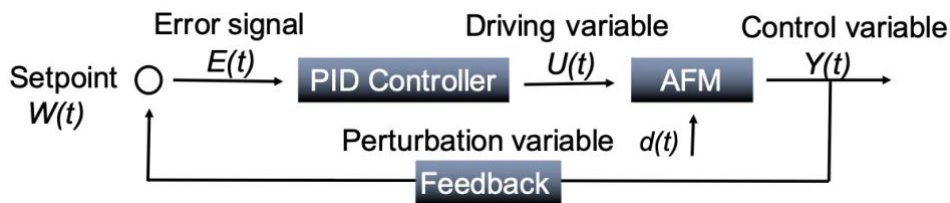


Figure 9: Mode of operation of the feedback mechanism.

The difference between the control variable $Y(t)$ and the setpoint $W(t)$ is controlled by the feedback mechanism. It minimizes the error signal $e(t)$ that occurs. A desired setpoint is set. If an error signal $e(t)$ occurs, the PID controller (proportional, integral and differential) produces a voltage $U(t)$ in order to control the z-movement of the crystal with the piezoelectric effect in order to readjust the height of the cantilever. The proportional part (P) multiplies the time-dependent error signal $e(t)$, while the integral part (I) integrates the error signal over time. One possible disturbance variable $d(t)$ can be the topography of the sample surface. Without the feedback mechanism there would be a large variation in amplitude or frequency, which would lead to incorrect and erroneous measurements.

2.6.2 Interactions between Tip and Sample Surface

The interactions between the tip and the sample surface can be classified into long-range and short-range forces. Pauli repulsion, covalent, metallic and ionic bonds as well as van der Waals forces (all attractive forces) and Coulomb repulsion are among the short-range forces. There is no coulomb repulsion on an electrically neutrally charged surface. The tip only perceives the induced or permanent dipole moments. Capillary forces are also present in measurements in air. The water vapor in the air condenses in the area of the tip and the surface, which leads to the formation of a water meniscus between the tip and the sample surface. How attractive the capillary forces are is defined by the air humidity. Magnetic and electrostatic forces, which can be either attractive or repulsive, belong to the long-range forces (76). An overview of the long- and short-range forces is given in Figure 10.

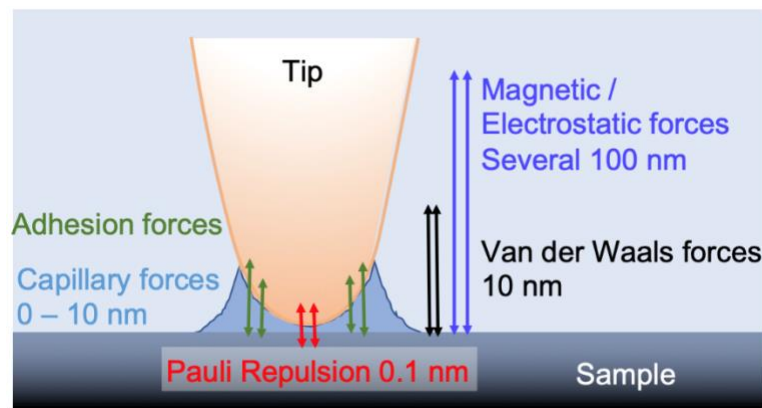


Figure 10: Schematics of long- and short range forces between the tip and the sample surface.

2.6.3 Description of the Cantilever Dynamics

The cantilever dynamics can be described by a spring constant mass system. The spring constant is denoted by k . Hook's law describes the deflection Δx proportional to the acting force F , as given as

$$F = k \cdot \Delta x \quad (1)$$

There are two common ways of determining the spring constant k . The first method is called the "Sader Method" (77). For this purpose, the cantilever geometry (width w and length L), the density of the fluid $\rho\rho_f$, the hydrodynamic function depending on the Reynolds number $\Gamma_i(\omega_0)$, the resonance frequency $\omega\omega_0$ and the Q-factor Q of the oscillation in the fluid must be specified. The spring constant is calculated according to Sader as

$$k = 0.1906 \cdot \rho_f \cdot w^2 \cdot L \cdot Q \cdot \Gamma_i(\omega_0) \cdot \omega_0^2 \quad (2)$$

The second method is the "thermal noise method" (78). Here the cantilever oscillates without external force only through Brown's molecular motion. The thermal energy is transferred to the spring (the cantilever). The method is based on the principle of equal distribution

$$\frac{1}{2} k_B T = \frac{1}{2} k \langle z^2 \rangle \quad (3)$$

and

$$k = \frac{k_B T}{\langle z^2 \rangle} \quad (4)$$

Here, T displays the temperature, k_B the Boltzmann constant, and $\langle z^2 \rangle$ the integrated area of the power spectral density over the frequency, as shown in Figure 11.

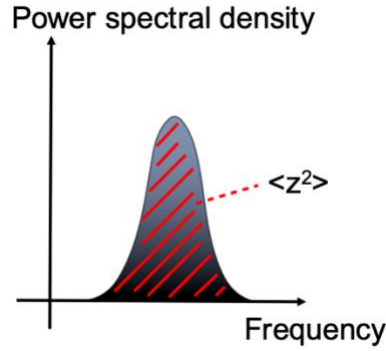


Figure 11: Power spectral density plotted over the frequency.

The cantilever motion can be described as a forced harmonic oscillator. The associated differential equation is defined as

$$m \cdot \ddot{x} = -k \cdot x - \frac{m \cdot \omega_0}{Q} \cdot \dot{x} + F_0 \cdot \cos(\omega t) + F_{ts}(x) \quad (5)$$

The first term on the right describes the spring force, the second term the damping behavior in the hydrodynamic medium (Q : Q-factor, m : mass, resonance frequency ω_0). The third term defines the excitation of the cantilever with the frequency ω and F_{ts} the non-linear tip-surface forces. A cantilever can be excited acoustically, magnetically or photothermally. The Q-factor describes the damping behavior of a harmonic oscillator. In liquids it is 5-10, while in air it is > 100 . The definition of the Q factor is given in

$$Q = \frac{\omega_0}{\Delta\omega} \quad (6)$$

2.6.4 Operating Modes in Atomic Force Microscopy

The operating modes in atomic force microscopy can be divided into static and dynamic modes. Static modes include constant altitude and constant force modes. The tip either detects the interactions with the surface at a constant height during the scanning process, whereby the feedback system is switched off, or the tip is in constant contact with the surface while the force between the tip and the surface is kept constant by the feedback system. The disadvantages of these modes are the large lateral forces that occur during the measurement. The dynamic modes were developed to minimize the lateral forces. Here the cantilever tip system is excited to oscillate close to the resonance frequency. A distinction is usually made between the amplitude-modulated mode and the frequency-modulated mode. The frequency-modulated mode is also called non-contact mode. Here the frequency shift is used as a feedback signal. The frequency shift contains information about the conservative forces, while the excitation amplitude is a measure of non-conservative (dissipative) forces. In the amplitude-modulated mode (tapping mode), the amplitude is considered a feedback signal. The cantilever is excited to a certain free amplitude. When the tip approaches the surface, the interacting forces dampen the oscillation of the amplitude. Due to the variations in the phase of the exciting force and the reaction of the tip, it is possible to make phase contrasts of the surface visible. The phase shift is similar to the energy dissipated between the tip and the surface during an oscillation cycle. If the dissipated energy is plotted against the normalized amplitude, it is possible to visualize the dissipation processes between stiff and soft materials. In this way, differences in the composition of a sample can be mapped directly (79-81).

2.6.5 PeakForce-Tapping Mode

The quasi-static mode represents a modification of the amplitude-modulated mode. Here the cantilever is excited to a certain amplitude far below the resonance frequency. The tip is in periodic contact with the surface and exerts a force (peak force) on the surface during the scanning process. In this way, several force-distance curves are generated at each contact point, since the bending of the cantilever represents a measure of the instantaneous force. These curves are averaged so that the feedback system can use the deviation to set the travel path of the piezo. The control variable represents the force (PeakForce). Therefore, precisely defined forces can be exerted on the surface through the tip. A typical force-distance curve is shown schematically in Figure 12. The frequency is usually 2 kHz and the peak force amplitude is 150 - 300 nm (82). The mode is also called “PeakForce Tapping Mode” or “PeakForce Quantitative Nanomechanical Mapping (PFQNM)” and was first introduced by Bruker in 2006 (83, 84).

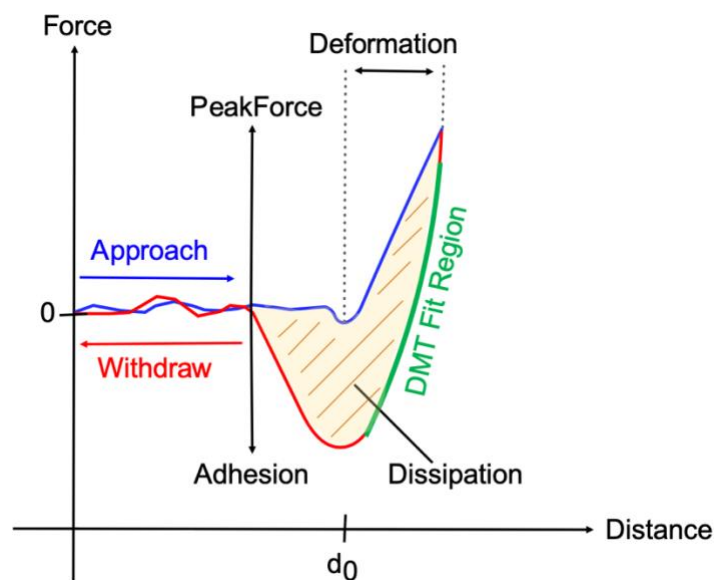


Figure 12: Schematics of a force-distance curve with mechanical properties.

In Figure 12, the blue line represents the characteristics during the approach of the tip towards the surface and the red line that during the retraction of the tip. When the tip approaches the surface, a “snap-into-contact” point occurs at a certain distance near the surface (d_0). Here the attractive force gradient is greater than the spring constant of the cantilever and the tip snaps into the surface. Then the set PeakForce is applied to the surface. When the Setpoint PeakForce has been reached, the tip is pulled back from the surface. An adhesive force now occurs between the tip and the surface. During the raster process, a force-distance curve is created at each contact point as shown in Figure 12. Further mechanical

properties of the surface can be read from this curve. The elastic properties can be described by the Derjaguin-Müller-Topotov (DMT) model (85). The green line in Figure 12 outlines the DMT Fit area. The DMT model incorporates adhesive forces outside the mechanical contact surface. The deformation resembles the Hertz contact model (86). Both models are shown in Figure 13.

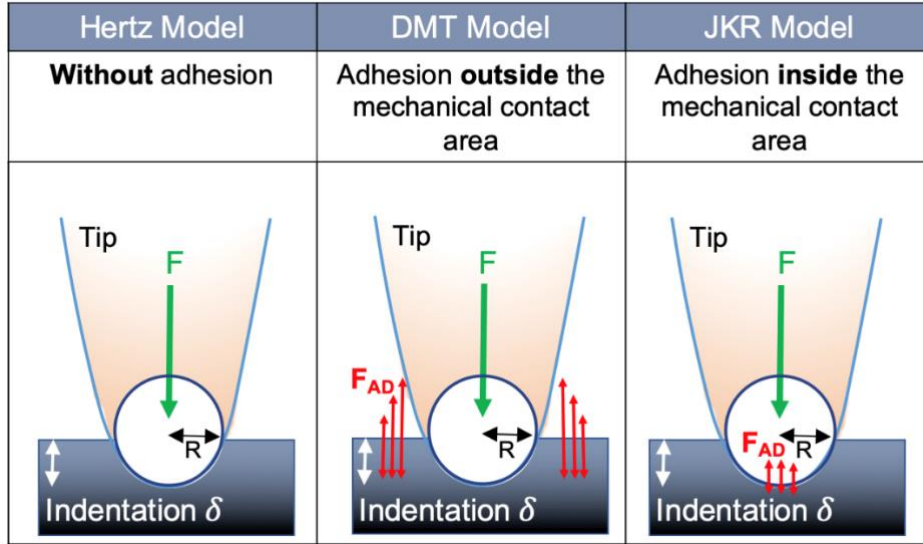


Figure 13: Contact mechanics of the Hertz model, DMT model and JKR model. F is the applied force, F_{AD} the adhesion force and R the tip radius.

The fit of the DMT model contains the interactions between surface and tip and is defined as

$$F_{DMT} = \frac{4}{3} E^* \sqrt{R} \delta^{\frac{3}{2}} + F_{ad} \quad (7)$$

F_{DMT} is the interacting force between surface and tip, E^* the reduced modulus of elasticity, R the tip radius, δ the indentation and F_{ad} the adhesion force. The reduced modulus of elasticity is extracted from the DMT module Fit and is defined as

$$E^* = \left[\frac{1 - \nu_s^2}{E_s} + \frac{1 - \nu_t^2}{E_t} \right]^{-1} \quad (8)$$

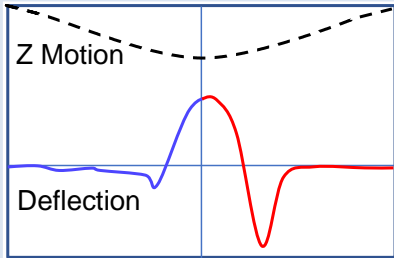
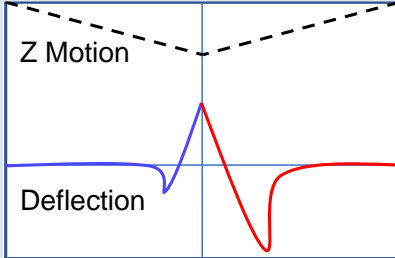
Here the Possion number ν_s , E_s is the E-module of the surface, respectively ν_t and E_t the Possion number and E-module of the tip. From the force-distance curve, the DMT module, the adhesion between tip and surface and the dissipation (enclosed orange area between the approach curve and the retraction curve in Figure 12) can be determined.

There are also other models of contact mechanics. The JKR (Johnson, Kendall and Roberts) model also describes the deformation like the heart model, but includes adhesion forces within the contact area (87). This is also shown in Figure 13. This model is valid for attractive forces between solids with a small modulus of elasticity. The JKR model is imprecise for materials with a high modulus of elasticity, as the adhesive forces are masked by the roughness of the surface. For bodies with high deformability and low elasticity, the surface roughness becomes negligible and the JKR model becomes more accurate. The DMT model can be used for high E-modules, small adhesion energies and small indentation radii (88).

2.6.6 Force-Volume Mapping

It is also possible to statically record the force-distance curves. In contrast to the PeakForce Tapping mode, the cantilever is not excited to vibrate, but remains static. While in PeakForce Tapping mode the amplitude is usually a few hundred nanometers and the cantilever and tip are therefore in permanent proximity to the surface, the cantilever is removed several μm from the surface when retracting in static force-distance curves. The advantage of measuring in the PeakForce Tapping mode is the speed of a measurement, as well as the simultaneous recording of the maps of the mechanical properties and the topography. The disadvantage is that the force-distance curves are not saved as individual curves, since this is often not technically offered by the manufacturers. However, on the basis of the individual force-distance curves, independent of the software used, further contact models can be used to fit the contact area or mechanical properties can be represented locally and with depth resolution (89). In order to obtain an extended method to characterize the sample mechanically both in the lateral direction and locally and with depth resolution in the z-direction, a map can be created using static force-distance curves (force-volume mapping). A volume mapping is thus possible by mapping force-distance curves. A brief overview of both modes can be seen in Table 5.

Table 5: Comparison between PeakForce Tapping and Force-Volume Mapping.

PeakForce Tapping	Force-Volume Mapping
	
<p>Sinusoidal ramping (not linear): \Rightarrow no piezo resonance ringing</p>	<p>Linear ramping: abrupt turn-around at maximum force \Rightarrow piezo resonance ringing</p>
<p>Real feedback loop force control: benefits from prior curves \Rightarrow no overshoot</p>	<p>Discrete force triggers at each ramp: reverse at trigger. At high speeds: can't resolve fast enough \Rightarrow overshoot</p>
<p>Best force control for high ramp rates</p>	<p>Best force control force control for low ramp rates</p>
<p>Fast ramping (kHz) \Rightarrow faster images, even with more pixels</p>	<p>Slow ramping (<kHz) \Rightarrow Slow speed of recording and evaluation</p>
<p>No storage of the individual force-distance curves</p>	<p>Application of advanced models for fit of \Rightarrow Contact point or contact mechanics</p>
<p>Simultaneous creation of maps of the topography and mechanical properties</p>	<p>Can be developed to a local and depth-resolved method</p>

2.6.7 Cantilever and Tip Geometries

The cantilever tip system makes it possible to detect surface or subsurface properties in the nanometer range. The cantilever or tip geometries should be adapted to the respective application. On the one hand, the mode used (static or dynamic) and the surrounding medium (air, liquid, vacuum) play a role, and on the other hand, the surface properties of the sample (hard or soft material). For this purpose, the elasticity, the geometry, the resonance frequency, the spring constant and the material of the cantilever should be selected appropriately (90). Since small steps cannot be detected due to intrinsic bending, hard materials are predominantly used as tip materials. Silicon oxide or silicon nitride are usually used. The geometry of the tip largely determines the resolution of the AFM measurement, since the area of the tip-sample interaction depends on the tip radius (91). It is also possible to replace the tip with a colloidal probe of micrometer size. The advantage here is the precisely defined contact area between the colloidal sample and the surface. The cantilever materials are also predominantly SiO_2 or Si_3N_4 (92).

Table 6: Display and description of the used cantilever and tip geometries.

Colloidal Probe	Triangular Geometry Probe
<p>Use: Chapter 3</p>  <ul style="list-style-type: none"> • Defined contact area between colloidal probe and surface • <u>Used mode:</u> Static force-distance curves 	<p>Use: Chapter 5</p>  <ul style="list-style-type: none"> • Sharp tip for high resolution • High force control • <u>Used mode:</u> PeakForce Tapping Mode

High Force Constant Cantilever	High Aspect Ratio Tip	Tipless Cantilever
<p>Use: Chapter 4</p>  <ul style="list-style-type: none"> • High force can be applied, which leads to a high indentation depth • <u>Used mode:</u> Force-Volume Mapping 	<p>Use: Chapter 4</p>  <ul style="list-style-type: none"> • Small tip opening angle • Specific indentation • <u>Used mode:</u> Force-Volume Mapping 	<p>Use: Chapter 6</p>  <ul style="list-style-type: none"> • Planar contact area • <u>Used mode:</u> Static force-distance curves

2.7 Confocal Laser Scanning Microscopy

The confocal laser scanning microscope (CLSM) is a specialised light microscope. In opposite to the conventional light microscopy not the whole sample is illuminated, but only a small light spot on the sample surface. The sample is then scanned point by point and the light intensities of the reflected or fluorescence light are detected successively. Via an aperture plate in the beam path only light from the focussed spot can pass and light from other plains are blocked. Thus, three dimensional images can be created non-destructively.

2.7.1 Working principle

The working principle in CLSM is the confocal principle. The confocal principle was patented in 1957 Marvin Minsky. In Figure 14 the schematic set up of the confocal principle is shown. The emitted laser light (in blue) is focussed on the excitation pinhole to create a light point which can be focussed on the sample surface. The beam is then split by a semipermeable mirror (white light) or by a dichroitic mirror (fluorescence light). The objective produces a reduced image of the excitation pinhole. The reflected/fluorescence light is marked in red in Figure 14. The light is reflected to the pinhole in front of the detector. The pinhole blocks the out-of-focus light, that means light above and beneath the focus plane. Thus, only light from the focus plane can reach the detector. Thus, the point in the middle of the pinhole and the illuminated spot on the surface are confocal to each other. That means they are in focus simultaneously. By the massive reduction of the stray light a high resolution in z-plane can be obtained. This makes the execution of optical sectioning and the three-dimensional representation of the sample possible. In CLSM the sample is scanned line by line via the movable mirror system.

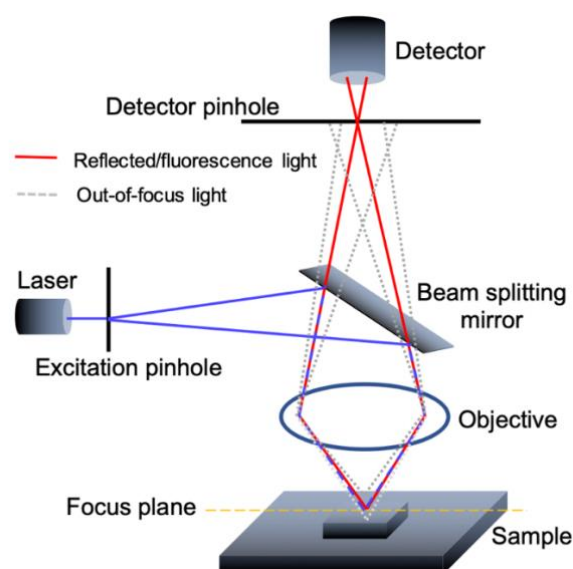


Figure 14: Schematics of the confocal principle in a confocal laser scanning microscope.

2.8 Raman Spectroscopy

Raman spectroscopy is a non-destructive analysis technique to obtain information about the chemical structure, molecular interactions or crystallinity. The Raman effect was discovered and identified in 1928 by Raman and Krishnan (93). They observed that an inelastic scattering of light results in a shift of the wavelength between an incident and scattered photon (94). In Raman spectroscopy incident light is focussed on a surface and scattered by the surface molecules. The change in wavelength of the scattered light is detected.

2.8.1 Working Principle

The Raman spectrometer can work in ambient conditions as solids, solutions and gases can be analysed. The setup is schematically shown in Figure 15. The monochromatic laser beam excites the sample. Typically, the laser wavelength is in IR or UV wavelength range. The secondary irradiation is then detected *via* a CCD camera or dispersive detector. The laser path beam in Figure 15 is shown in green. The change in dipole moment is induced by the polarised excitation laser.

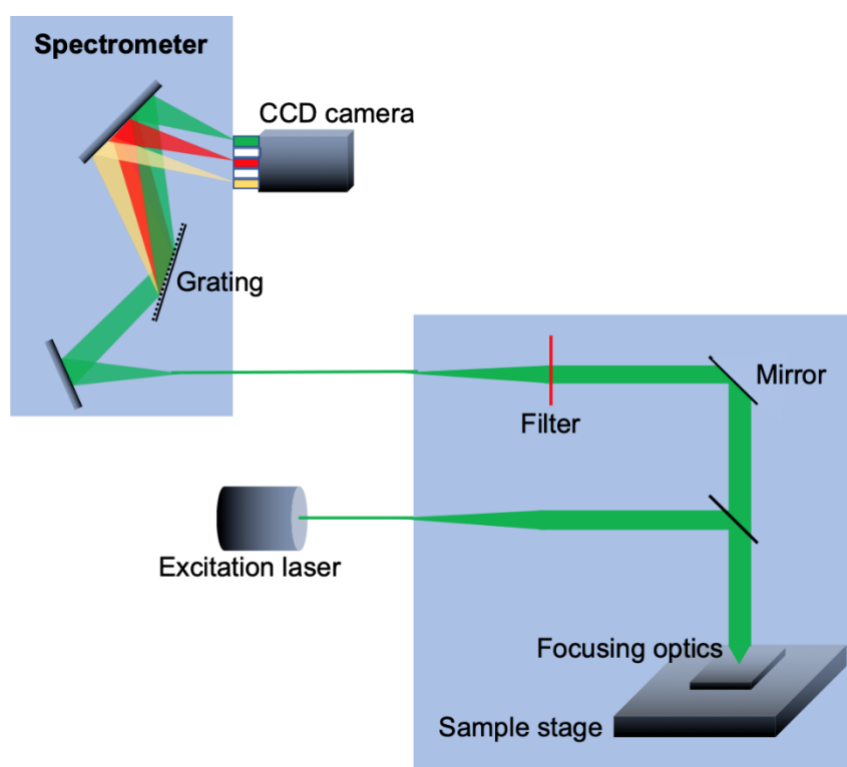


Figure 15: Set up of a Raman spectrometer and beam path. The laser beam path is shown in green.

As the laser beam hits the sample surface, the laser photons are scattered by the sample molecules. The scattering processes of the incident photons can be divided into elastic and inelastic scattering processes. The scattering processes are shown in Figure 16. The elastic scattering is called Rayleigh scattering. The incident and the scattered photons have the same wave length. This results in a Rayleigh peak at 0 cm^{-1} and has the highest intensity as the most of the photons are scattered elastically. When a photon is scattered inelastic the photon changes its wavelength after the scattering process. This results in a shifted Raman peak in the spectrum. The Stokes scattering of photons results in positive wavenumbers, as the scattered photons remain in a higher vibrational state. In Anti-Stokes scattering the photons remain in a lower vibrational state, which results in negative wavenumbers. The Anti-Stokes scattering occurs less frequently than the Stokes scattering. The resulting Raman shift depends on energy and wavelength of the incident and scattered photon as

$$\Delta E = E_{\text{virtual state}} - E_{\text{vibrational state}} = h f \quad (9)$$

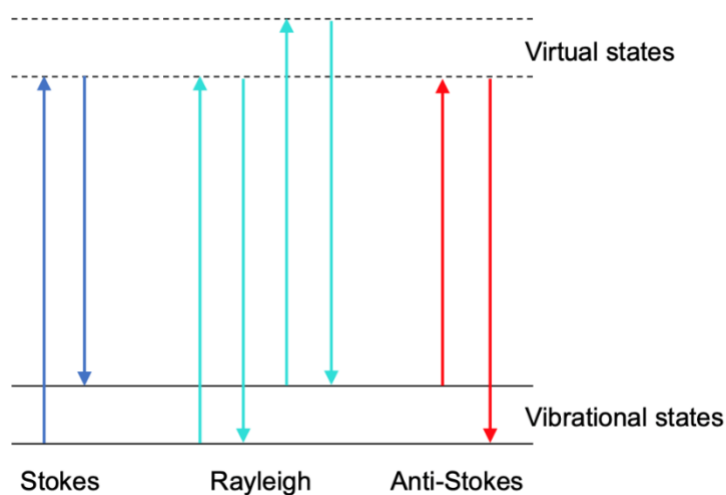


Figure 16: Scattering processes in Raman spectroscopy. In blue the inelastic Stokes scattering is shown. The elastic Rayleigh scattering is shown in turquoise and the inelastic Anti-Stokes scattering shown in red.

However, not every molecule reacts similar to an incident radiation. The secondary radiation depends on the polarisation, molecule symmetry and the dipole moment. But also, the possibility of a vibrational motion within the molecule is important for a Raman signal. In opposite to IR spectroscopy, in Raman spectroscopy the vibrational motions without a change of the centre of symmetry in a molecule is detected. The intensity of the Raman spectrum depends on the physical state of the sample, as the intensity decreases with decreasing volume. Thus, solutions or solids show higher intensities as gases. The spectrum consists of Raman bands, which are characteristic of every molecule bond.

2.9 Contact Angle Goniometry

With the contact angle θ , formed on the three-phase boundary between the liquid, gas and the solid, it is possible to extract a quantitative measure of the wettability of the solid surface by a liquid. The Youngs-Laplace equation

$$\gamma_{LG} \cos(\theta) = \gamma_{SG} - \gamma_{SL} \quad (10)$$

includes the interfacial tensions such as γ_{LG} (interfacial tension between liquid and gas), γ_{SG} (interfacial tension between solid and gas) and γ_{SL} (interfacial tension between solid and liquid). The contact angle θ is measured as a tangent line on the three-phase boundary. This is schematically shown in Figure 17.

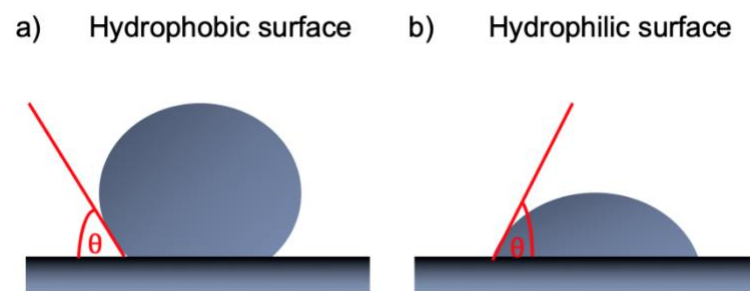


Figure 17: Schematics of the interaction of a liquid drop with a hydrophobic surface in a) and a hydrophilic surface in b).

Surfaces with a contact angle higher than 90° are called “hydrophobic” surfaces, see Figure 17a). When the contact angle is lower than 90° , the surfaces are characterised as “hydrophilic” surfaces, see Figure 17b). The contact angle not only depends on the composition of solid surface, but also on its physical properties such as roughness or homogeneity.

2.10 Scanning Electron Microscopy

The scanning electron microscopy (SEM) is an imaging technique to obtain images at higher resolution than conventional light microscopy. The technique and apparatus were firstly introduced by Max Knoll and Ernst Ruska in 1931. The first commercial electron microscope was produced by Ruska in 1938 (95). In SEM electrons are accelerated towards the sample surface and the deflected or knocked off electrons are detected to create an image of the surface *via* a scanning motion. As the electron wavelength is much smaller than the wavelength of light, higher resolutions can be obtained.

2.10.1 Working Principle

In general, the SEM needs to work under high vacuum conditions. Otherwise, the electrons can interact with other molecules and are thus reflected, which reduces the image quality. The electrons are generated by an electron source. This can be done by a thermionic field emission source (LaB₆ crystals) or field emitters like fine tungsten needles. A schematic set up of a SEM is shown in Figure 18. The electrons are emitted if the thermic energy of the electrons is higher than the work function of the source material. Then, the electrons are accelerated and attracted by a positively charged anode. The acceleration voltage can be several 10 kV. The condenser lens converges the beam before the cone opens again and defines the size of the electron beam, which defines the resolution. The objective lens converges the beam once more before the beam hits the sample. Via the scan coils the scanning motion is accomplished.

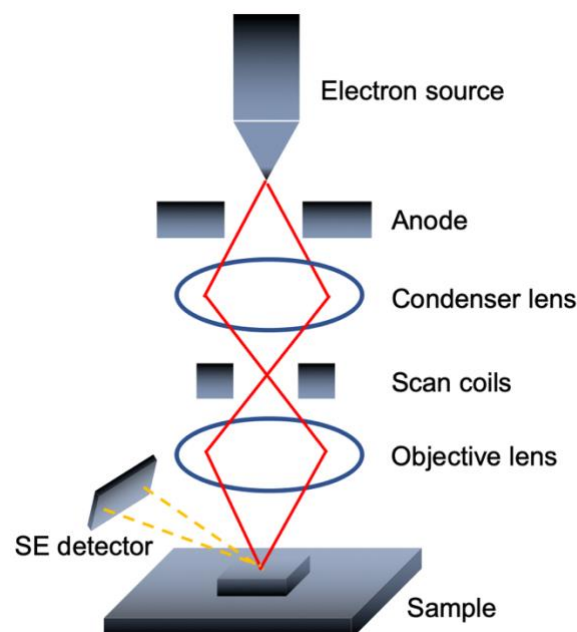


Figure 18: Schematic set up of an SEM.

When the electrons hit the sample surface they interact with the sample atoms in different depth up to 1 μm . Thus, different types of electrons, photons and irradiations are occurring. In SEM mostly, the secondary electrons (SE) and the backscattered electrons (BSE) are detected. In Figure 19 a schematic excitation bulb with the different interactions and areas where they originate is shown. Auger electrons are generated up to 2 nm depth. The SE are generated up to 5 nm depth. They originate from atoms of the sample due to inelastic scattering. Via SE it is possible to obtain surface information. In a depth of up to 100 nm the BSE are generated. They originate from the primary electron beam and are backscattered after elastic interactions. Because of the different depth, where the electrons originate, different information can be obtained. The BSE exhibit differences in atomic number where a brighter image means a higher atomic number. Furthermore, it is possible to an energy-dispersive X-ray spectroscopy (EDX) with the material characteristic released X-rays. In that way it is possible to obtain information about the atoms in the sample. To obtain the crystal structure an electron backscatter diffraction (EBSD) method can be used.

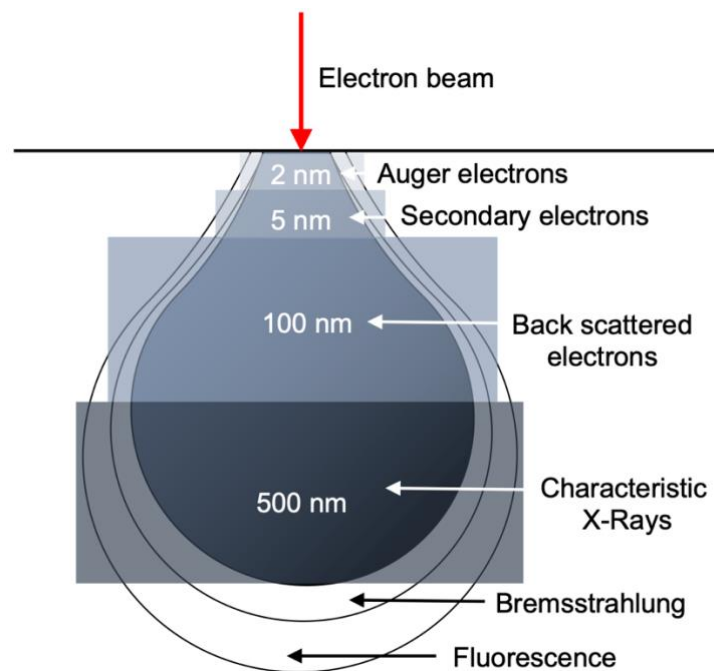


Figure 19: Excitation bulb and different types of interactions with the electron beams and the area where they originate.







3

Mapping humidity-dependent Mechanical Properties of a Single cellulosic Fibre

At first, an AFM-based analysis method via static force distance curves for single fibres is described and discussed. Here, the humidity-dependent mechanical properties of a whole single cellulose fibre are analysed in a stepwise manner.

Usually, the modelling of single cellulose fibres is usually performed by assuming homogenous properties, such as strength and Young's modulus, for the whole fibre. Then, the inhomogeneity in size and in swelling behaviour along the fibre is often disregarded. Thus, a more detailed characterisation of the fibre is required. Herein, an AFM-based method to map these properties along the fibre is described. A single fibre was mechanically characterised by static colloidal probe AFM measurements along the longitudinal direction of the fibre. Thus, the contact stress and strain at each loading point could be extracted and stress-strain curves were obtained along the fibre. Additionally, mechanical properties such as adhesion or dissipation were mapped. Local variations of the effective fibre radius were recorded via CLSM. SEM measurements revealed the local macroscopic fibril orientation and provided an overview of the fibre topography. By combining these data, regions along the fibre with higher adhesion, dissipation, bending ability and strain or differences in the contact stress when increasing the relative humidity could be identified. This combined approach allows to obtain a detailed picture of the mechanical properties of single fibres.

Parts of this chapter have been published as:

"Mapping humidity-dependent mechanical properties of a single cellulose fibre" by Auernhammer, J., Keil, T., Lin, B. *et al.* in *Cellulose* **28**, 8313–8332 (2021).
<https://doi.org/10.1007/s10570-021-04058-4>

3.1 Introduction

Paper can be used as substrate material for various “lab on paper” applications (4-10) without knowing the exact mechanical properties. The most used effect here is the intrusion of a fluid into a paper substrate by its hygroscopy and thus, without external pumps. However, to access even more fields of applications such as paper-based actuators or to develop specific improvements such as an alignment of fibres within a paper sheet an understanding of how the mechanical properties of single cellulosic fibres depend on the structure its variations and inhomogeneities must be improved. In pulping and paper making, the flexibility of a single fibre plays an important role. Flexibility is responsible for quality during sheet formation and production of types of papers (55). To control this process, characterisation of the processed fibres is important.

The Young’s modulus is a mechanical parameter that can be used to describe a single fibre. In tensile tests, a Young’s modulus between 20 and 80 GPa was measured for single fibres (96-99). *Via* an AFM-based three-point bending test, the Young’s modulus of a single pine fibre could be quantified to 24.4 GPa (100). Large variations in the Young’s moduli of different fibres are due to the different types of fibres, such as earlywood vs latewood, and botanical aspects, such as cell wall thickness or fibre width. Additionally, the micro fibril angle plays an important role in the single fibre strength. A small micro fibril angle was shown to be correlated with a high longitudinal elastic modulus (101).

The parameter of bending stiffness is defined as the Young’s modulus multiplied by the second moment of inertia (102). The bending stiffness of dry earlywood fibres was tested to be $3.1 \cdot 10^{-5} \text{ Nm}^{-2}$ and that of latewood was tested to be $1.5 \cdot 10^{-4} \text{ Nm}^{-2}$. Flexibility is another relevant mechanical parameter that characterises single fibres. It is defined as the reciprocal bending stiffness (103-107). When wetting the fibre, the bending stiffness was reduced to $0.9 \cdot 10^{-5} \text{ Nm}^{-2}$ for earlywood and to $2.6 \cdot 10^{-5} \text{ Nm}^{-2}$ for latewood (108).

These examples illustrate the drastic effect of humidity on fibre mechanics.

Thus, the influence of humid air or water on the mechanical properties of natural fibres is an important topic to be addressed in the application of cellulose-based materials. The impact of relative humidity (RH) on the elastic modulus, stiffness, or strength has been investigated by various authors (109-111). With an AFM-based indentation method, it was possible to test the mechanical properties of wet cellulose and estimate the Young’s modulus, which was in the kPa range (112). Likewise, nano mechanical mapping by AFM indicated a decrease of the DMT modulus in a humid environment (113). Additionally, the viscoelastic properties of pulp fibres could be investigated with AFM. The fibres exhibited a decrease in the elastic moduli by a factor of 100 after water immersion, and the viscosity decreased by at least three orders

of magnitude (114). Further AFM-based colloidal probe measurements on cellulose were performed on gel beads made of cellulose to show the impact on mechanical properties in the wet state (115). Additionally, the breaking load of a single fibre depending on the RH could be determined, whereas the breaking load decreased with increasing RH (116).

Since cellulose fibres are natural fibres with a hierarchical structure, one must account for the variability in the mechanical parameters within and along the longitudinal direction of the fibre. Earlier, the inhomogeneous swelling behaviour of cellulose fibres was reported (18, 110). The swelling process of cellulose fibres is determined by the crystallinity, the degree of polymerization, the degree of fibrillation and the pore size (18, 117-119). Additionally, variability in cross-sectional areas within the fibre must be considered, as pointed out by *Biwas et al.* (120) and *Chard et al.* (121).

To establish mechanical models of fibres and fibre networks that account for the intra-fibre variability in mechanical parameters, it is essential to locally characterize fibres (122). In the following, an AFM-based method to map the strength, flexibility, and mechanical properties of single cellulose fibres depending on relative humidity and based on different sections of the fibre is reported. Other methods, such as the three-point bending test, are often based on the assumption of a constant cross section along the longitudinal direction of the fibre. However, this assumption might be slightly too simple to yield a good mechanical representation of cellulosic fibres in the dry state and even less in the wet state. To account for the variation in the cross section, the geometrical and mechanical properties of cellulose fibres along their longitudinal direction section by section was characterised.

At first, the behaviour of the local fibre surface radius of the fibre along its longitudinal direction *via* CLSM is observed. The changes in the local fibre surface radius were considered for each fibre section. Then, static force-distance curves *via* AFM with a colloidal probe were recorded to test the mechanical properties at every local loading point of the fibre. The local topography was recorded by SE measurements. A cotton linter fibre, which consists of 95 % cellulose, served as the model system (34, 37), and the results indicate that the mechanical properties of the fibres strongly varied along the longitudinal direction of the fibre, particularly in a humid environment.

3.2 Materials and Methods

3.2.1 Materials

Cellulose fibres were manually extracted from a cotton linter paper sheet that was prepared according to DIN 54358 and ISO 5269/2 (Rapid-Köthen process). Further information on the fibre is given in Table 7. The extracted fibre was mounted on a 3D printed sample holder, which supplied a fixed trench distance L of 1 mm between the two attachment points. Thus, the fibre under test was freely suspended and fully exposed to the humid environment, which minimized the influences of a substrate or other connecting fibre bonds. The set up was similar to that of *Schmied et al.* (123, 124). The glue did not penetrate the fibre, as shown in Figure 71.

Table 7: Information of the used linter fibre

Fiber length (Weightage to mass)	1.13 mm
Fibre width	16.5 μm
Curl	12.87 %
Coarseness	0.09 mg/m
FinesA	19.55 %
Fibrillation	1.78 %

3.2.2 Methods

The CLSM measurements were executed to estimate the local fibre surface curvature radius R_{Fibre} . With the AFM, the local bending δ , adhesion, and dissipation to complete the mechanical property image with the calculated local occurring contact stress σ (unit: N/m^2) and strain ε (unit: %) at each bending point could be detected. For the calculation of contact stress σ , the R_{Fibre} from the CLSM measurements were used. Regions with unique mechanical behaviour or an increase in R_{Fibre} were investigated and related to the local macroscopic fibril orientation on the fibre surface, which was identified with SEM. In CLSM and AFM measurements, the relative humidity (RH) was varied. For every RH step, the fibre was measured first at the CLSM in a climate chamber and was then moved to the AFM and put inside the climate chamber for uniform conditioning and reliable results as described in the following sections. After measuring at a certain RH, the sample was moved back to the CLSM and the RH was increased.

To assess the repeatability of the measurement technique the fibre was exposed to two cycles RH variation. After the first cycle the fibre was allowed to dry for 6 days and then the measurements of the second humidity cycle were carried out.

3.2.2.1 Confocal Laser Scanning Microscopy

A VK-8710 (Keyence, Osaka, Japan) CLSM instrument was used to investigate the local fibre surface curvature radius R_{Fibre} . The local surface curvature is a parameter which represents the surface curvature of the fibre at the contact area between the colloidal probe and the fibre as illustrated in Figure 20. Note, that R_{Fibre} is an estimate for the local curvature at the point of contact between colloidal probe and fibre and thus does not parameterize the fibre cross section. The parameter R_{Fibre} was used to estimate the contact stiffness from the colloidal probe measurements.

To this end, the fibre was placed into a climate chamber, where the RH was set at 2 %, 40 %, 75 %, and 90 %. The fibre was exposed to the RH for 45 minutes before measuring. Additionally, each experiment at the adjusted RH took at least 30 minutes in total. Thus, the measurements were carried while the fibres were not yet fully equilibrated. To reach a full adsorption/desorption equilibrium from the gas phase, an “exposure time” of at least twelve hours (116) would have been necessary. However, to ensure consistency between CLSM and AFM measurements and to avoid drift problems in AFM, 45 minutes of “exposure time” as a feasible compromise to balance effects from instrumental drift and slow swelling processes was defined.

The change of the local surface curvature radius of the fibre was analysed using the VK analyser software from Keyence (Osaka, Japan). First, the data were noise corrected. Then, cross sections were measured along the longitudinal direction of the fibre to estimate the fibre surface curvature radius R_{Fibre} at each loading point. A representative cross section is shown in Figure 20, and the corresponding recorded three-dimensional fibre images are shown in Figure 72. For every loading point, such a cross section was drawn. The change in R_{Fibre} with increasing RH was normalised to the R_{Fibre} of 2 % RH and plotted against the RH. The local investigated fibre surface curvature radius spot R_{Fibre} is needed to calculate the contact area A (Eq. (18)) between the colloidal probe and fibre.

Furthermore, regions of homogeneously varying behaviour were identified along the fibre diameter. At every loading point, the R_{Fibre} was analysed for every RH. Then, the change in R_{Fibre} at every loading point with varying RH was noted. The regions of interest (ROIs) were defined as having a similar, normalised increase in R_{Fibre} when varying the RH. The ROIs were then subjected to SEM for further investigation.

The fibre was fixed at both ends to minimise fibre twisting. For that reason, a strong twisting phenomenon within the evaluation of R_{Fibre} with different RHs was not observable.

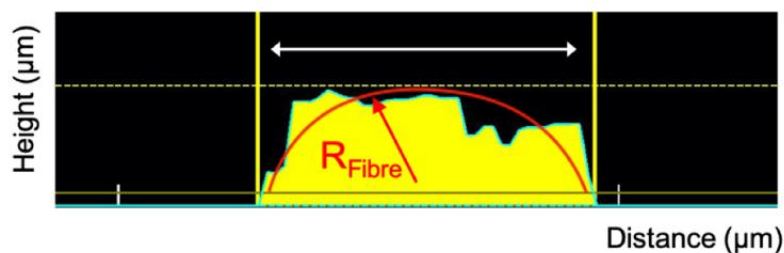


Figure 20: A representative CLSM measurement of the cross section of the fibre surface of a loading point of the fibre. The estimated fibre surface curvature radius is indicated in red. Note that R_{Fibre} parameterises a local curvature and not the cross section of the fibre.

3.2.2.2 Atomic Force Microscopy

A Dimension ICON (Bruker, Santa Barbara, USA) was used to measure static force-distance curves along the longitudinal direction of the fibre with a colloidal probe. The cantilever (RTESPA 525, Bruker, Santa Barbara, USA) with a nominal spring constant of 200 N/m (measured via thermal noise method (125)) was modified with a 50 μm diameter SiO_2 colloidal probe (Glass-beads, Kisker Biotech GmbH & Co. KG, Steinfurt, Germany). The deflection sensitivity of the cantilever (invOLS) was calibrated by performing a force-distance curve on a hard sapphire surface. All AFM experiments were performed in a climate chamber. Hence, it was possible to vary the relative humidity (RH) during the experiments. The chosen RH values were 2 %, 40 %, 75 %, and 90 %. As the RH was adjusted, the fibre was exposed to the environment for 45 minutes before starting the measurements. Force-distance curves were acquired every 5 μm along the freely suspended fibre in longitudinal direction.

The fibre was fixed at both ends to strain the fibre and prevent twisting of the fibre as the force was applied. Twisting and sideways slippage of the colloidal probe during force curve measurement was investigated in preliminary experiments. By trial and error, a colloidal probe diameter of 50 μm turned out to limit slippage on the fibre under test. A step size of 5 μm in the axial direction was set and automatically controlled by AFM software. The lateral position of the colloidal probe was corrected manually based on the camera image. Thus, the scan along the fibre was aligned stepwise along the longitudinal direction of the fibre (Figure 21). Additionally, fibre bending by the colloidal probe was monitored with the camera image to ensure consistent AFM data. Finally, the recorded force-distance curves were inspected for obvious features of a slipped colloidal probe. In the case of slippage, the probe was repositioned, and the measurement was repeated.

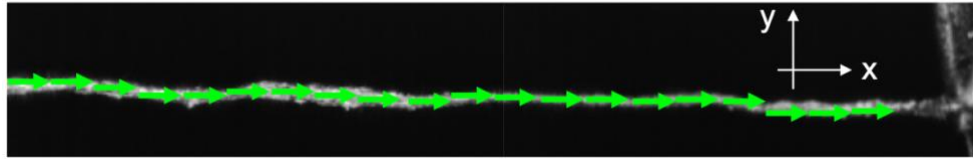


Figure 21: Schematics of the section-wise scanning process along the longitudinal direction of the fibre. At every section, the scanning trajectory was realigned to the fibre axis.

Via cantilever calibration and the deflection sensitivity, the recorded deflection-piezo position curves were transferred to force-distance curves. A schematic force-distance curve is shown in Figure 22a). The peak force setpoint was 2100 nN. The baseline was corrected with a linear fit function to the initial flat region. The contact point was defined with MATLAB (The MathWorks, Inc. Natick, Massachusetts, USA) toolbox code from Bruker. The method first determines the contact point of the curve. In general, finding the contact point in force-separation curves reliably is difficult. Various strategies to automatically determine the contact point have been reported (126-129). This method is designed to identify the contact point by a sharp transition between the out-of contact and in-contact signal. If there is a smooth transition between both regimes, the estimate for the contact point might be less accurate. 512 points per curve (512 per trace and 512 per retrace) are recorded. An offset of 20 % in the bending data to account for the potential measurement errors is assumed.

Mechanical properties such as adhesion and energy dissipation were extracted from the force-distance curve, as illustrated in Figure 22a. The adhesion force was identified as the lowest point in the retrace curve (red curve in Figure 22a), and the dissipation was defined as the integrated area between the trace and retrace curves (blue and red curves in Figure 22a). In Figure 22b), a schematic force-bending curve is displayed. To transform the force-distance curves into force-bending curves, the MATLAB code identifies the contact point in the trace curve (blue in Figure 22a) and sets this point as zero (offset). For the force-distance curve, the offset is in the origin of the curve (cf. position of zero value in Figure 22a) and b). From the data, the fibre bending δ can be read out for various forces from the data to create virtual height maps for these forces, as schematically illustrated in Figure 22b). For mapping, the fibre bending for 500 nN, 1000 nN, 1500 nN, and 2000 nN was determined. This allows for one to easily detect a potentially nonlinear local response of the fibre.

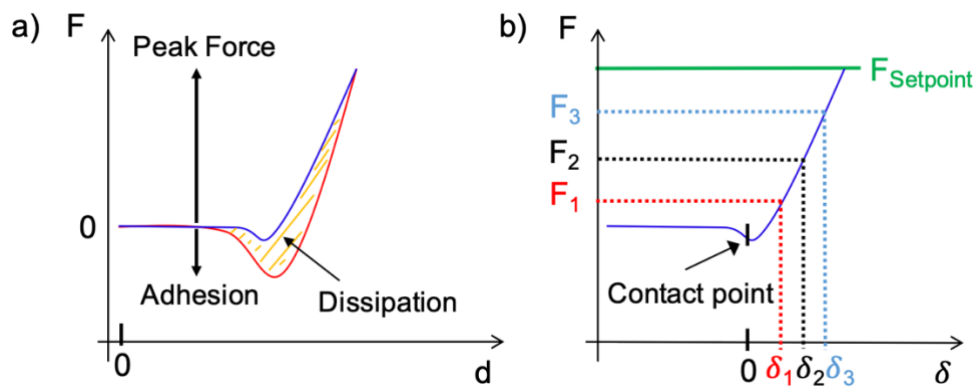


Figure 22: a) Schematic force-distance curve with extracted mechanical properties. b) Force-bending displacement curve with visualization of multiple virtual setpoint forces F .

This non-linearity is shown in Figure 23 a-d) with representative force-bending displacement curves at different RHs. The curves clearly show the nonlinear force-bending relationship. Thus, the bending displacement for different applied forces cannot be easily estimated, as seen in the sketch (Figure 22b). Due to piezo hysteresis or thermal drift trace (blue) and retrace (retrace) curves did not merge not in the contact point region (Figure 23 a-d)).

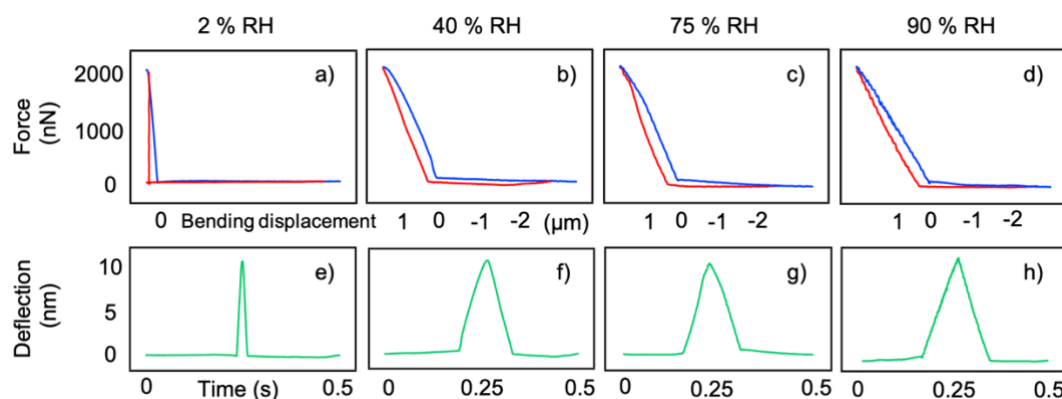


Figure 23: a-d) Force-bending displacement curves measured at different RHs. The curves from loading point #15 (from left to right in figure 9) are shown. In blue: trace curve, in red: retrace curve. The force-bending curves exhibited a slightly non-linear force-bending relationship. Therefore, the bending displacement at different forces to create a map which highlights strongly non-linear regions were read out. e-h) Force-time plots of the corresponding force-bending displacement curves at the different RHs.

In contrast to the conventional three-point bending test (Figure 24a), where the specimen is bent only at the centre, here a test along the longitudinal direction of the fibre every $5 \mu\text{m}$ in a scanning three-point bending test (Figure 24c) is performed. In conventional three-point bending testing, the second moment of inertia

$$I = \frac{\pi}{4} \cdot (r_2^4 - r_1^4) \quad (11)$$

is a critical parameter that must be homogenized along the fibre to obtain Young's modulus

$$E = \frac{F \cdot L^3}{192 \cdot \delta \cdot I}. \quad (12)$$

The calculation of Young's modulus *via* the conventional three-point bending test includes the applied force F , the trench length L , the bending displacement δ , and the second moment of inertia I . The second moment of inertia I includes the inner and outer radii (r_1 and r_2) of a schematic circular fibre, as shown in the cross section in Figure 23b). Since a cotton linter fibre is a natural fibre, the dimensions along the fibre cannot be modelled using a single value for the cross section. To circumvent this problem, many bending tests are preformed and scanned along the longitudinal direction of specimen to test and determine the mechanical properties. Thus, it was possible to detect the local bending displacement δ of the fibre via AFM from the force curves and could, therefore, study the bending behaviour of the fibre at different applied forces. In addition to the local adhesion, dissipation, and bending ability along the longitudinal direction of the fibre, the mechanical property imaging with the local "contact stress" was completed:

$$\sigma = \frac{F}{A}, \quad (13)$$

and strain

$$\varepsilon = \frac{\Delta L}{L} \quad (14)$$

for each loading point.

The local contact stress for each bending point was obtained by dividing the applied force F by the contact area A . The contact stress is not corresponding to the "bending stress", which is described as the bending moment divided by the resistance moment (130). The strain is calculated as the elongation ΔL divided by the trench length L . The estimation of the variables contact area A and elongation ΔL is described in the following.

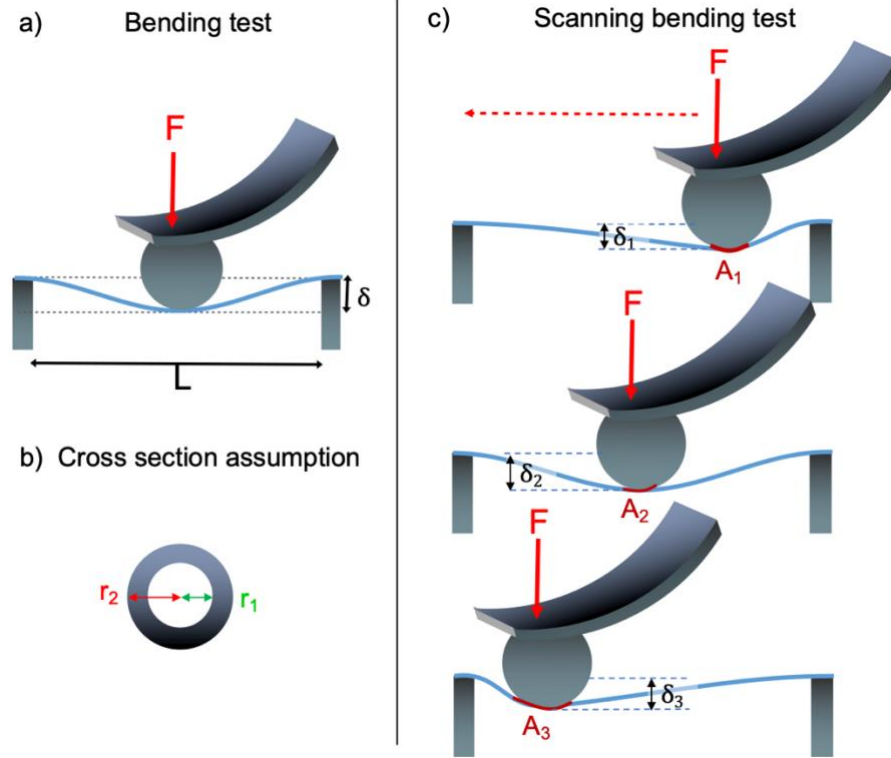


Figure 24: a) Schematic of a conventional three-point bending test. b) Cross section of a fibre and the corresponding equations for a three-point bending test. c) Principle of a scanning three-point bending test.

3.2.2.3 Estimation of Contact Area A and Elongation ΔL

The area A of contact between the colloidal probe and the fibre could not be measured directly. Thus, this parameter had to be estimated to determine the contact stress (Eq. (13)). To simplify the model, it was assumed that rough features at the fibre surface are compressed i.e. that there is a (nearly) conformal contact between probe and fibre.

The contact mechanics of this problem is similar to the contact mechanics of a sphere pressing into a curved surface of a cylinder as illustrated in Figure 25a) and b). The contact area has an elliptical shape, with the major axis a and the minor axis b . Following (131) the major axis a can be calculated as:

$$a = \left(\frac{3 F [K(e) - E(e)]}{2 \pi e^2 E^* P} \right)^{\frac{1}{3}} \quad (15)$$

and the minor axis b as

$$b = a \sqrt{1 - e^2}. \quad (16)$$

Here, $K(e)$ is the complete elliptic integral of the first kind, $E(e)$ the complete elliptic integral of the second kind, e the eccentricity, E^* the reduced elastic modulus, and P the principal curvature. As the eccentricity is a function of the profiles of the contacting surfaces, it varies with the different radii along the fibre axis. Thus, the elliptical integrals $K(e)$ and $E(e)$ also vary along the fibre axis. All values are extracted from the diagrams given in (131) in chapter 3. For more information see chapter 8.1.

The reduced elastic modulus E^* is given by

$$\frac{1}{E^*} = \frac{1 - \nu_{\text{Colloidal}}^2}{E_{\text{Colloidal}}} + \frac{1 - \nu_{\text{Fibre}}^2}{E_{\text{Fibre}}} \quad (17)$$

The elastic modulus of the SiO₂ colloidal probe ($E_{\text{Colloidal}}$) is 35 GPa (132). The elastic modulus of the fibre was determined as the DMT modulus of the fibre surface (85). The DMT modulus was mapped with a sharp cantilever (Scan Asyst Fluid +, Bruker, Santa Barbara, USA) in PeakForce tapping mode with a force constant of 1.1 N/m, PeakForce Setpoint of 10 nN, and amplitude of 300 nm. Representative DMT modulus maps are shown in Figure 75. The DMT modulus was 60 GPa for 2 % RH, 21 GPa for 40 % RH, 2 GPa for 75 % RH and 0.5 GPa for 90 % RH. The Poisson's ratio $\nu_{\text{Colloidal}}$ was defined as 0.5, and the Poisson's ratio ν_{Fibre} was defined as 0.3. The radius of the colloidal probe $R_{\text{Colloidal}}$ was 25 μm . The local fibre curvature surface radius R_{Fibre} was recorded via CLSM at every loading point.

To calculate the total contact area A , it was assumed that the major axis of the ellipse shaped contact area $2a$ is increased by the arc length of $S_1 + S_2$ due to the bending of the fibre (Figure 25c). Thus, the contact area is approximated as

$$A = \pi \cdot \left(a + \left(\frac{S_1 + S_2}{4} \right) \right) \cdot b \quad (18)$$

The geometrical relations of the sphere bending the fibre are shown in Figure 25d). The model assumes tangents, displayed in dashed red and turquoise, in arc lengths S_1 and S_2 of the fibre and the colloidal probe with occurring angles α and β . Via geometric laws, the same angles are also present between the radius $R_{\text{Colloidal}}$ and the white dashed middle line. Variables c and d display the segment lengths to the fixed end of the fibre and present loading point.

The tangents 1 and 2 are defines as:

$$\text{Tangent 1} = \sqrt{\delta^2 + c^2} \quad (19)$$

and

$$\text{Tangent 2} = \sqrt{\delta^2 + d^2} \quad (20)$$

The angles α and β are calculated as:

$$\tan(\alpha) = \frac{\delta}{c} \quad (21)$$

and

$$\tan(\beta) = \frac{\delta}{d} \quad (22)$$

Therefore, the arc lengths S_1 and S_2 can be defined as

$$S_1 = R_{\text{Colloidal}} \cdot \alpha \quad (23)$$

and

$$S_2 = R_{\text{Colloidal}} \cdot \beta \quad (24)$$

With the calculated contact area A , the contact stress σ as defined in Eq. (12) can be calculated. A linear elastic Hertzian contact mechanics was assumed and the viscoelastic parts were neglected. The viscoelastic behaviour is a time dependent phenomenon. As illustrated in Figure 23e-h) the fibre was bent only 0.5 s in total at each point of measurement. The force peak at 0.25 s in the time series exhibited hysteretic forces due to adhesion but was otherwise symmetric, which indicates that there were only small contributions from time depending forces (viscoelastic behaviour). This is compatible with literature data, where storage and loss modulus of cellulose fibres were investigated via Brillouin spectroscopy (133). The authors concluded that loss modulus (viscous behaviour) was much (25 times) smaller than the storage modulus (elastic behaviour). Thus, it seems reasonable to neglect the viscous contributions in our simplified contact mechanical model.

Many simplifying assumptions had to be made in the model. The contact model assumes a conformal contact between colloidal probe and fibre and a homogeneous fibre material.

Another error source can be the addition of the arc length S_1+S_2 to the major axis of the elliptical shaped contact area. Additionally, the contact area could also be increased due to the bending in the minor axis $2b$ of the elliptical shaped contact area. Thus, it seems reasonable to assume a rather large error for the estimated contact area A on the order of at least 30%.

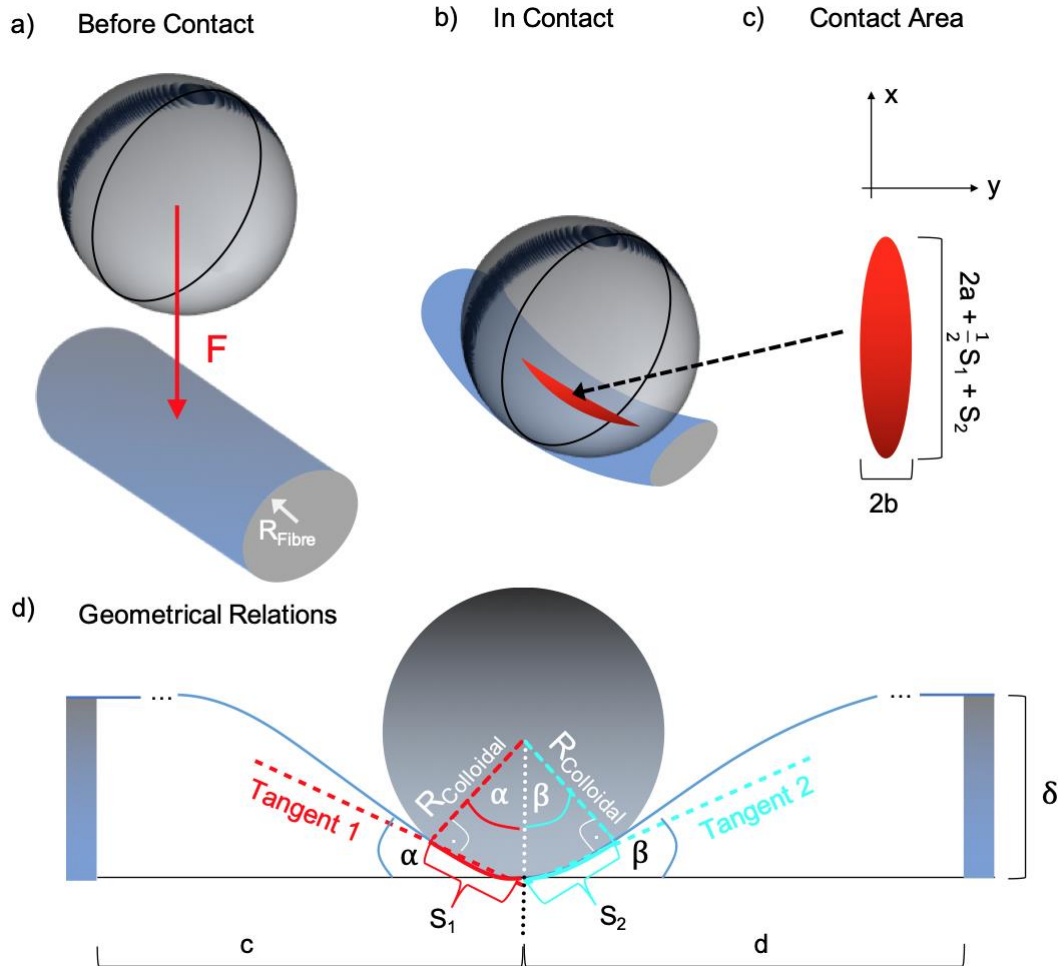


Figure 25: Schematics of the contact mechanics between the colloidal probe and the fibre. a) Before contact and b) in contact. The elliptical contact area is illustrated in c). In d) the geometrical relations between the colloidal probe and the fibre are shown.

To determine the strain along the longitudinal direction of the fibre, elongation ΔL must also be estimated (see Eq.(14)). Often, the elongated bending length is determined based on a Euler-Bernoulli beam. However, this approach requires homogeneous parameters, and for a fibre, such homogenization is questionable. Thus, the bending was limited to small values, and the maximum fibre bending δ was approximately $2 \mu\text{m}$, which is rather small compared to the trench length $L = 1 \text{ mm}$. Thus, the elongation could be estimated from simple geometrical assumptions with:

$$\Delta L = \text{Tangent 1} + \text{Tangent 2} - L \quad (25)$$

as illustrated in Figure 26. An error of 25 % of the strain due to the geometrical assumptions was assumed.

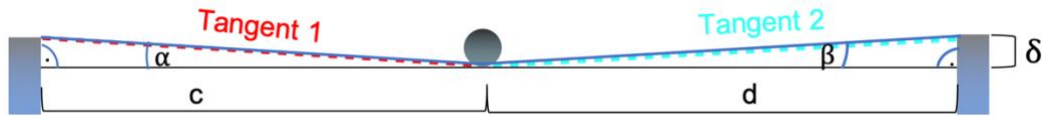


Figure 26: Schematics of the calculation of the elongation ΔL .

3.2.3 Scanning Electron Microscopy

The individual fibre topography was analysed using a scanning electron microscope (SEM) (MIRA3, TESCAN, Brno, Czech Republic) in secondary electron (SE) imaging mode at a low acceleration voltage (3 kV). Here, the fibre ends were glued with a silver paste to a metal substrate to enhance the electron transport and avoid a too fast charging of the fibre surface.

3.3 Results and Discussion

In the following, it is discussed at first how the radius of the fibre surface curvature R_{Fibre} was measured with CLSM and evolved with increasing RH. Then, by combining CLSM and AFM colloidal probe bending measurements, a mechanical image of a single fibre and related the mechanical behaviour and the increase in R_{Fibre} for each ROI was developed.

3.3.1 Fibre Geometry

CLSM measurements were used to measure the change of the paper fibre surface curvature radius R_{Fibre} . These results were used to estimate the contact area A of the colloidal probe and the fibre to determine the contact stress σ . Figure 27a) shows a CLSM image of the fibre. The coloured boxes indicate regions of interest, ROIs, as they were used for CLSM and SEM characterization. The ROIs were defined as regions with similar normalised change in R_{Fibre} in a humid environment. In Figure 27b), the normalised change in R_{Fibre} of the framed ROIs is displayed over the RH in %. The change in R_{Fibre} was normalised by the value of R_{Fibre} at 2 % RH in each ROI.

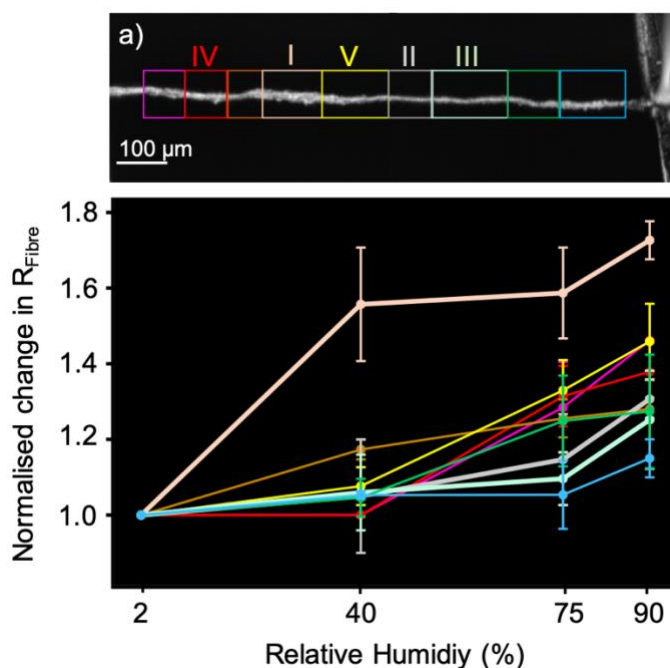


Figure 27: a) CLSM microscopy image of the investigated fibre. The coloured boxed indicate the ROIs. b) The normalised change in $R_{Fibre}/RRH=2$ is displayed over the relative humidity in % of the marked regions of a).

As shown in Figure 27, the changing behaviour of the surface curvature radius of a natural paper fibre is inhomogeneous along the fibre diameter, as indicated with different ROIs.

Cellulose fibres with different degrees of polymerization, cellulose contents, crystallinity, and degrees of fibrillation are expected to exhibit different degrees of swelling (18, 117-119). The increase in R_{Fibre} could origin from fibre swelling or e.g. from fibre twisting. This was for minimising the fibre twisting with the fixed end of the fibre in our set up and did not observe this phenomenon in a strong way, but it cannot be excluded.

Three ROIs (I, II and III) were investigated in more detail. The corresponding SE images of the discussed ROIs are shown in Figure 28. ROI I (light orange) in Figure 27a) increased to a normalised change in R_{Fibre} of 1.72 ± 0.05 when increasing the RH to 40 %. When increasing the RH to 75 % and 90 %, the R_{Fibre} only slightly increased. The behaviour in ROI II (grey) was different. The changing in R_{Fibre} was much lower until an R_{Fibre} of 1.31 ± 0.09 was reached at 90 % RH. In ROI III (green), there was little difference between the radii at 75% and 90 % with a normalised change of 1.25 ± 0.13 .

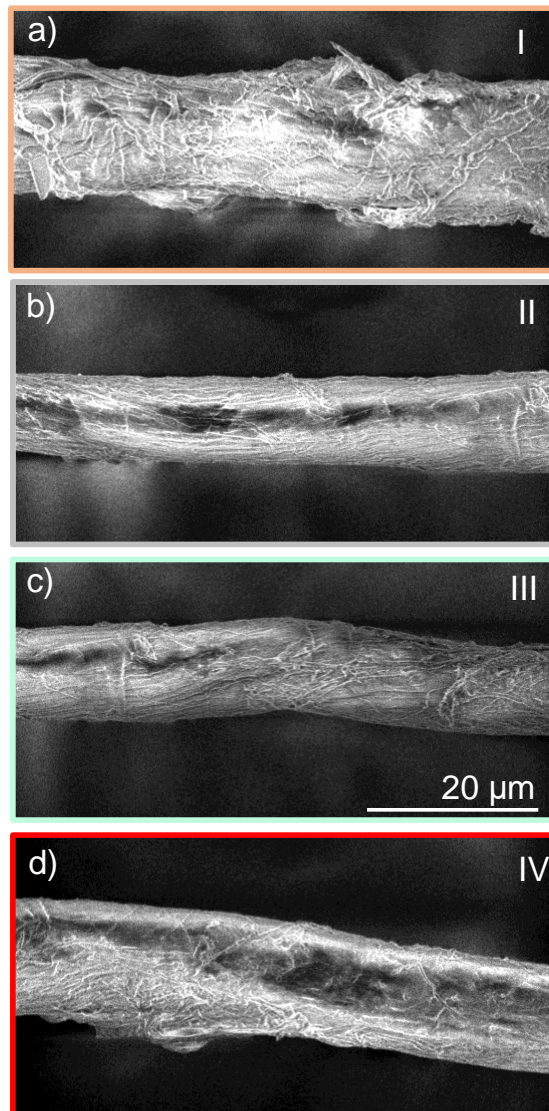


Figure 28: SE images of fibre sections. a) ROI I b) ROI II c) ROI III, d) ROI IV.

A correlation between the changes of R_{fibre} in the different ROIs and the fibre surface structure with its macroscopic fibrils was observed.

As shown in Figure 28, the SE images of ROI I exhibited a larger cross section compared to ROIs II and III. In Figure 28a), the SE image revealed macroscopic fibril orientation with little order on the surface in the ROI I. From Figure 28, it is also clear that the fibre cross section varies along the longitudinal direction of the fibre. For example, the fibre in ROI II has a smaller cross section than that in ROI I. In ROI II, the macroscopic fibrils are much better aligned than in ROI I, which exists in an ordered, aligned way. Similar observations can be made for ROI III. ROI IV shows a more complex structure of the macro fibrils.

3.3.2 Colloidal Probe Mapping

Mechanical properties such as local adhesion, energy dissipation, or the bending of the paper fibre were investigated with AFM. Properties such as contact stress and strain were calculated according to Eqs.(13) and (14). The measurements were carried out with a colloidal probe bending the fibre point by point along the longitudinal direction of the fibre. Thus, a detailed image of the mechanical behaviour along the fibre could be obtained. Mechanical properties such as adhesion, dissipation, and bending ability were estimated from the force-distance data together with contact stress and strain, as displayed in Figure 29. Figure 29a) shows the CLSM together with the mechanical properties at 2 % RH, b) at 40 % RH, c) at 75 % RH, and d) at 90 % RH. The shape of the fibre is consistent at all RHs; thus, significant fibre twisting can be excluded.

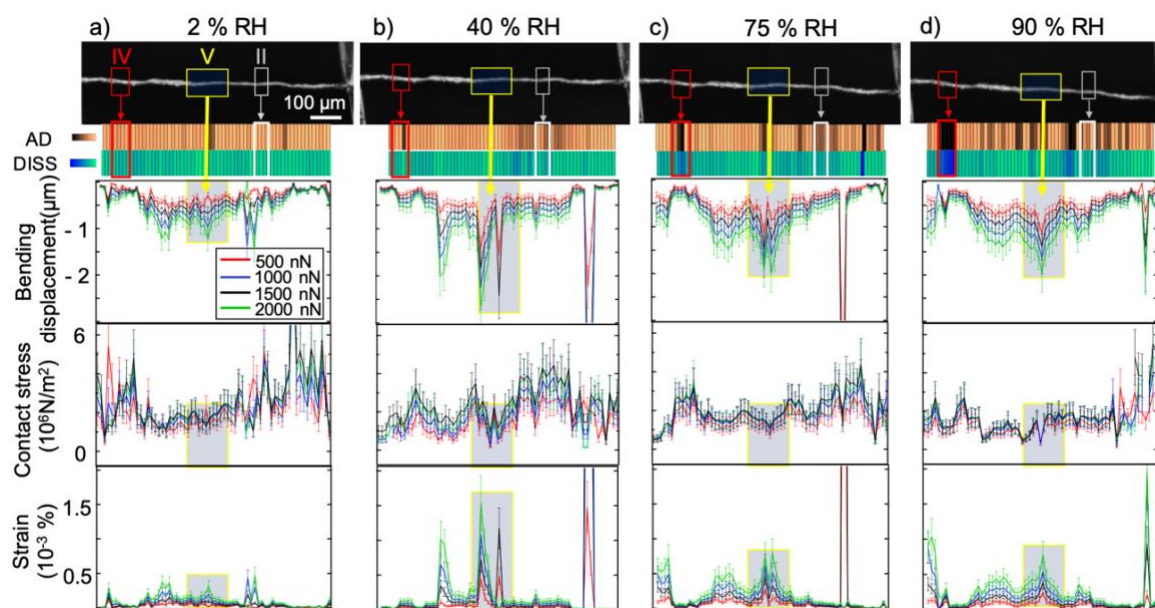


Figure 29: Mechanical characterisation of a cellulose fibre along the longitudinal direction of the fibre. From top to bottom: CSLM image of the fibre with the local adhesion and dissipation maps along the fibre beneath. The scale bars are -800 to 0 nN (adhesion) and 1 to 1×10^5 J (dissipation). Beneath: bending displacement, contact stress (error 30 %) and strain (error 25 %) along the fibre. The mechanical properties in a) are at 2 % RH, b) at 40 % RH, c) 75 % RH and d) 90 % RH. The discussed ROIs are marked with II, IV, and V.

First, the evolution of the adhesion properties with increasing RH will be discussed. The data in Figure 29 and Figure 30 show that the adhesion force increases with increasing RH. In general, two trends in adhesion changes with increasing RH could be observed: (i) a strong increase in adhesion with increasing RH, as observed in ROI IV, and (ii) a minor increase in adhesion, as in ROI II. The corresponding topographies with their macroscopic fibril orientation in both ROIs are shown in the SE images in Figure 28. Figure 28b) displays the topography of ROI II, which exhibits an ordered macroscopic fibril orientation along the fibre. Figure 28d) reveals more macroscopic fibrils oriented on the surface in ROI IV than in ROI II.

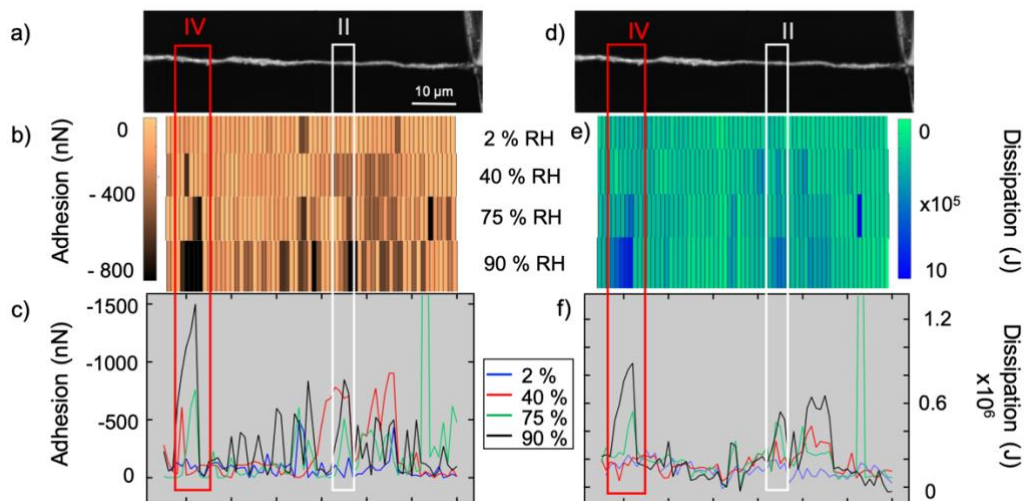


Figure 30: Adhesion and dissipation maps along the longitudinal direction of the fibre. a) CLSM image of the fibre, b) of adhesion maps and c) corresponding cross-sections along the fibre at different RHs. d) CLSM image of the fibre (same as a), b) dissipation map and c) corresponding cross sections along the fibre at different RHs.

From the bending data in Figure 29, the local bending increased when increasing the RH from 2 % RH to 90 %. Additionally, mechanical effects (clamping) play a role: the bending of the fibre is reduced at both fixed ends and is increased in the middle of the fibre. Here, the reduced bending at both ends is due to attachment to the sample holder.

An interesting observation is marked in the ROI V in Figure 29. At 2 % RH, the bending behaviour looks normal with increased bending ability in the middle of the fibre. When increasing the RH to 40 %, ROI V exhibited two significant notches at positions where the fibre was particularly soft. The soft regions (notches) broadened and were no longer distinctive at 75 % RH. When increasing the RH further to 90 %, only one notch (=soft region) could be distinguished. A possible interpretation is that by increasing the RH, more water molecules intrude into the cellulose network, weakening the internal structure, which reduces the stability of the fibre (13-15). In addition, the water molecules act as lubricants between the fibrils, which leads to the ability of higher bending at higher RH as the fibrils can slip along each other. As indicated in ROI IV in Figure 29, some areas exhibit distinctive regions with strong local deformation (notches in the plot). Thus, it could be speculated that at 40 % RH, “wet spots” develop, which weaken the fibre in distinctive regions. Increasing the RH further to 90 % RH, more water molecules diffuse in the other parts of the fibre, which leads to more uniform deformation along the longitudinal direction of the fibre.

In Figure 31 local bending lines are given for the selected forces of 500 nN, 1000 nN, 1500 nN and 2000 nN. The pronounced and repeated bending ability of ROI V is marked in yellow. Also,

other features in the bending ability are visible. In the red marked areas in all graphs from Figure 29 some very pronounced bending features can be observed. These are interpreted to origin from noise from the measurement. As they occur near the fixed end the bending ability of the fibre was actually reduced and the colloidal probe probably slipped along/from the fibre. Overall, Figure 29 suggests that the reproducible bending features (yellow) were due to local variations in the fibre properties.

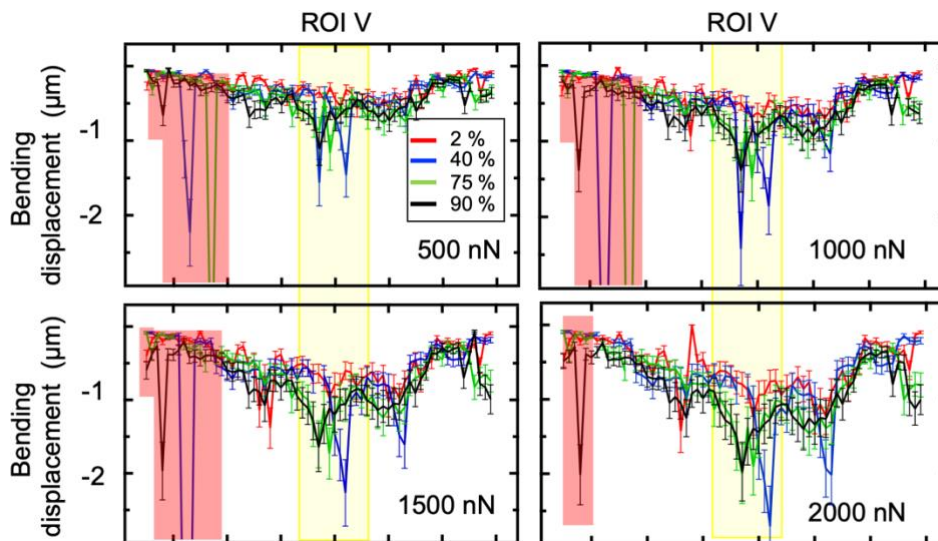


Figure 31: Bending displacements along the longitudinal direction of the fibre at different RHs. a) at 500 nN, b) at 1000 nN, c) at 1500 nN and d) at 2000 nN. The ROI V is marked in yellow. Data close to the fibre attachment (red) can be attributed to experimental noise (probe slippage).

To verify that the bending behaviour displays the actual bending behaviour with its features, a second set of experiments where a fibre was characterised for two RH cycles were performed (see chapter 3.4).

In the contact stress graphs in Figure 29, it is evident that the contact stress was higher at both ends of the fibre. This is due to the attachment at the fixed ends and should not be interpreted as a higher strength of the fibre. The contact stress at both fixed ends decreases as the RH is increased. Additionally, here, the increased amount of water molecules inside the cellulose network destroys bonds and act as a lubricant between the fibrils, which leads to fibre softening.

The strain displayed in Figure 29 is linked to the bending properties of the fibre. Thus, the strain behaviour follows the same trend as the bending behaviour and is assumed to be interpreted identically.

Furthermore, the applied method makes it possible to establish stress-strain diagrams for each loading point. The stress-strain diagrams for ROIs I, II, and III are displayed in Figure 32. To derive the stress-strain curves, the stress and strain are also calculated for 200 nN and 350 nN for completeness.

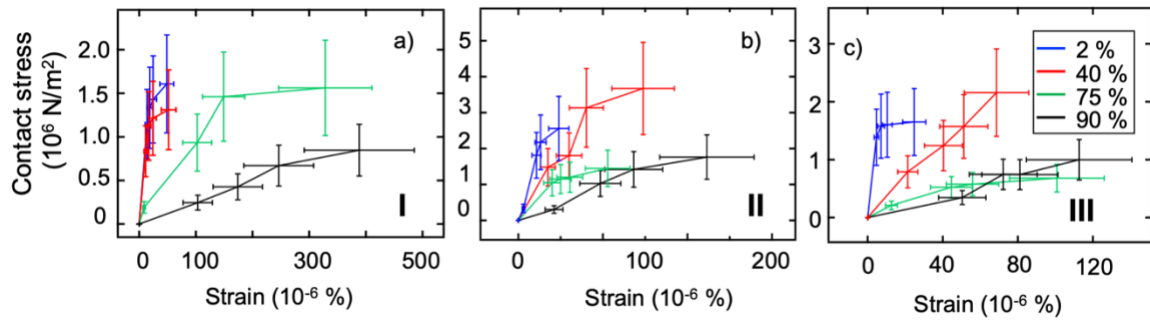


Figure 32: Stress-strain diagrams of ROI I in a) of ROI II in b) and of ROI III in c).

The stress-strain diagram of ROI I is shown in Figure 32a). It is evident that the slopes in the linear-elastic area decrease with increasing RH. In a linear elastic area, stress and strain are proportional and the deformation is reversible. In a non-linear elastic area, the stress and strain are not proportional to each other, but the deformation is still reversible. In an elastic-plastic area the deformation is partly plastic and irreversible. At 2 % and 40 % RH, linear-elastic and non-linear elastic areas are monitored but no elastic-plastic areas are detected. At 75 % and 90 % RH, the non-linear elastic area is distinctively larger than that at 2 % and 40 % RH. However, there is no clear indication for an elastic-plastic area. Therefore, it is suggested that there is no plastic deformation in the fibre structure in ROI I.

Figure 32b) shows the stress-strain diagram of ROI II. The slopes in the linear-elastic area also decrease with increasing RH. The non-linear-elastic area increases with increasing RH. Additionally, no clear indication for an elastic-plastic area could be observed.

ROI III, shown in Figure 32c), exhibited the same behaviour as ROIs I and II. The slopes in the linear-elastic area decreased with increasing RH, and the non-linear-elastic regime increased with increasing RH. Additionally, no clear indication for an elastic-plastic regime can be found within the error bars.

These observations strengthen the assumption that the fibre could fully recover its structure between the static colloidal probe experiments, and the presented method with applying multiple setpoints could additionally preserve the fibre.

3.3.3 Determination of virtual Young's moduli

With Hooke's law

$$\sigma = E \varepsilon \quad (26)$$

, the Young's modulus can be determined in the linear elastic area. The calculated Young's moduli for every RH in the three ROIs are shown in Table 8. In opposite to the literature, the Young's modulus was not extracted for the whole fibre, but in sections of the fibre. Additionally, in the presented contact model a conformal contact between colloidal probe and fibre and a homogeneous fibre material was assumed. Thus, the Young's modulus values display a measure for the fibre stiffness in a certain ROI on the fibre and cannot be treated as absolute values and are called therefore "virtual Young's moduli".

Table 8: Corresponding virtual Young's moduli of ROIs I, II, and III of Figure 29.

RH (%)	E (GPa) ROI I	E (GPa) ROI II	E (GPa) ROI III
2	32 ± 8	93 ± 28	95 ± 27
40	28 ± 7	72 ± 20	51 ± 13
75	10 ± 4	49 ± 10	25 ± 5
90	2 ± 2	19 ± 3	20 ± 4

The virtual Young's moduli in ROI I exhibited lower values than those in ROIs II and III (Table I). Typical values for the Young's modulus for plant-based cellulose are 20-80 GPa but can also amount to 138 GPa for highly crystalline cellulose (14, 96-99, 134-136). Furthermore, the Young's modulus is dependent on geometrical aspects, such as cell wall thickness or fibre width.

In Figure 28, the corresponding SE images of the ROIs are shown.

ROI I exhibited a larger diameter and thus had a high fibre mass, which is mostly represented by the S2 wall. The S2 wall is mainly responsible for the mechanical properties (34, 35). Also, the surface in ROI I showed an unordered macroscopic fibril orientation. In ROIs II and III, the SE images in Figure 28 show smaller diameters and an ordered macroscopic fibril orientation on the surface. This observation could support the fact that the fibre mass (corresponding the mass of S2 layer) plays a role in the stiffness of a fibre. Furthermore, the order and arrangement of the microscopic fibrils on the surface could be an indicator of the mechanical strength of the fibre. Additionally, with respect to the mechanics, it seems reasonable that unordered macroscopic fibrils are indicative of a reduced local stiffness of the fibre.

All values of the Young's moduli in Table 8 decreased with increasing RH. This is also stated in the literature (109-112, 114). The values of in Table 8 normalised to the Young's modulus values of 2 % and plotted in Figure 33. From Figure 33 it is clear that all normalised Young's moduli from the different ROIs decreased to the same range of values at 90 % RH. In ROI I, the normalised Young's moduli decreased to 0.21, 0.20 in ROI II, and 0.22 in ROI III. This means that a decrease in the Young's moduli of 6-7 times from the initial value at 2 % RH was observed. As the fibre was not immersed in water to cause a drop of 10-100 times the Young's moduli and obtain values in the kPa range as (112), a decrease of 6-7 times at 90 % RH aligns with (114).

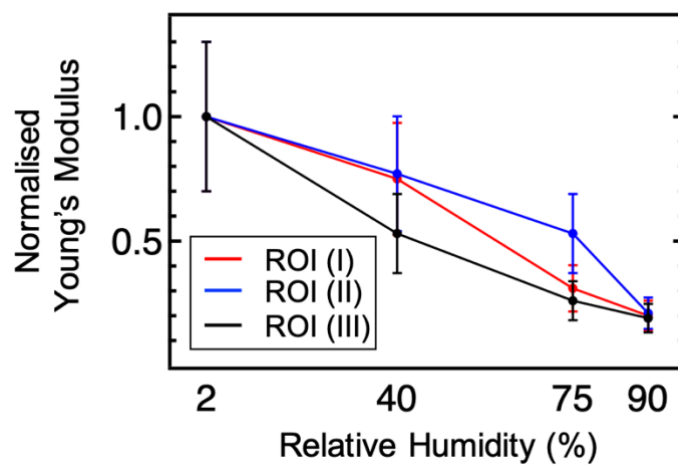


Figure 33: Young's modulus (normalised to the modulus at RH = 2 %) versus the RH for ROIs I-III.

3.4 Repeatability of the measurement technique

The measurement technique was applied to another fibre under test for two cycles of changing the RH to detect the possible variations in the change of the normalised R_{Fibre} and in the bending behaviour and to assess the repeatability of the experiments. The first cycle was performed as: every RH firstly measured at the CLSM, moved to the AFM and then increase the RH and move back to the CLSM. Then the fibre was dried for 6 days and a second cycle was performed in the same measurement order as the first cycle. For better visualisation, the 20 % error in the bending is not included in the following figures.

In Figure 34 the normalised R_{Fibre} over the RH for every ROI changes and two different cycles of changing the RH is shown. It is clear that the increase in the normalised R_{Fibre} over the RH for every ROI changes and differs slightly within the two different cycles. This variation between the cycles can be attributed partially to cycle-to-cycle variation of the CLSM experiments due to slightly different loading points but also to irreversible (or only very slowly reversible) variations of intra fibre properties. It is suggested that the increase of RH in the first cycle lead to breaking of internal bonds the cellulose structure did not fully recover and a structural change appeared when the fibre dried. Therefore, the increase of the normalised R_{Fibre} over the RH changed in the second cycle.

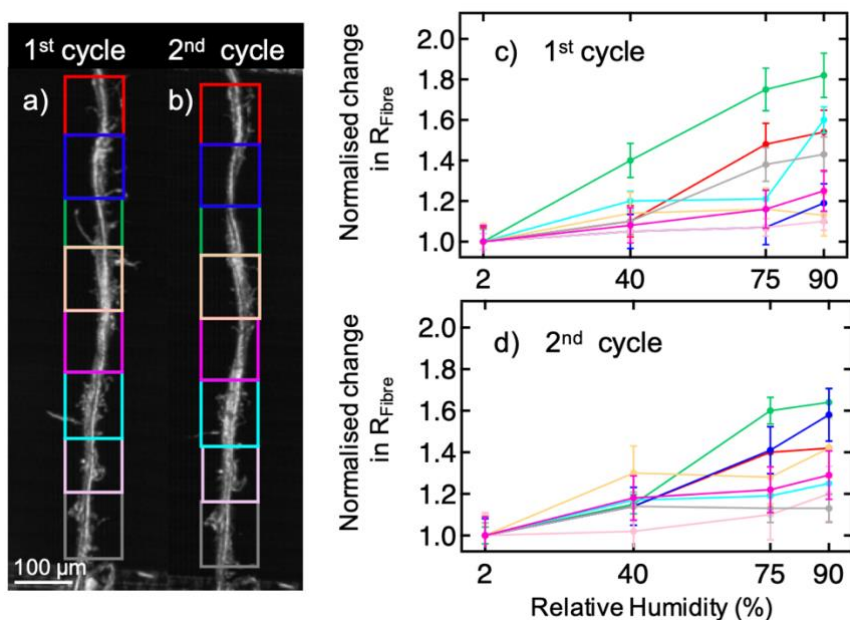


Figure 34: a) and b) displays a CLSM image of the first and second cycle of changing the RH with the respective ROIs of interest. c) and d) show the normalised change in R_{Fibre} over the RH for the first and second cycle of changing the RH (colour coded with respect to the ROI)

In Figure 35 the adhesion, dissipation and the bending behaviour for both cycles is shown as an overview image. The adhesion and dissipation increased with increasing RH as expected. Apart from that some minor changes can be identified.

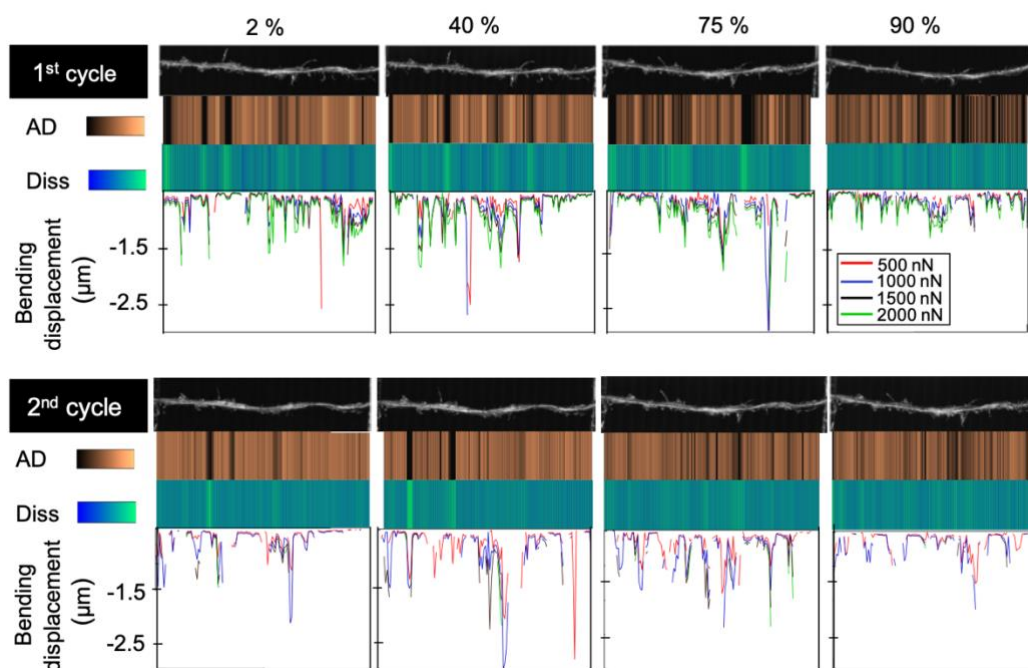


Figure 35: The CLSM images as well as the mechanical properties such as adhesion, dissipation and the bending displacements for two cycles of changing the RH are shown.

To verify the differences in adhesion and dissipation between both cycles, adhesion and dissipation are plotted in Figure 36. The adhesion properties in both cycles were similar. Some spikes occurred during the first cycle (e.g. at 2 % RH), which did not occur in the second cycle. In the dissipation plot it is visible that data of both cycles differs in particular close to the fibre attachment (left side of the graph). These differences could be explained by probe slippage or twisting of the fibre in between the two cycles. Otherwise, the dissipation properties were similar in both RH cycles.

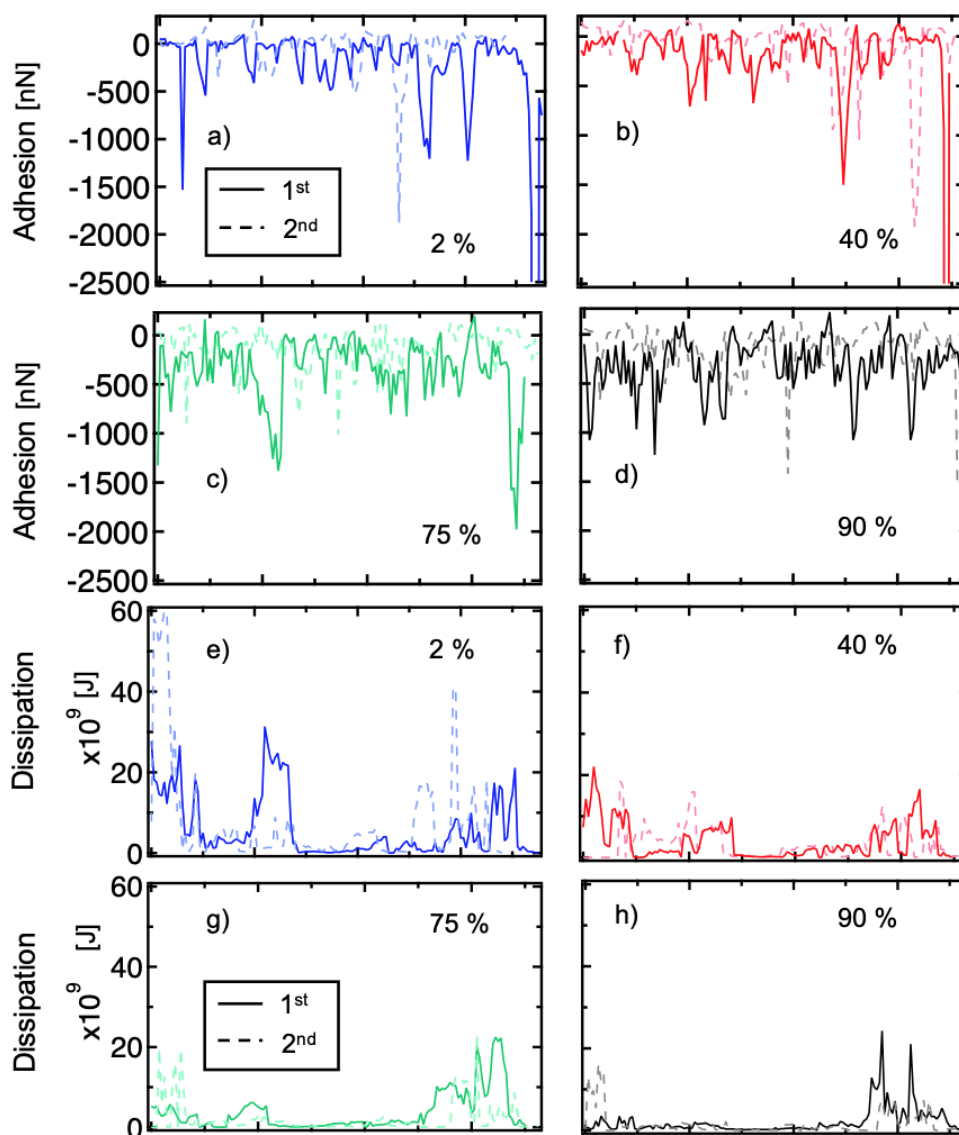


Figure 36: a-d) Adhesion properties along the longitudinal direction of the fibre of both RH cycles. The 1st cycle is plotted in solid lines and the 2nd cycle in dashed lines. e-h) Dissipation properties along the longitudinal direction of the fibre of both RH cycles. The 1st cycle is plotted in solid lines and the 2nd cycle in dashed lines.

The adhesion and dissipation properties from the first cycle with them from the second cycle are divided by each other and plotted it in a point-wise coefficient along the longitudinal direction of the fibre. This can be seen in Figure 37.

The point-wise adhesion or dissipation coefficient should be equal to 1, in an ideal condition. As shown in Figure 37a) the point-wise adhesion coefficient showed a high noise ratio in some parts of the fibre. The dissipation point-wise coefficient in Figure 37b) also exhibited a high noise ratio in some parts of the fibre, but especially in the beginning of the fibre. This could be attributed to the twisting of the fibre in between the two cycles of RH (see Figure 34 pink

and turquoise ROI). As a cotton linter fibre is a natural occurring and processed material, it cannot be expected to obtain a highly reproducible measurement.

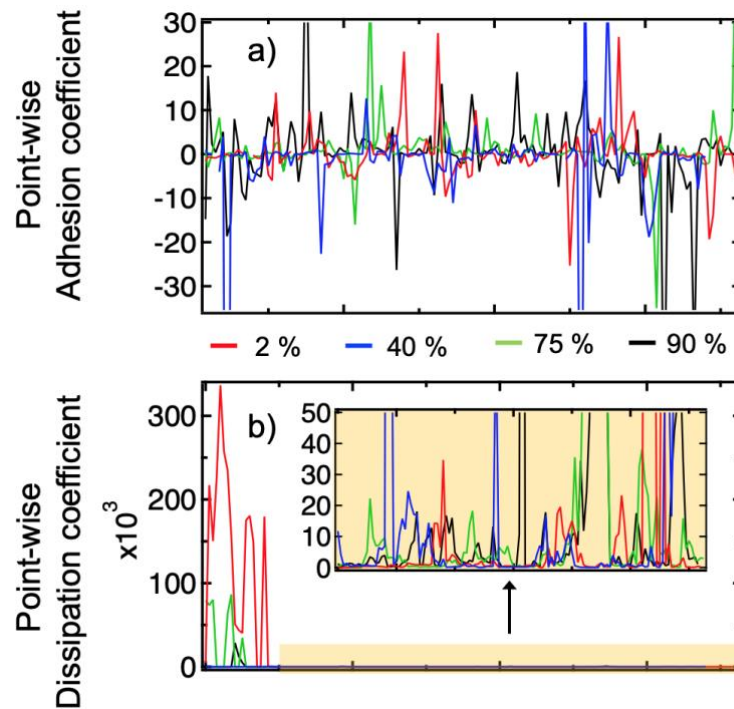


Figure 37: a) Point-wise adhesion coefficient: Adhesion of the 1st cycle divided by the 2nd cycle properties along the longitudinal direction of the fibre at the different RHs. b) Point-wise dissipation coefficient: Dissipation of the 1st cycle divided by the 2nd cycle properties along the longitudinal direction of the fibre at the different RHs.

The bending ability is plotted in Figure 76 for both cycles. In cycle #1 the highest applied force of 2000 nN could be reached. The bending ability could be mapped sufficiently for every loading point. As discussed in the previous section some “soft-spots” can be identified. These soft spots are diminishing with increasing RH.

In cycle 2 the 2000-nN-setpoint could not be reached for almost all loading points at all RH. In addition, some regions can be identified, where the bending could not be mapped in a reliable manner. This implies that with wetting of the fibre or exposing the fibre to humidity, the strength of the fibre could be lost for a time period which is longer than the experiment. Similar to Figure 76, in Figure 77 the bending ability is plotted for different RHs for both cycles. There it is shown that the soft spots of the fibre are vanishing with increasing RH in the first cycle, but are more distinctive in the second cycle. This also strengthens the assumption that the fibre strength could be lost when exposing the fibre to RH more often.

In this verification experiment, the bending ability of the fibre was decreased at both fixed ends due to clamping. In other regions of the fibre, “soft spots” again developed.

Furthermore, Figure 34 shows that the increase in the normalised R_{Fibre} over the RH for every ROI changes and differs within the two different cycles. In Figure 37, changes between the two cycles of varying the RH in adhesion and dissipation properties as well as in the bending behaviour (Figure 76 and Figure 77) are observable. In the second cycle of changing the RH, the setpoint of 2000 nN could not be reached in most spots. Thus, it can be suggested that with wetting of the fibre or exposing the fibre to RH, fibre strength is lost.

This fact also highlights the value of the introduced method. By reading out the “virtual setpoint forces” beneath the setpoint, the mechanical properties of the fibre can be displayed at different setpoint forces at a uniform fibre state. Nonlinearities or peculiar effects, such as local softening, can be detected.

3.5 Conclusions

The mechanical properties of a free hanging cotton linter fibre (clamped at both ends) with colloidal probe AFM along longitudinal direction of the fibre were measured. The proposed method of scanning along the longitudinal direction of the fibre provides a more detailed picture of the mechanical behaviour than conventional three-point bending tests, where only one measurement is performed. To demonstrate the potential of this approach, the mechanical properties of a single cellulose fibre were mapped for varying RH. The colloidal probe data were analysed in correlation with data from CLSM and SEM. The combination of these methods allowed for insights into the interdependence of swelling, bending displacement ability, contact stress, and the stress-strain curves depending on the fibre sections.

With the help of CLSM, the change in the fibre surface curvature radius of different parts of the fibre could be identified. Regions with a lower order in the macroscopic fibril orientation on the surface showed immediate deformation, and regions with a more ordered fibril orientation exhibited steady volume increase.

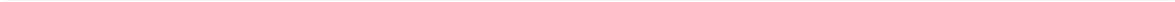
With the help of force-bending displacement curves obtained with a colloidal probe AFM, it was possible to create a detailed mechanical picture of the paper fibre. Mechanical properties such as adhesion and dissipation, bending ability, contact stress, and strain could be identified. In general, the bending ability increased as RH increased. Additionally, “soft spots” could be identified at an intermediate RH of 40 %. Increasing the RH, the soft areas became less distinctive when the entire fibre became softer. This implies that at intermediate RH, individual soft spots can occur in a cotton linter fibre weakening the fibre locally, whereas the entire fibre softens at elevated RH. By analysing the AFM force curves, it was possible to generate stress-strain curves for local points on the fibre. The stress-strain curves were dependent on the macroscopic fibril orientation: regions with an ordered macroscopic fibril orientation on the surface appeared to be stronger than those with less order. From the stress-strain diagrams, the local Young’s moduli could be identified, and the decrease in values with increasing RH was investigated.

The introduced approach highlights the difficulties in the three-point bending test, where the fibre is assumed to be homogeneous along the longitudinal direction of the fibre. Mapping with different virtual force setpoints allows one to detect a potentially nonlinear local response of the fibre.

For the next step, it will be interesting to address the internal fibre and fibril structure by microtomography or *via* fluorescent dyes in confocal fluorescence microscopy. Additionally, a better model for the contact area of a colloidal probe and the fibre will be relevant to further

develop the method. Thus, better statistics of local mechanical parameters will help to develop computer models of fibres or fibre networks that account for the inhomogeneity of the fibres. An extension of the presented method can be found in Lin, B., Auernhammer, J. and Schäfer, J.L., *et al.* (137).





Nanomechanical Subsurface Characterisation of cellulosic Fibres

In this section an AFM-based subsurface characterisation method for cellulosic fibres is introduced. As stated as an outlook in chapter 3, here the cellulosic fibres are labelled with fluorescence markers to compare the intra fibre properties with AFM measurement results.

The description of mechanical properties is usually characterised via linearized assumptions and is not resolved locally or spatially in three dimensions. In tensile tests or nanoindentation experiments on cellulosic fibres, only one mechanical parameter, such as elastic modulus or hardness, is usually obtained. To get a more detailed mechanical picture of the fibre, it is crucial to determine mechanical properties in depth. To this end, an AFM-based approach to examine the local stiffness as a function of indentation depth via static force-distance curves is discussed. This method has been applied to cotton linter fibres (extracted from a finished paper sheet) as well as to natural raw cotton fibres to better understand the influence of the pulp treatment process in paper production on the mechanical properties. Both types of fibres were characterised in dry and wet conditions with respect to alterations in their mechanical properties. Subsurface imaging revealed which wall in the fibre structure protects the fibre against mechanical loading. Via a combined 3D display, a spatially resolved mechanical map of the fibre interior near the surface can be established. Additionally, labelling the fibres with carbohydrate binding modules (CBMs) tagged with fluorescent proteins allowed to compare the AFM results with fluorescence confocal laser scanning microscopy imaging. Nanomechanical subsurface imaging is thus a tool to better understand the mechanical behaviour of cellulosic fibres, which have a complex, hierarchical structure.

4.1 Introduction

During papermaking, the natural structure of fibres can be mechanically or chemically altered, particularly at the fibre surface. To better understand how these alterations may affect the mechanical stability or water uptake of the fibres, it is essential to investigate the mechanical fibre properties at and beneath the surface. To tailor paper to advanced applications, the impact of fibre or pulp treatment before the paper-making process on the structure and mechanical properties of cellulose fibres must be understood. In particular, the fibre surface is relevant in technology because its composition and roughness determine the fibre-fibre bond strength and because it is exposed to the environment on the paper sheet surface (53, 56, 57). The properties of the bulk, however, are of similar relevance because they determine, for example, how well fluids such as water can be absorbed and how the fibre swells in a humid environment. To better understand how cellulose fibres swell and thus change their mechanical stabilities and how this process is related to the pulp treatment process of the papermaking procedure, it is essential to characterise bulk and surface properties close to the interface between the fibre and the surrounding atmosphere.

Cellulosic fibres have a hierarchical structure. The corresponding structure with its detailed description of the discussed cotton fibres can be found in chapter 2.2.2.

To date, tensile tests have characterised the tensile strength or elastic modulus of cellulosic fibres. An experimental approach to determine the longitudinal elastic modulus has been described by *Page et al.* (97). Theoretical works, e.g., *Mark and Gillis* (138) and *Salmen and Deruvo* (139), established that the MFA in the S2 layer is the determining factor for the strength of the fibre. Soon, it was established that the MFA in the S2 layer is the factor that determines the strength of the fibre. A small MFA angle leads to a high longitudinal elastic modulus (101). In addition, (140) found that the mechanical properties depend on the orientation of the microfibrils in the S2 layer. Likewise, (141) determined that the more closely the microfibrils are longitudinally aligned with each other in the S2 layer, the more tensile force could be applied. However, the transverse elastic modulus depends, according to *Bergander and Salmen*, less on the S2 layer than on S1 and S3 (142). Nanoindentation was introduced as a method to investigate the different layers in the fibre. *Wimmer et al* determined the Young's modulus and the hardness of wood fibres via nanoindentation (143). *Gindl and Schoberl* expected in their nanoindentation experiments that the Young's modulus of the S2 layer should be higher than the modulus of the other layers (144).

Sensitive nanoindentation can be performed by AFM, which even makes it possible to map mechanical properties on the surface (145, 146). A straightforward approach to obtain a picture of the landscape of local mechanical properties is "force-volume mapping". In this

approach, the force is measured via the cantilever deflection, which leads to force-distance curves. *Roduit et al.* extended this method by introducing the “stiffness tomography” method, where they evaluated static force-distance curves in segments to show the stiffness differences along the indentation path (147). Thus, it is possible to estimate the Young’s modulus of the sample at a desired indentation spot for various indentation depths. Previously released studies have shown that this approach can be applied to soft materials such as cells (89), polymers (148), bacteria (149), graphene oxide (150) or collagen fibrils (151).

In the following, it is discussed how AFM-based nanoindentation can be used to probe the near-surface bulk of cellulose fibres under dry and wet state. Variations in the local nanomechanical properties could be established and related to recovery from the hydrated state.

4.2 Materials and Methods

4.2.1 Materials

Processed cotton linter fibres were extracted manually from a linter paper sheet. The sheet was produced according to DIN 54358 and ISO 5269/2 (Rapid-Köthen process). As these fibres were already processed, they are referred to as PF (processed fibres) in the following. Unprocessed cotton fibres were manually extracted from a dried natural cotton boll. These fibres were raw and unprocessed and will be referred to as UPFs (unprocessed fibres). The fibres were fixed on both ends on glass substrates. For hydration, fibres were stored in deionised water and allowed to swell for 45 minutes. As shown in *Carstens et al and Hubbe et al.* (152, 153), the water progressed into the cotton linter test stripes in seconds. Furthermore, it was discovered that the free swelling time for a whole pulp was 70 minutes (154). However, *Mantanis et al.* recorded the swelling of cellulose single fibres in water and showed that equilibrium was reached at 45 minutes (119). The measurements in the wet state were performed as shown in *Auernhammer et al.* (113). After incubation the residual water droplet was removed before the measurement, to avoid further swelling. Overall, 9 spots of every fibre type and condition were investigated.

4.2.2 Methods

4.2.2.1 Atomic Force Microscopy

A NanoWizard II atomic force microscope (JPK Instruments AG, Berlin, Germany) was used to record maps of force–distance curves of the PF and UPF. Two types of cantilevers were used. The first type was the RTESPA-525 (Bruker, Santa Barbara, USA) with a high spring constant (HSC) of 162 N/m, a 15° opening angle only at the tip end and a radius of 30 nm. The second type was the ISC-125 C40-R (Team Nanotec, Villingen-Schwenningen, Germany) with a high aspect ratio (HAR), an opening angle of 10° for 3 µm, a radius of 10 nm and a spring constant of 30 N/m. The image size was 10 µm with 128x128 data points, a setpoint of 3000 nN and a scan speed of 20 µm/s (tip approach speed).

Force-Volume Mapping

Performing force-distance curves allows not only investigation of the surface nanomechanics but also probing of the mechanical properties near the surface. To map sub-surface properties, i.e., to obtain a three-dimensional characterisation of the mechanical properties, the force-distance was analysed stepwise (30 nm) after the contact point d_0 . Local slopes were interpolated stepwise to obtain estimates of the effective local elastic modulus as a function of depth $E_{lok}(z)$ (see Figure 38). Extracted force-distance curves from the measurements are shown for every cantilever type, every fibre type and every environment condition in the Figure 78-Figure 81.

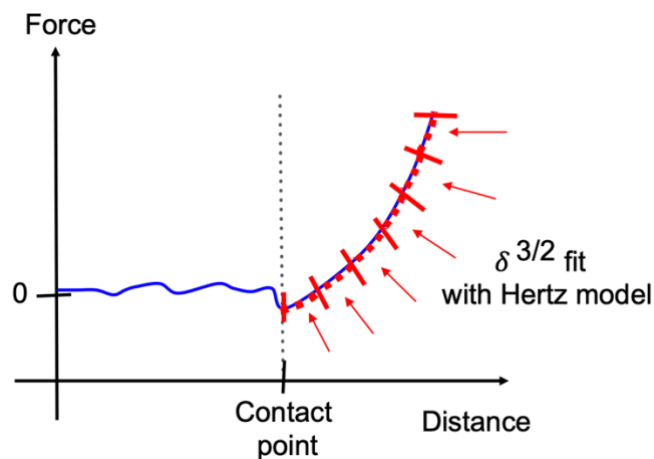


Figure 38: Principle of the stepwise analysis of a force-distance curve. The local fits are indicated in red. The indentation depth is calculated as the distance from the contact point.

Before analysing the local slopes, the force-distance curves had to be processed. The noise was removed by a Savitzky-Golay filter. The slope of the baseline was corrected with a linear fit function to the initial flat region. The initial offset and the inclination (tilting) of the curves were corrected. The contact point was identified as the first point in the repulsive regime (positive slope). More precisely, the first contact point was identified as the point where the force exceeded that of the preceding point by at least 10 times the standard deviation of the baseline signal. The position of the tip over the height z was calculated from the deflection of the cantilever, which transformed the force- z -piezo data to a force-distance or force-indentation curve, respectively.

From a two-dimensional map of force-distance curves, various parameters were calculated. The topography was calculated from the contact points. The penetration depth reached at the setpoint (maximum force) yielded the maximal indentation. To obtain mechanical information at intermediate depths, the data were interpolated in a stepwise manner in the approach curve. Thus, for the intermediate penetration depths, local fits were calculated,

which served as estimates of the effective elastic modulus assuming Hertzian contact mechanics (86) as

$$F = \frac{4}{3} \cdot E^* \cdot R^{\frac{1}{2}} \cdot \delta^{\frac{3}{2}}. \quad (27)$$

Here, F displays the applied force, E^* the effective modulus, R the tip radius and δ the indentation.

To obtain good spatial and depth resolution, the AFM cantilever was selected such that structures beneath the surface could be probed. This was accomplished via two different approaches: (i) by using hard cantilevers with a high spring constant (HSC) but conventional tips or (ii) by using softer cantilevers equipped with extremely sharp tips with a high aspect ratio (HAR). By using the HSC cantilever, a sufficiently large loading force can be applied that the tip probes the structure inside the fibres. In contrast, with the HAR cantilever, a large local pressure can be obtained at moderate loading forces. Both tip geometries are displayed in Figure 39 with SE images. The data were processed by using MATLAB code. The two-dimensional images were generated by using Gwyddion (155), and three-dimensional images were created by using Blender (156).

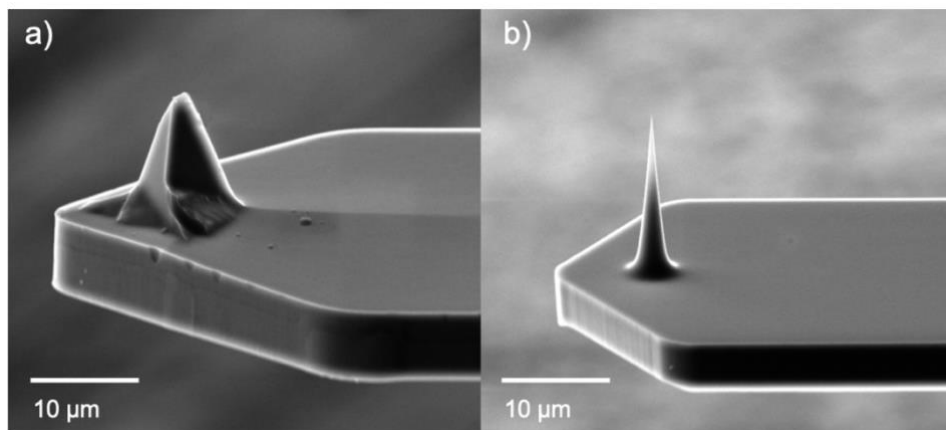


Figure 39: SE images of the tip geometry for a) the HSC cantilever and b) the HAR cantilever.

4.2.2.2 Scanning Electron Microscopy

The individual cantilever tip shapes were analysed by a scanning electron microscope (SEM) (MIRA3, TESCAN, Brno, Czech Republic) using secondary electron (SE) imaging mode at an acceleration voltage of 10 kV.

4.2.2.3 Preparation of Recombinant His- and Fluorescence-Tagged Carbohydrate-Binding Proteins (CBMs)

The DNA sequences of CBM3a (157-159) (“semi-crystalline” cellulose), CBM1Cel6a (crystalline cellulose) (157, 158) and CBM77 (160) (pectin) were taken from the CAZy database and linked DNA or protein databases (GenBank, UniProt, PDB). The evaluated sequences of *Clostridium thermocellum* (CBM3a; CCV01464.1, 4J05), *Rumminococcus flavefaciens* (CBM77; WP_009983557, 5FU5) and *Trichoderma reesi* (CBM1Cel6a; AAA34210.1, P07987) were then ordered as gene fragments (IDT, Coralville, USA) and cloned via Gibson assembly into a self-designed pET28 vector derivative. CBM-XFP-6xHis fusion proteins were expressed in *E. coli* BL21 cells by induction with IPTG. According to the protocols of (157) and “Polymer Probes And Methods” (161), induced cells were homogenised and lysed by the utilisation of EmulsiFlex-C3 from AVESTIN® in His-Trap Binding Buffer (20 mM NaH₂PO₄/0.5 M NaCl/pH 7.4 with NaOH). The desired His-tagged proteins were purified by immobilised metal affinity chromatography (IMAC) using a Ni-IDA column (Protino Ni-IDA 2000 packed column, Macherey-Nagel, Düren, Germany) and eluted with 200 mM imidazole. Elution fractions were pooled and concentrated using ultrafiltration unit filters (Vivaspin® 20; membrane 10,000 MWCO PES, Sartorius, Germany). During centrifugation, the imidazole buffer was exchanged into CBM storage buffer (50 mM Tris HCl; 20 mM NaCl; 5 mM CaCl₂ x 2H₂O; pH 7.4) via diafiltration.

For fibre labelling, CBMs were diluted 1:1000 (CBM77-mclover3, CBM1Cel6a-mKOk) or 1:500 (CBM3a-smURFP) in ddH₂O to a final concentration of ~40 µg/ml and both types of fibres were incubated in it for 5 -20 min each (PF 5 min, UPF 20min). UPF fibres were preincubated for 30 min with a 0.02% solution of Tween 20 in ddH₂O to remove or permeate the cuticula of cotton fibres.

SE images show no differences between dry, swollen and re-dried fibres. This is especially true for cotton linter fibres, which have been altered by paper production anyway (lack of cuticle and primary wall). It is also true that untreated cotton fibres hardly absorb any water, which is achieved by water-repellent substances in the cuticula and primary wall.

CBMs are able to penetrate the cell wall after a short time, but not on the complete thickness. The cell wall acts like a molecular sieve. Dyes like Calcofluor white or P4B are able to penetrate the complete cell wall. Cotton linter fibres in particular can also be marked from

the inside, as closed systems are no longer present due to paper production. Therefore, the large lumen of the fibres can be seen particularly well here. In principle, a longer incubation time always allows a greater penetration depth. This can be seen very well in untreated cotton fibres. It can also be seen that with completely closed intact cells (fibres) the CBMs do not succeed in entering the lumen. However, micro-damages occurring during preparation are sufficient to obtain the labelling on the inside as well.

4.2.2.4 3D Fluorescence CLSM Measurements

Confocal xyz series of CBM3a-mClover3-, CBM1Cel6a-mKOk- and CBM3a-smURFP-labelled fibres were recorded with a Leica TCS SP8 confocal system (Leica Microsystems GmbH, Mannheim, Germany) using an HyD detector with an HCX PL APO 63x NA 1.2 W CORR CS2 objective and the normal scanner system at 512 x 512 pixels in the 12-bit mode. Z-sections were set at a system-optimised value of 0.36 μm or a custom value of 0.2 μm per section. Sections were obtained using an appropriate laser for excitation and a small range of emission, 10 to 15 nm around the emission maximum (mClover3 ex. 488 nm, em. 505-525 nm; mKOk ex. 561 nm, em. 570-590 nm; smURFP ex. 635 nm, em. 660-690 nm). Fluorescence channels were obtained in sequential frame detection mode to avoid cross talk. The position of the images in the 3D stack are the middle of each fibre.

Cellulose microfibrils consists of highly ordered crystalline, semi-ordered para-crystalline, and disordered non-crystalline (amorphous) states (Blake et al. 2006; Tomme, Warren, and Gilkes 1995). These states (organizations) are based on the interaction of the individual cellulose chains with each other and thus their arrangement or crystal formation. Although cellulose is in principle always a semi-crystalline product, since areas of high order (crystalline) alternate with areas of low order (amorphous), type I celluloses are always more crystalline (higher organization) than type II celluloses (lower organization) and many different levels exist (Blake et al. 2006; Gautam et al. 2010; Široký et al. 2012; Fox et al. 2013). Complete crystalline and non-crystalline forms do not exist. CBMs are able to recognize the different organizational levels of cellulose and bind them based on their folding. CBM3a and CBM1Cel6a, for example, bind to flat crystalline areas due to their planar surfaces, while CBM28 binds to individual cellulose chains protruding from the disordered network via their binding cleft (Fox et al. 2013). CBM3a has the ability to bind to intermediate levels (semi-crystalline cellulose) of cellulose organization that occur in both crystalline and amorphous cellulose regions (Fox et al. 2013).

4.3 Results and discussion

4.3.1 Subsurface properties of dry fibres

From the force curve data, a 3D surface topography map was calculated. In addition, maps of the local stiffness at various indentation depths were generated. The combined 3D representation of the topography with the corresponding local stiffness is shown in Figure 40. The topography is given in a yellow colour scale as 3D representation. The colour code in z-direction encodes the local stiffness beneath. In Figure 40b) the top image shows the minimized Figure 40a) to illustrate that the image at the bottom is a cross section through the same fibre with the corresponding local stiffness maps of $E_{lok}(z)$ is shown in the xz- and yz-directions at this slice of the mapped fibre.

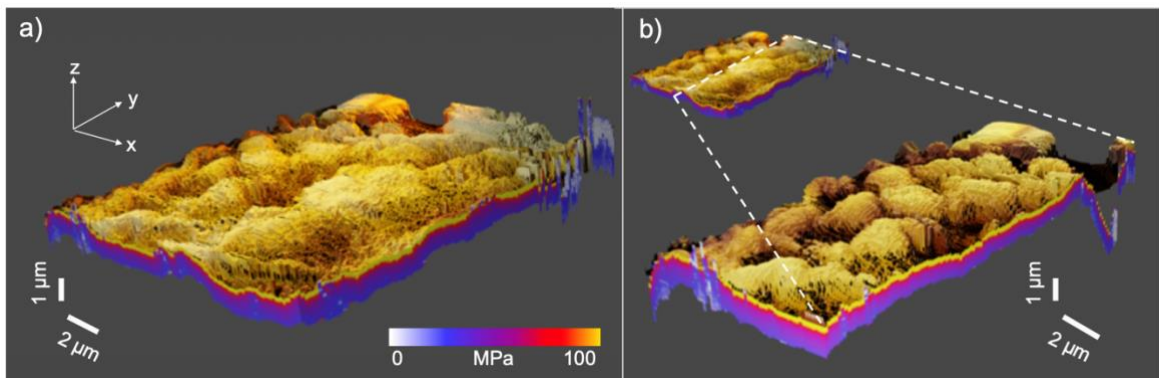


Figure 40: a) 3D representation of the surface profile of a PF recorded with a HSC cantilever. The colour in the z-direction encodes the local stiffness beneath the surface. b) A cross-sectional profile of $E_{lok}(z)$ in the xz- and yz-directions as indicated.

Figure 40a) shows an overview of the PF surface with its local stiffness maps. A cross section through the fibre with the corresponding local stiffness maps of $E_{lok}(z)$ is shown in the xz- and yz-directions in Figure 40b). The parameter for the local stiffness as a function of the depth beneath the surface $E_{lok}(z)$ is meaningful in regions where the fibre topography could be mapped with sufficient resolution. “Sufficient resolution” here means a feature size of 12.8 pixels/μm.

In Figure 41, an overview of cross sections of $E_{lok}(z)$ in the xz-direction in the PF and UPF mapped with the different cantilever types are shown.

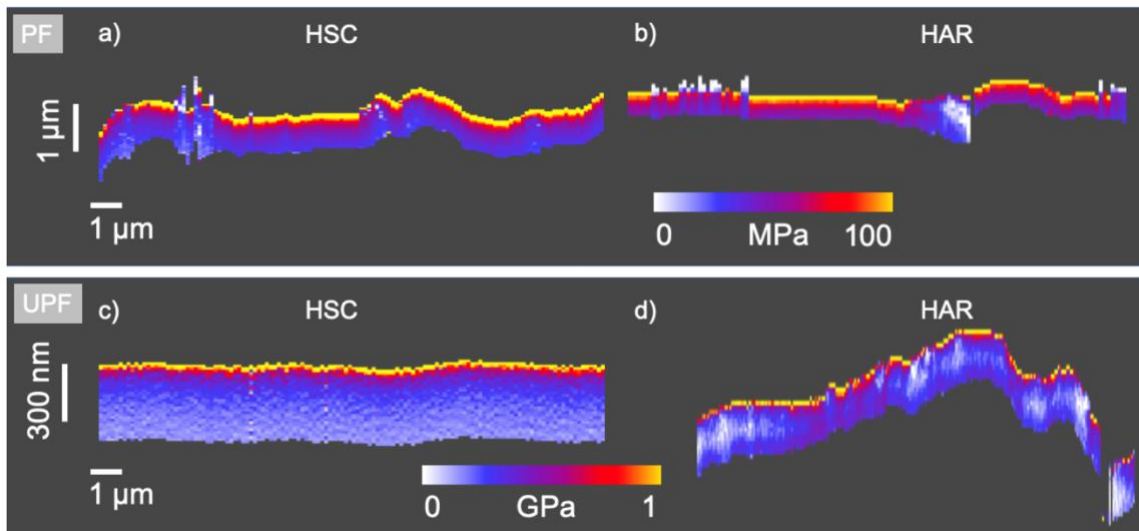


Figure 41: Depth profile of $E_{lok}(z)$ in the xz -direction of a PF mapped with an HSC cantilever in a) and an HAR cantilever in b) and of UPF mapped with an HSC cantilever in c) and an HAR cantilever in d).

In Figure 41a), the depth profiles of $E_{lok}(z)$ in the xz -direction of a PF mapped with a HSC cantilever in a) and with a HAR cantilever in b) are shown. Both depth profiles exhibited a hard layer, shown in yellow. The hard layer on the top exhibits a value of 95 ± 15 MPa. A sharp transition between a hard layer (yellow) and softer material (red and blue) can be identified. Thus, a stiffness gradient from the fibre surface to the softer interior was observable. $E_{lok}(z)$ was calculated for each data point, for a total of 128 profiles. All of them showed the same behaviour with the hard layer at the surface and sharp transition to the softer layer beneath. To Figure 40b), where the topography and the profiles of $E_{lok}(z)$ are shown for another cross section. Additionally, here, a hard layer (yellow) can be identified above the softer layers (red and blue). Thus, it is reasonable to assume that the PF is covered by a hard layer (or several hard layers that could not be resolved). Beneath this top layer, $E_{lok}(z)$ decreases with further indentation depth. Cross sections of the $E_{lok}(z)$ of PF are shown in Figure 42b). Note 9 spots of every fibre type were investigated and the cross sections in Figure 41 are representative cross sections only. As UPF and PF are natural occurring fibres it is not expected them to own the same roughness at the surface.

However, in the fibre or pulp treatment process, the P wall is usually milled off. Thus, it has to be excluded that the hard layer on top in the PF presents the S2 layer. To verify this, force-volume mapping was applied to the UPFs. The UPFs were directly extracted from a natural cotton boll and therefore raw and unprocessed, which means that all layers should be intact. In Figure 41c), a depth profile of $E_{lok}(z)$ in the xz -direction mapped with an HSC cantilever

and in d) mapped with a HAR cantilever are shown. From Figure 41c) and d), it can be seen that the UPF possessed a hard layer (yellow) on the fibre surface with softer layers beneath (colour coded in red and blue). The $E_{lok}(z)$ in the xz -direction decayed with increasing indentation depth. Compared to the PF, the UPF exhibits a harder layer on the surface at 1 GPa. The indentation depth in all measurements was sufficient to reach the S2 layer depth, i.e., at least 300 nm. However, it was observed that the indentation depth in the UPFs was not as high as that in the PFs. Cross sections of the $E_{lok}(z)$ of UPF are shown in figure 6a). The recorded profiles in Figure 42a) and b) are recorded at different spots on different fibres.

The trend of the depth profile of UPF is interpreted as follows: In UPF, all layers should be intact. Therefore, the hard layer (yellow) on the top most likely represents the $E_{lok}(z)$ of C with incrustations (eventually with a slight crosstalk caused by P). Layer C is a waxy layer containing cutin, waxes and cell wall polysaccharides, which is assumed to be harder than the layer beneath it, which is embossed by the fibril structure of cellulose. The slightly softer layer beneath (red) might directly represent the P wall. In comparison to the C layer, the $E_{lok}(z)$ in the P wall is reduced because it contains additives to waxes, such as lignin, minerals and cellulose fibrils. Compared to the S layers, which are predominantly constructed of cellulose fibrils, the P wall with waxes, lignin or minerals is therefore harder. At the indentation depth, where S1 and S2 should be present, $E_{lok}(z)$ decayed noticeably.

Regarding the question of what happens to the fibres when they are processed into paper fibres, it is proposed the following: In the PF, a maximum average value of $E_{lok}(z)$ 87 ± 16 MPa was measured (hard layer on the top). In UPF, this $E_{lok}(z)$ value is reached at an indentation depth of 235 ± 58 nm. As the depth of S2 should be 300-500 nm, this result suggests that in PF, C was completely removed during the paper production process. Additionally, the P and S1 layers were slightly milled off in PF, and the lignin content decreased. However, the data indicate that the P and S1 layers were not completely removed during paper production, as the $E_{lok}(z)$ of the S2 layer was not reached in the first 200 nm. Since the P wall has a thickness of 100-200 nm, as does the S1 layer, it can be assumed that both layers could still be partially intact.

In in Figure 42c), further cross sections of $E_{lok}(z)$ UPF (in red) and PF (in blue) are shown (150 profiles for UPF and PF each). The suggested corresponding wall layers are indicated with different colours in the graph (see C, P, S1, S2). The C layer is highlighted in dark blue, the P wall in blue, the S1 layer in light blue and the S2 layer in grey. in Figure 42c) represents the suggested $E_{lok}(z)$ trend inside the fibre. The cross sections of $E_{lok}(z)$ of the PF begin where the $E_{lok}(z)$ value of the UPF fibre is matched.

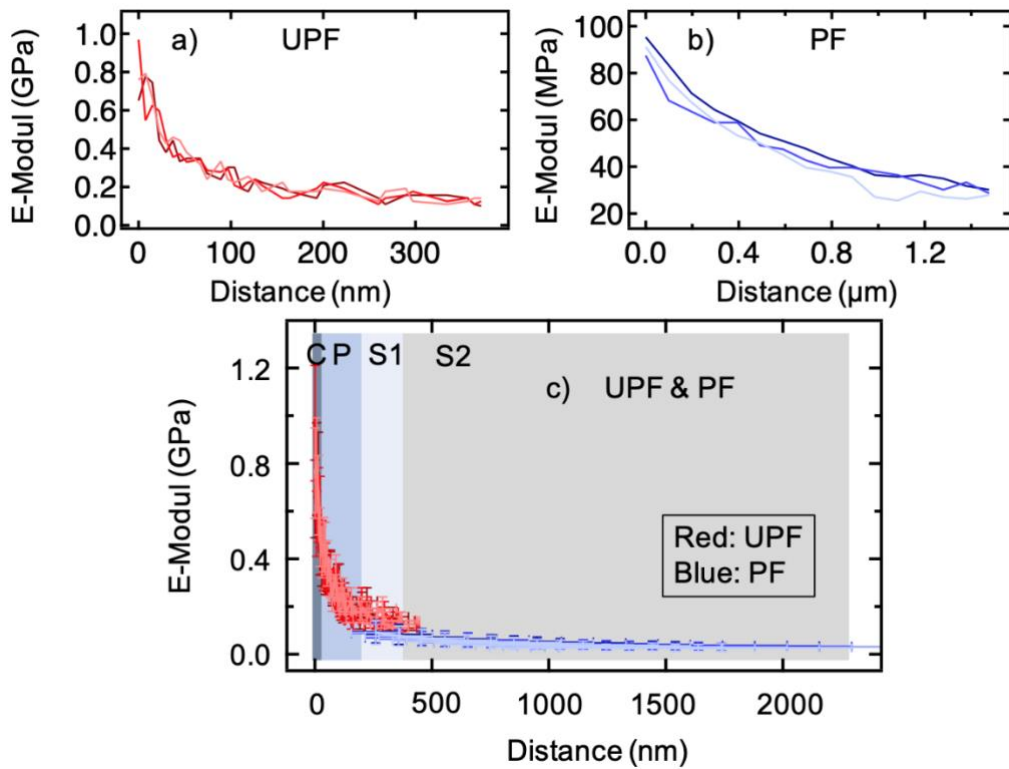


Figure 42: Depth profiles of this $E_{lok}(z)$ of a) a UPF, b) a PF and c) a combined graph of UPF and PF. In c), the UPF profiles are plotted in red, and the PF profiles are plotted in blue. The suggested corresponding wall layers are indicated with different colours. The C layer is highlighted in dark blue, the P wall in blue, the S1 layer in light blue and the S2 layer in grey. The error bars are $\pm 30\%$ of the values. The 3 profiles in a) and b) were extracted from cross sections with a HSC cantilever. The profiles in c) were extracted with both cantilever types.

4.3.2 Verification of fibre wall structure by fluorescent protein markers

To verify the suggested wall structure, UPF and PF were labelled with fluorescence protein-tagged CBMs. It was used: CBM77 (binds to pectin, shown in green), CBM3a (binds to “semi-crystalline” cellulose, shown in cyan) and CBM1Cel6a (binds to crystalline cellulose, shown in red). 3D confocal fluorescence microscopy images of UPF and PF are shown in Figure 43a) and b).

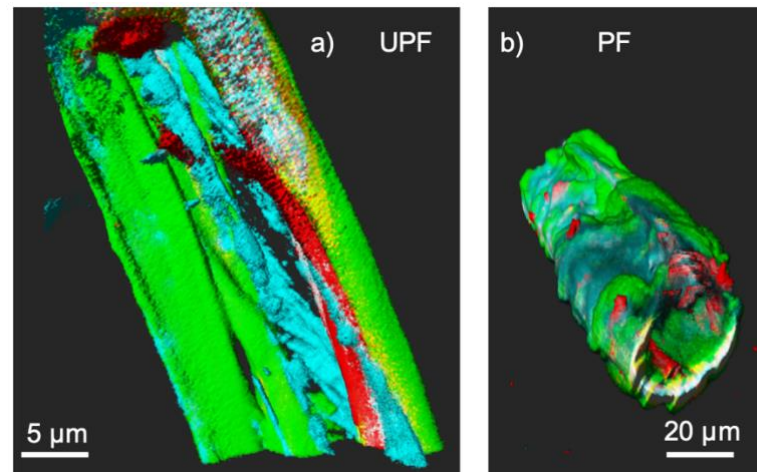


Figure 43: 3D images of confocal fluorescence microscopy imaging. The fibres are labelled with CBM77 in green (binds to pectin), with CBM3a in cyan (binds to “semi-crystalline” cellulose) and with CBM1Cel6a in red (binds to crystalline cellulose). a) UPF fibre and b) PF fibre.

Both fibre types exhibit a green (pectin) outer layer with cyan (semi-crystalline cellulose) parts and a red (crystalline cellulose) fibre interior (see Figure 43). Intensity cross sections on single confocal planes reveal the order in which the three labelled components are arranged within a fibre wall (Figure 44). By analysing the peak position of the labels, it is found that for UPF, the order is green, blue, green and red, i.e., pectin, semi-crystalline cellulose, pectin, and crystalline cellulose. The pectin signal is found on the outside and decays towards the fibre interior but is not found on the inside of the fibre wall. The signal for semi-crystalline cellulose, in turn, is found only in the fibre wall’s interior, and the signal for crystalline cellulose is found only inside. In mature fibres, the P wall contains pectin, hemicelluloses, disordered cellulose fibres and lignin, and the S1 layer of the secondary cell wall has portions of pectin and hemicelluloses in addition to densely packed parallel cellulose microfibrils. Thus, both layers should occur in green but can also occur in blue, as both walls also contain “semicrystalline” cellulose. Therefore, it can be assumed that the green and blue intensity peaks represent the P wall and S1 layer. The crystalline cellulose is marked in red and can be attributed to the S2 layer of the secondary cell wall.

In contrast, in PF, the intensity peaks of the three components are closer together, but their signal distribution is broader. Similar to UPF, the order of the intensity peaks occurring towards the fibre interior is green, blue and red. However, in PF, only one peak is found for the green signal, which is consistent with the milling off of parts of P and S1 during the paper production process.

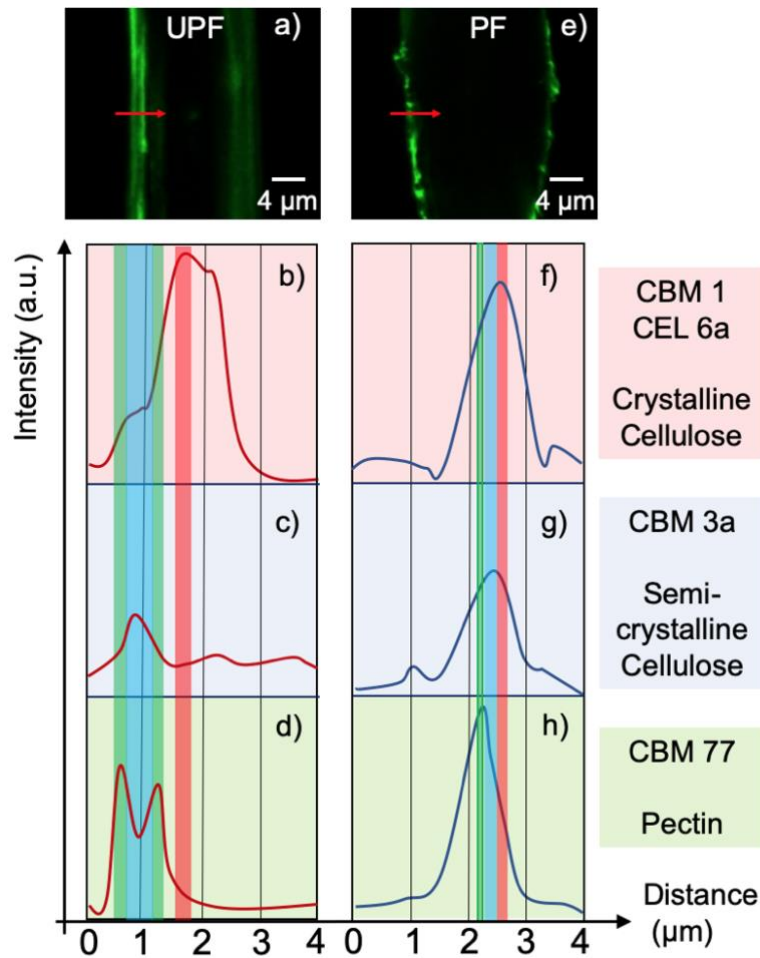


Figure 44: a) Image slice of the confocal fluorescence imaging of a UPF. The intensity peaks over the distance of the CMBs in the UPF are shown in b) for CBM1Cel6a, in c) for CBM3a and in d) for CBM77. In e), an image slice of the confocal fluorescence imaging of a PF is shown. The intensity peaks over the distance of the CMBs in the PF are shown in f) for CBM1Cel6a, in g) for CBM3a and in h) for CBM77. The peaks of the corresponding CMBs are marked in the green (CBM77), blue (CBM3a) and red (CBM1Cel6a) boxes.

It was not possible to label the C layer or the different layers P, S1, S2 individually with CBMs. The measured intensities and intensity peaks could therefore also display a mixture of the different layers of walls. Furthermore, the fluorescence CLSM images have a lateral resolution

of 250 nm and an axial resolution of 500 nm. Thus, it is not possible to assign the $E_{lok}(z)$ measured with AFM directly to the different wall layers with confocal microscopy. However, the measured order of the occurring intensity peaks and the correlation of the labelled parts with the predicted fibre structure strongly supports our interpretation of the AFM measurements.

In the literature, tensile testing showed that an intact S2 layer is the most important factor for the mechanical properties of the fibres (140, 141). From nanoindentation experiments, it was inferred that the elastic modulus of the S2 layer should be higher than the elastic modulus of the other walls (144). Merely, in the work of *Bergander and Salmen* (142), the transversal elastic modulus was not highly dependent on S2 but on S1 and S3. The presented results in this work indicate that the hardness of the walls/layers and the corresponding meaning of the mechanical properties must be divided in the transverse and longitudinal directions. In tensile tests, the longitudinal elastic modulus of the fibres is determined by pulling at both ends of the fibres. The fibril structure of the S2 layer in the fibre is therefore oriented in the tensile direction. Hence, a higher resistance in the tensile direction is achieved. In contrast to the tensile test, in the force-volume mapping method, the fibre is not pulled at either end, but the stiffness at depth is measured by nanoindentation. Thus, the loading direction is perpendicular to the orientation of the fibrils of the S2 layer (Figure 45b). Due to the geometry of the indenters used in conventional nanoindentation experiments, it is not possible to obtain a lateral resolution, as it is by the AFM force-volume mapping method. The difference in the arrangement of the applied force in relation to the fibril orientation in the S2 layer in the fibre is shown in Figure 45. The presented results are in line with *Bergander and Salmen* (142), who showed that the transversal elastic modulus does not depend on S2. This leads to the interpretation that a cellulose fibre is resistant to tensile forces mainly due to the orientation of the fibril structure in the S2 layer in the tensile direction. The resistance against compression forces is due to a hard layer on top of the surface, i.e., the fibril structure in the P wall.

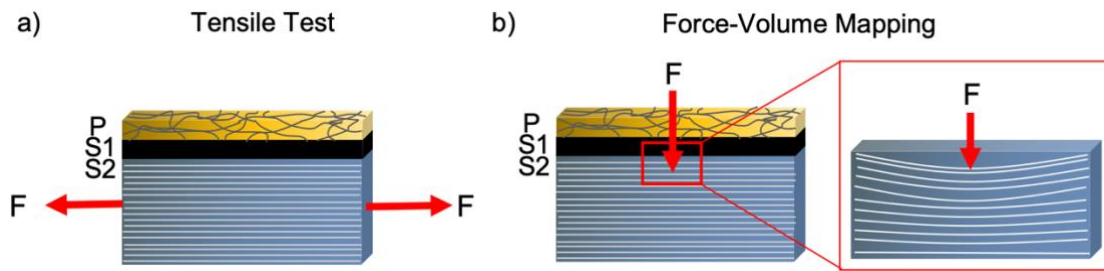


Figure 45: Fibril orientation in the applied load direction in a) the tensile test and b) force-volume mapping. In the tensile test, the fibrils of the S2 layer are oriented parallel to the applied force. In the Force-Volume Mapping, the fibrils of the S2 layer are oriented perpendicular to the applied force. Thus, the fibrils from the S2 layers can be bend down locally as shown in figure b).

(Note: NOT the whole fibre is bent down.)

4.3.3 Subsurface properties of hydrated fibres

In the next experiment, PF and UPF were hydrated to investigate the difference in indentation depth and behaviour of the layered wall structures of the fibres.

In Figure 46, the cross sections of $E_{lok}(z)$ in the xz -direction of a hydrated PF mapped with an HSC cantilever (a) and with a HAR cantilever (b) are shown. A cross section of a hydrated UPF is displayed in c) mapped with an HSC cantilever and in d) mapped with an HAR cantilever.

The hydrated PF exhibited fewer areas with a hard top layer on the fibre surface (yellow). In most parts, the PF showed areas that were attributed to a softer $E_{lok}(z)$ (blue or white). In these volume segments, the water molecules could break hydrogen bonds, which resulted in a softening of the fibre (13-16). In only a few areas, the layered structure, observed in the dry state, was visible. Therefore, it is interpreted that in the hydrated state, the layered wall structure of the PF becomes indistinct. The bonding between the fibrils in each layer could be weakened due to the weakening of the H-bonds. Thus, a possible interpretation is that an intact wall structure in each layer cannot be sustained in the wet state. In the hydrated state of the UPF (Figure 46c and d), a layered structure in the $E_{lok}(z)$ was observable in most parts of the cross section of the fibre. In contrast to the PF, the UPF seemed to preserve the layered wall structure in the hydrated state, which is suggested to be due to the intact C layer and P wall, which prevent the UPF from excessive softening in the hydrated state. The higher maximum value of $E_{lok}(z)$ in the UPF compared to the PF supports this consideration. However, the maximum value of $E_{lok}(z)$ in the hydrated UPF exhibits a lower value than in the dry state. As shown in Figure 46, the indentation depth of a PF in the hydrated state is higher than that of the UPF.

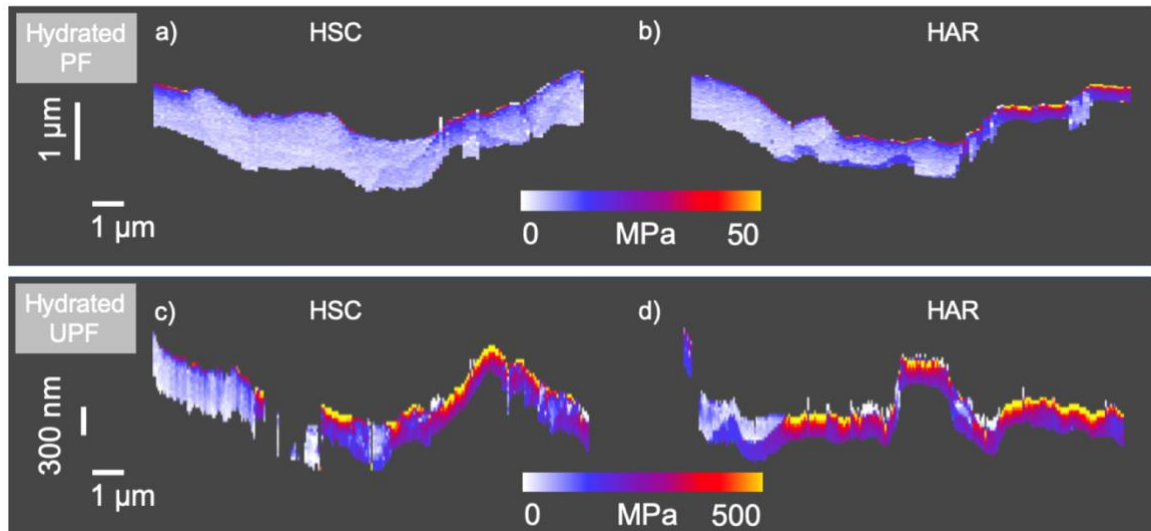


Figure 46: Cross section of $E_{lok}(z)$ in the xz -direction of a hydrated PF mapped with a) an HSC cantilever and b) an HAR cantilever. Cross section of $E_{lok}(z)$ in the xz -direction of a hydrated UPF mapped with c) an HSC cantilever and d) an HAR cantilever.

4.3.4 Comparison of dry and wet state subsurface properties

At next, the indentation depths in the dry state of both fibre types were averaged and normalised to be equal to 1. Then, the indentation depths in the wet state of both fibre types were averaged and set in relation to the dry state (equals to 1) to get a measure of the loss in stiffness of the fibre types. In both fibre types, a decay of the normalised indentation in the hydrated condition was observable. The decrease in the normalised indentation in the wet state compared to the dry state of the PF ranged from 1 to 0.16 ± 0.14 and hence was larger than the decrease in the UPF to 0.81 ± 0.05 . Thus, the tip could indent into the PF deeper in the hydrated state than into the UPF. This is attributed to the fibre or pulp treatment before the paper-making process. As mentioned before, the C and small amounts of P are removed during the fibre or pulp treatment process in the PF. Therefore, predominantly cellulose-based layers are present. Hence, the normalised indentation in the PF is attributed to the greater softening of the entire cellulose-based fibre. In contrast, in the UPF, the wax-like layer C and the wax-, pectin- and lignin-containing P wall are still intact (162). With the intact composition and structure in the UPF, the water molecules cannot easily diffuse into the fibre. This can be seen as a natural hydrophobization to prevent massive water uptake into the UPF. Additionally, the standard deviation of the UPF was ± 0.05 lower than that of the PF (± 0.12). The more uniform behaviour is consistent with an intact layer structure. As all UPFs were extracted from a natural, raw cotton boll, and the fibres had the same unprocessed layer structure. Thus, these measurements were completed with reproduceable samples, unlike the processed PF. In the fibre or pulp treatment process, the PF pass processes, such as beating

or pressing, where the original fibre structure is randomly destroyed in each fibre. Thus, the higher standard deviation in the PF originates from statistics in the fibre or pulp treatment before the paper-making process.

Note: It has to be pointed out that in Figure 46d) exemplarily the stiffer top layer is absent. This shows the natural character of the fibres. No fibre is like the other fibre. Also, as the fibres are grown naturally, it could happen that the growth process possesses some errors and some wall layers are not built successfully. Furthermore, the extraction of the fibres from the cotton boll/paper sheet could also lead to damages of the fibre layers.

However, all depth profiles (Figure 42) are drawn at spots, where the whole layer structure seemed to be intact.

4.3.5 Influence of tip geometry

Furthermore, the influence of the cantilever tip system geometry was probed. An HSC and an HAR cantilever were used to investigate the indentation behaviour. The setpoint for both cantilevers was 3000 nN. A higher indentation depth was reached with the HSC cantilever. The difference between the two indentation depths was 18 ± 6 %. It was interpreted that with the HAR cantilever, the cantilever could not displace as much volume with its lower spring constant as the HSC cantilever.

Moreover, considering the shown force-distance curves with the $\delta^{\frac{3}{2}}$ and δ fit in Figure 78, Figure 79, Figure 80 and Figure 81 the choice of the tip geometry seems to play a role in analysing the measurements. The local fits of $\delta^{\frac{3}{2}}$ and δ (images b), c) for HSC cantilevers and e), f) for HAR cantilevers) are shown in the black curves. The blue points are the recorded indentation points for the applied forces. In every fibre type and dry and wet state the local fits of the HAR cantilever seemed not as accurate as for the HSC cantilever, especially at the contact region between tip and sample surface. There it is visible that the fits in the contact region of the HAR cantilever lead to a higher stiffness. As stated in *Dokukin and Sokolov* sharp tips such as the HAR cantilever could lead to a plastic deformation, which could lead to the measurement of a stiff surface layer (163).

As this stiff layer on the fibre surface with the HSC cantilever was detected, it was assumed that the hard layer is present on the fibre surface. However, the choice of the cantilever-tip system should be the HSC.

But, in all measurements, the desired indentation depth was reached.

Figure 82 shows that the force-volume mapping method does not leave an imprint on the fibre surface in the scanned area with both types of cantilevers in the dry and wet states.

4.4 Conclusion

AN AFM-based method to assess the intrinsic mechanical properties of cellulosic fibres (processed linter and unprocessed cotton) was discussed. With the local analysis of recorded static force-distance curves, it was possible to measure the local elastic moduli at the fibre surface and 950 nm beneath the surface. This approach was used to investigate how fibre or pulp treatment before paper making affects the mechanical properties of cotton linter fibres at the surface.

In a combined 3D representation, topographic features could be directly related to the local mechanical properties. Dry fibres had a stiffer outer layer (higher $E_{lok}(z)$) on the fibre surface with softer material (lower $E_{lok}(z)$) beneath. The surface of UPF was stiffer than that of the processed fibres. For hydrated fibres, however, differences in the stiffness profile between the processed and unprocessed stiffnesses were found. The maximum indentation depth was much higher for the processed fibres than for the unprocessed fibres. This observation can be explained assuming that during the fibre or pulp treatment process, the C layer and perhaps the P wall were affected in the milling process. Thus, the processed fibres exhibited a lower $E_{lok}(z)$ layer on the fibre surface than the unprocessed fibres where the wall structure was intact. Assuming that intact wax-containing cuticle (C) and primary cell walls (P) serve as protection against intruding water molecules explains why the mechanical properties of the unprocessed fibre were less affected by hydration than those of the linter.

These findings are supplemented by microscopic observations. On the one hand, the data indicate that the P wall is missing in PF, as the external pectin signal is missing but the primary wall would have a high proportion of it. On the other hand, they show that the fibre wall in PF is less clearly layered than in UPF, as the signal intensity peaks are much closer together and at the same time broader than in UPF. Hence, processing not only removes the P wall but also affects the clear stratification and orderly structure of the fibre wall. Compaction, in turn, may result if a structurally challenged wall swells and is then dried during the paper-making process.

To investigate the influence of tip and cantilever properties on the results, data obtained with (relatively soft) cantilevers with high-aspect-ratio tips were compared to data obtained with a high spring constant cantilever with a standard tip. With both approaches, i.e., either using stiff cantilevers or using high aspect ratio tips, an indentation depth of a minimum of 300 nm could be achieved, and the mechanical stiffness was probed as a function of indentation depth. A higher maximum indentation depth was achieved using the hard cantilever HSC.

The subsurface imaging method proved to be a valuable tool for surface near depth-sensitive mapping of the local stiffness of cellulosic fibres. Local, i.e., lateral and vertical variations in

the mechanical properties could be investigated and related to features of the fibre wall. Furthermore, the recovering behaviour of the layered wall structure from the hydrated to the dry condition and the potential fatigue could be investigated with the presented AFM-based method.



5

Nanomechanical Characterisation of a Water-repelling Terpolymer Coating of Cellulosic Fibres

After describing the properties of single cellulosic fibres in dry, humid or wet state this chapter focusses on preventing the discussed losses in mechanical properties in humid/wet state. The increase of wet-strength of cellulosic fibres could be archived via a hydrophobic polymer coating.

Here, the effects of a terpolymer P(S-co-MABP-co-PyMA) coating on cotton linter and eucalyptus fibres to improve the resistance of cellulose fibres against humidity is investigated. Coated and plain fibres were characterised by using SEM, CA measurements, Raman spectroscopy and AFM measurements with the objective of correlating macroscopic properties such as the hydrophobicity of the fleece with microscopic properties such as the coating distribution and local nano mechanics. The SE and fluorescence microscopy results should reveal the distribution of the coating on the paper fleeces and fibres. CA measurements proved the hydrophobic character of the coated fleece, which was also confirmed by Raman spectroscopy measurements that investigated the water uptake in single fibres. The water uptake also induced a change in the local mechanical properties, as measured by AFM nano indentation method and the quasi-static PeakForce Tapping method. These results verify the basic functionality of the hydrophobic coating on fibres and paper fleeces but call into question the homogeneity of the coating.

Parts of this chapter have been published as:

“Nanomechanical characterisation of a water-repelling terpolymer coating of cellulosic fibres” by Auernhammer, J.*, Bell, A.K*, Schulze, M. *et al.* in *Cellulose* **28**, 2149–2165 (2021).
<https://doi.org/10.1007/s10570-020-03675-9>

5.1 Introduction

To control the wetting properties, paper fibres or the entire fleece can become hydrophobic with the application of polymer coatings (11, 164) or modified with TiO₂ nanoparticles or fluorinated silanes to obtain self-cleaning surfaces used for the separation of different liquids, such as water and oil (165-168). To improve the strategies to strengthen wetting properties, it is essential to understand how these coatings change the mechanical and wetting properties of individual cellulosic fibres.

The efficiency of coating strategies and the uptake of liquids into cellulose fibres are issues that have been successfully addressed with various characterisation methods. The distribution of coatings on fibres and the distribution in the fibre network can be investigated with fluorescence microscopy (4, 11). Raman spectroscopy was applied by *Fechner et al.* (169) and *Eronen et al.* (170) to study changes in the molecular structure of cellulose caused by water or sodium hydroxide. In a more comprehensive approach, coated cellulose fibres were investigated with the help of brightfield microscopy, Raman spectroscopy and confocal laser scanning microscopy (11). AFM has been used to investigate the surface properties of cellulose-based materials in dry and wet states (112, 171, 172). Further nanoindentation experiments have been carried out to study the elastic modulus of wood cells (144) or that of dry pulp fibre walls (173). In 2013, Yan *et al.* used the classic *Oliver-Pharr approach* (174) for the investigation of the instantaneous elastic modulus (175). In 2014, *Ganser et al.* described the hardness and modulus of pulp fibres via AFM-based nanoindentation as a function of the relative humidity (176) and, in 2015, compared the results with viscose fibres (111).

Herein, the effect of humidity on plain cotton linter paper (LP) and eucalyptus sulphate paper (EP) fibres, as well as P(S-co-MABP-co-PyMA) coated LP and EP fibres is reported. Its fluorescent component (PyMA) allows for the mapping of the polymer distribution. For the experiments, papers made of LP and EP fibres were coated, and their properties in comparison to those of unmodified paper samples were investigated. LP consists of 94-95 % cotton and serves as a model system (34, 37). The chemical composition of EP is more complex than that of LP, with EP having a cellulose content of only 42 % and additional hemicellulose and lignin (37). The functionality of the water-repelling polymer coating was investigated by macroscopic (CA goniometry and fluorescence microscopy) and microscopic (Raman spectroscopy, SEM and AFM) methods to reveal the response of the different samples to humidity at a large scale.

5.2 Materials and Methods

5.2.1 Materials

Cellulose fibres were extracted from LP and EP sheets, which were prepared according to DIN 54358 and ISO 5269/2 (the Rapid-Köthen process). The hydrophobic, UV-active, and fluorescent terpolymer P(S-co-MABP-co-PyMA) was used as hydrophobic coating. Specifically, the PyMA part of the terpolymer was fluorescent. The coating was applied by dip coating the paper samples, according to the procedure described in the literature (47, 177). Briefly, the polymer was dissolved in tetrahydrofuran (THF) and in a solution applied *via* the dip coating process. After drying, the coated paper sheets were irradiated by UV light (365 nm) to connect the benzophenone units with each other and with the cellulose, and excess polymer was removed by THF Soxhlet extraction; this suggests that all remaining fibre-attached polymers are chemically stable, and it can be proposed that it is thermally stable up to 300 °C, as the polymer is an organic material (47, 177, 178).

5.2.2 Methods

5.2.2.1 Contact Angle Goniometry

For the contact angle goniometry (CA) measurements, a CA goniometer (OCA, DataPhysics Instruments, Filderstadt, Germany) was used. A static Milli-Q water droplet with a volume of 2 µl was placed on the sample. The CA was determined *via* Young-Laplace alignment 1 s after drop generation.

5.2.2.2 Scanning Electron Microscopy

A conducting gold layer was sputtered (Balzer SCD 050, BAL-TEC AG, Balzers, Lichtenstein) onto the samples with a supply current of 30 mA for 75 s. For SEM imaging, a Philips XL30 FEG high-resolution electron microscope was used with an electron voltage of 10 kV at 1500x magnification and 10000x magnification (Figure 51).

5.2.2.3 Fluorescence Microscopy

Fluorescent images were taken using a Zeiss AXIO observer Z1 optical microscope equipped with a Zeiss Colibri.2 illumination system and a Zeiss HSM Axiocam camera (Carl Zeiss Microscopy GmbH, Jena, Germany). All images were processed using Zeiss Axiovision SE64 software. Images were taken in the standard epifluorescence configuration and in transmitted white light mode for bright field microscopy. The excitation wavelength was 365

nm, and the emission bandwidth was 435-485 nm (AHF Analysetechnik, Tübingen, Germany, filter set 31-013, DAPI configuration). The acquisition time for the fluorescent light was 1 s with a 5x/0.12 objective lens for the unmodified samples and 10 s with a 5x/0.12 objective lens as well as 2 s with a 10x/0.25 objective lens for the coated samples.

Pieces of paper and small bundles of fibres were analysed by pulling out fibre bundles of the pieces of paper. Papers and fibres were placed on a microscope slide and covered with a cover glass.

5.2.2.4 Raman Spectroscopy

A confocal Raman microscope (alpha300R by Witec GmbH, Ulm, Germany) with a laser wavelength of 532 nm (Nd:YAG-Laser) and a 20x/0.40 objective lens was used throughout the measurements. For reference measurements, small pieces of paper (fibre bundles) were collocated on an object slide to obtain unmodified samples. Raman measurements were taken with 10 accumulations and an integration time of 30 s each.

Point scans (10 accumulations with an integration time of 10 s each) and map scans (25 x 25 μm^2 , 50 x 50 measuring spots with an integration time of 0.005 s each) were acquired for varied states of humidity (humidity experiments). The measurements were taken inside the fibre close to the surface to estimate the amount of water intruding into the fibre.

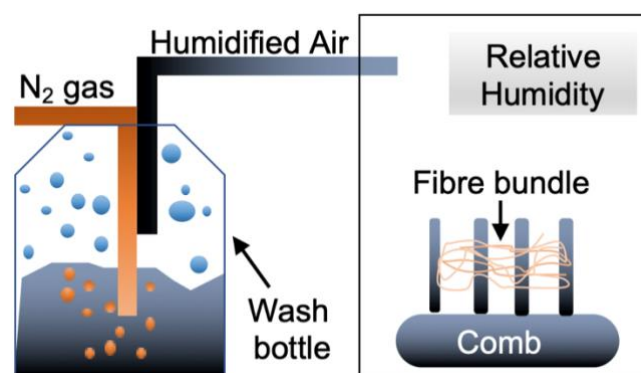


Figure 47: Experimental setup for humidity experiments including a water wash bottle, a N₂ gas inlet, a hygrometer, and a small tooth comb as the sample holder with the fibre bundles.

For the humidity experiments, the paper fibre bundles (2 x 7 mm²) were mounted on a small-tooth comb that was placed in a climate chamber (Figure 47). For every type of sample, three sets of experiments were performed, in which the spectral range from 3200-3500 cm⁻¹, corresponding to the OH stretching vibration, was analysed. In this way, the water uptake in the LP, polymer-coated LP (PCLP), EP, and polymer-coated EP (PCEP) samples could be

recorded. The calculation of the intensity in this region was performed by integration (integrated intensity).

In the first set of experiments, point scans were used, and the Raman spectra were measured first under room conditions (20-60 % RH at 22-24 °C). The second point scan was performed after keeping the sample at 80-90 % RH for 60 min. Subsequently, the RH was reduced to 2-5 %, and the third point scan was recorded after another 60 min.

The second set of experiments included map scans every 60 min. To evaluate potential local drying caused by the heat of the Raman laser, map scans were also performed because the laser radiation is distributed over a large area. The first measurement was taken under room conditions, and the second measurement was taken after 60 min at 80-90 % RH. For the third map scan, a drop of water was added to the sample, and after 15 min, a Raman spectrum was acquired. The last measurement was taken after 60 min at 2-5 % RH.

In the third set of experiments, the adjustment time for RH was 180 min so that the first measurement was taken under room conditions, the second after 180 min at 80-90 % RH, and the last after 180 min at 2-5 % RH.

All experimental data were processed by using WITec Project FOUR 4.0 software. The background of the point scan spectra was subtracted, and the spectra were normalised to the Raman band at 2800-3000 cm⁻¹. From the map scans, an average spectrum of all measurements was calculated and filtered for illustration. From this region, the background was subtracted by a 2nd-order polynomial. From all map scans, an average spectrum was calculated that was then treated like a point spectrum. In this way, the map scans could be compared directly to the point scans.

For the error calculation, the following equation was used:

$$\Delta I = \frac{I}{A} \cdot \Delta A \quad (28)$$

where I is the intensity and A is the Raman band height (amplitude).

5.2.2.5 Atomic Force Microscopy

5.2.2.6 Indentation Experiments

A Dimension ICON instrument (Bruker, Santa Barbara, CA, USA) was used for the indentation and nanomechanical mapping experiments on freely suspended fibres. The indentation experiments were performed using ZEIHR cantilevers with a force constant of 27 ± 4 N/m. The set point was chosen as 300 nN, and the engagement rate was 0.5 Hz. The indentation was recorded *via* static deflection versus separation curves. The inverse optical lever sensitivity (*InvOLS*) was extracted from every curve, as shown in Figure 48b. The *InvOLS* is a relative measure of fibre stiffness plus the cantilever stiffness, with units of nm/V. Thus, the recorded deflection versus separation curves were representative of the resistance of the fibres towards indentation by the AFM probe. Variations in the *InvOLS* linearly correspond to changes in the sample stiffness. Dividing the recorded *InvOLS* by the calibrated *InvOLS* of the cantilever and its force constant allows for the representation of the data in nm/nN, which shows the indentation per applied force (see equation (29)). The cellulose fibres were manually extracted from paper sheets and adhered onto a sample holder that provided a gap $L = 1$ mm between the two attachment points of the fibre. To straighten the fibres, the distance of the gap was adjusted by a micrometre screw. Deflection versus separation curves were acquired at $L/2$ of the freely suspended fibre to minimise any influence of the mounting and prevent any effects due to an asymmetric load. For every type of sample, two results are presented, and every data point is the average from three deflection-versus-separation curves. Two measurement points were taken under room conditions (region I). After hydration of the fibre (a drop of deionised water, which was carefully removed after 30 min of swelling time), data points were acquired in 10-min intervals for a period of 200 min (region II). Then, the fibre was dried in a gentle stream of nitrogen, and two additional measurements were performed (region III). The fibres were freely suspended to homogeneously expose the fibre to humidity/dry air and to guarantee the measurement of the mechanical properties of a single fibre without the influence of a substrate or other connecting fibre bonds.

$$\text{Indentation} \left(\frac{\text{nm}}{\text{nN}} \right) = \frac{\text{InvOLS (Curves)} \left(\frac{\text{nm}}{\text{V}} \right)}{\text{InvOLS(Cantilever)} \left(\frac{\text{nm}}{\text{V}} \right) \cdot k \left(\frac{\text{N}}{\text{m}} \right)} \quad (29)$$

5.2.2.7 Nanomechanical mapping

For nanomechanical mapping, the quasi-static PeakForce-Tapping mode was applied. A ScanAsyst-Fluid+ cantilever from Bruker (Santa Barbara, CA, USA) with a spring constant of 0.9 ± 0.2 N/m was used. The setpoint was chosen as 3 nN, the scan rate was 0.5 Hz, and the amplitude was 300 nm. Single paper fibres were manually extracted from paper sheets, adhered onto 3D-printed fibre holders and put inside a climate chamber of the AFM setup. When measuring the polymer-coated fibres, the paper fibres were primarily investigated with fluorescence microscopy to detect the homogeneous polymer-coated spots on the fibre surface. The chosen RHs were 2 %, 40 %, 75 % and wet conditions (a drop of deionised water on the fibre). The RHs were maintained for 30 min. The deionised water drop was applied and left for 30 min and was subsequently removed carefully with clean tissue. As shown in *Castens et al and Hubbe et al.* (152, 153) the water progress into cotton linter test stripes goes in seconds. Furthermore, *Olejnik et al.* discovered that the free swelling time for a whole pulp was 70 minutes (154). However, *Mantanis et al.* (119) recorded the swelling of cellulose single fibres in water and showed that the equilibrium is reached at 45 minutes. As the fibre surface is for interest only, 30 minutes as “swelling time” for every hydration condition is sufficient. Additionally, the water drop for swelling was removed before the measurement, where the fibre could not swell further then.

The fibre and AFM head were not immersed in water during the measurements. The topography images taken were tilt- and drift-corrected by a first-order plain fit. The mechanical property images were not modified. For analysis of the AFM images, NanoScope Analysis software from Bruker was used. For each fibre type, three different individual fibres were investigated, and on each fibre, three spots were mapped and analysed.

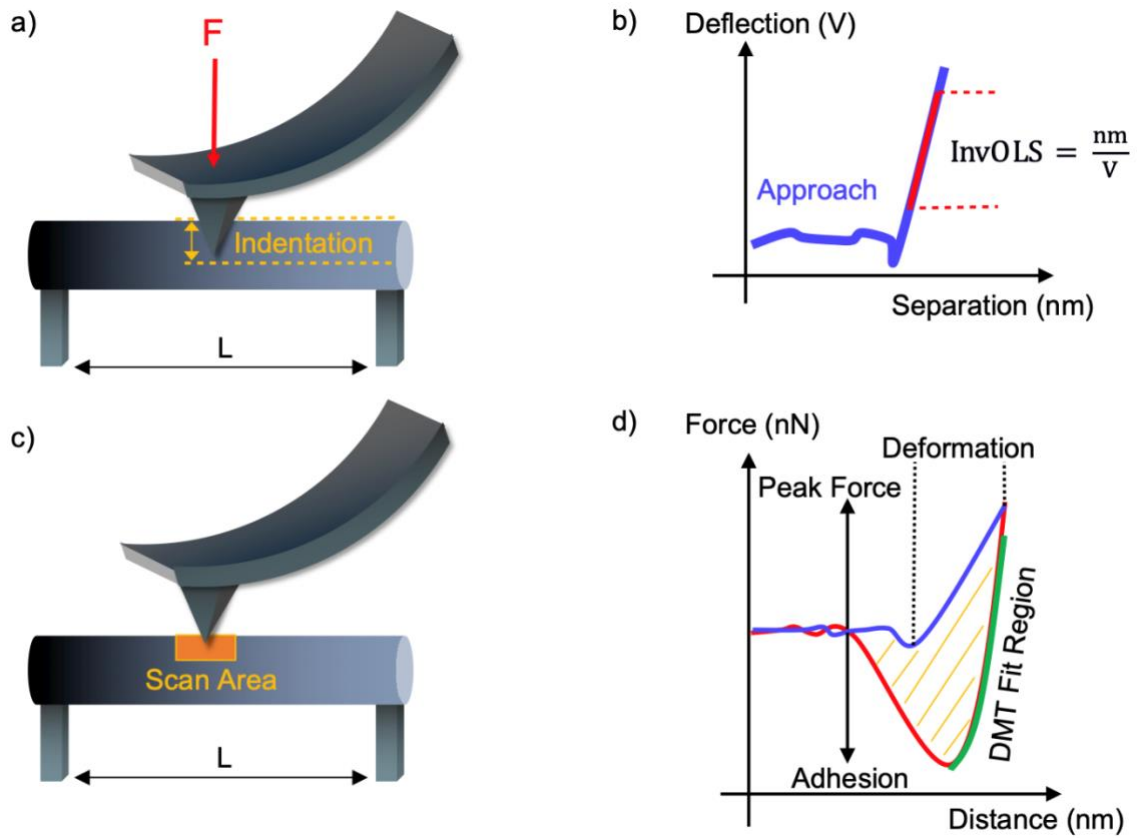


Figure 48: Schematic setup of AFM experiments. (a) Schematics of nanoindentation experiments, (b) deflection versus separation curve with InvOLS shown, (c) schematics of nanomechanical mapping and (d) force versus distance curve with extracted mechanical properties.

5.3 Results and Discussion

5.3.1 Hydrophobicity of terpolymer P(S-co-MABP-co-PyMA)

With the help of static CA measurements, the hydrophobic character of the polymer coating was investigated on a macromolecular scale. The unmodified paper samples adsorbed the water quickly, and videos were recorded to obtain the measurements. These videos were stopped 1 s after the water drop was applied to determine the CA of the different samples. The images of sessile droplets (2 μl of deionised water) on the LP, PCLP, EP, and PCEP sheets for the CA measurements are given in Figure 49.

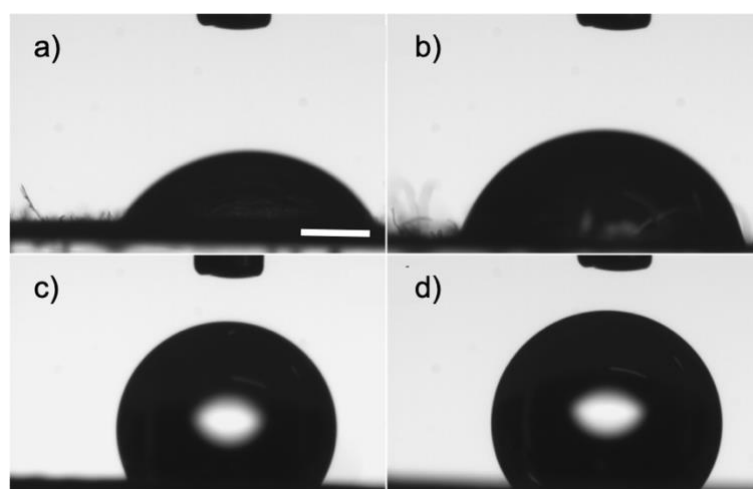


Figure 49: Images of 2 μl water drops on (a) LP, (b) EP, (c) PCLP, and (d) PCEP for CA measurements. The scale bar is 500 μm .

LP and EP showed a hydrophilic behaviour. The imbibition was faster in EP (2 s) than in LP (8 s). On both unmodified samples, the CAs were in the same regime, which was also the case for the polymer-coated samples. The CAs of PCLP and PCEP were in the hydrophobic range, with value of $119^\circ \pm 10^\circ$ and $129^\circ \pm 9^\circ$, respectively, while the CAs of LP and EP showed hydrophilic behaviour with CA values of $79^\circ \pm 10^\circ$ on both materials. On the polymer-coated samples, the water drop was not adsorbed and was much more stable than in the unmodified samples. Additionally, a smoother surface for the polymer-coated samples than for the unmodified samples could be seen, which was also observed in the SEM measurements (Figure 50). These results proved the hydrophobic character of the polymer coating.

5.3.2 Spatial distribution of the polymer coating

SEM was used to visualise the structure of LP and EP and their morphological changes induced by the polymer coating. For all samples, the paper fibres were homogeneously distributed (Figure 51). LP exhibited an increased level of entanglement (Figure 50a) due to a higher number of smaller fibrils than EP (Figure 50b). The polymer coating wrapped the fibres, which was very obvious for the PCLP (Figure 50c), thereby changing the appearance of the small entanglements from single fibres to agglomerated structures. For EP, the number of entanglements also decreased (figure Figure 50d)) because fibres with a smaller diameter were adhered onto fibres with a larger diameter. In Figure 51, overview SEM images at a 1500x magnification are given of all paper and paper-polymer systems.

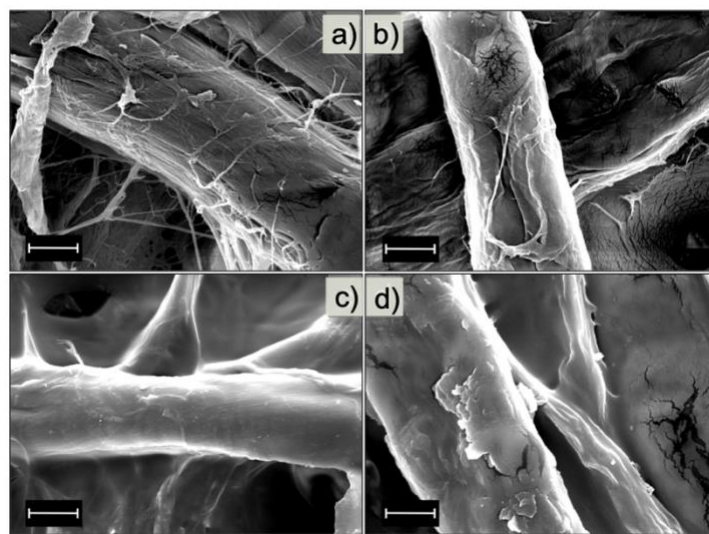


Figure 50: SEM images of sheets made of (a) LP, (b) EP, (c) PCLP, and (d) PCEP. (scale bar: (a,b,d) 5 μ m and (c) 10 μ m).

In Figure 51 the SE images of LP and EP are shown. A higher entanglement is observed for LP (Figure 51a) than for EP (Figure 51b). After the coating the surface is smoother and the entanglements could not be distinguished anymore.

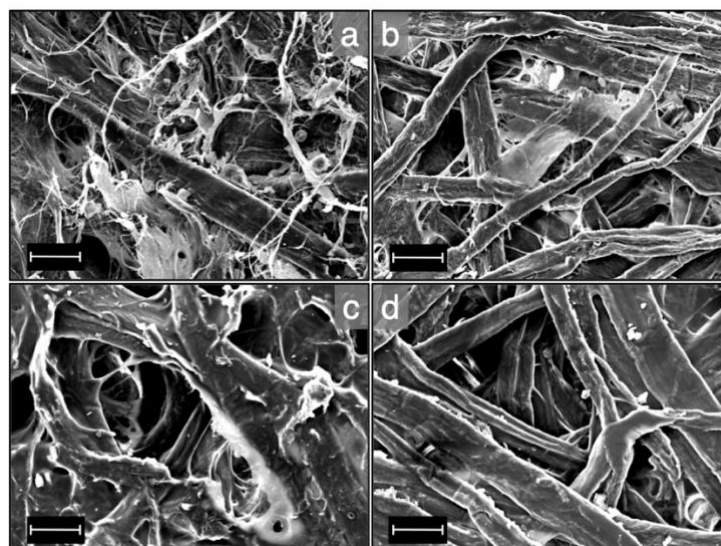


Figure 51: SEM images of a) LP, b) EP, c) PCLP and d) PCEP at 1500x magnification.

The distribution of the polymer on the paper was analysed by fluorescence imaging. The measurements were taken on paper fleeces as well as on small fibre bundles to evaluate the distribution of the polymer. In Figure 52, overlays of bright field microscopy images (grey) and the corresponding fluorescence microscopy images (yellow) are shown.

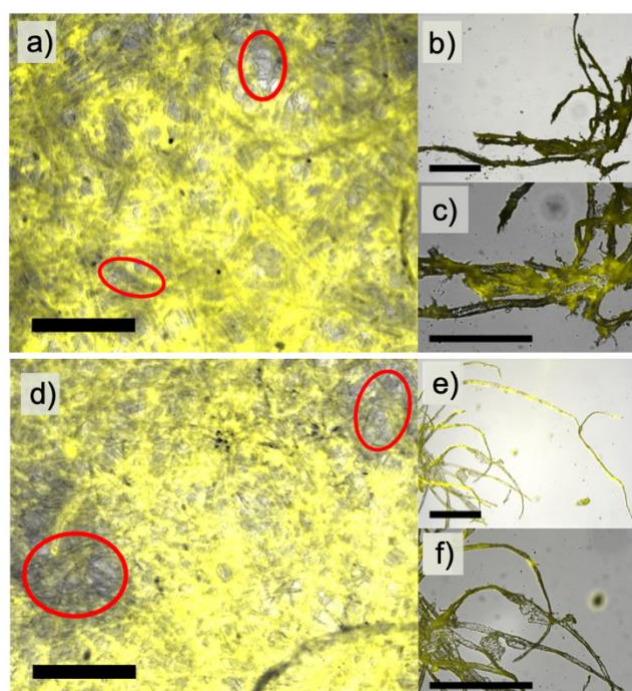


Figure 52: Overlay of bright field microscopy (grey) and fluorescence microscopy images (yellow) at 5x and 10x, showing sheets of (a) PCLP and (d) PCEP, as well as near-surface fibres of (b,c) PCLP and (e,f) PCEP. The scale bar represents 300 μm . The red areas shows regions without a polymer coating, therefore revealing the inhomogeneous coating distribution.

A faint and evenly distributed fluorescence could be seen for the unmodified samples, which was caused by the autofluorescence of the lignin (Figure 53). A higher autofluorescence was noticed on EP because of the higher lignin content in EP than in LP (37). In contrast, PCLP and PCEP exhibited a strong fluorescent signal that was localised along the fibres. Nevertheless, an analysis of the fluorescent signal showed that the fleece was not homogeneously coated (red areas in Figure 52a,d). Additionally, on the level of single fibres, as shown in Figure 52c) and f), the fluorescence signal and thus the amount of coating could vary. The inhomogeneous polymer distribution implies that water could infiltrate not only the unmodified paper but also the coated samples.

In Figure 53 fluorescence microscopy images of LP and EP are displayed. They exhibited a homogeneously distributed, slight fluorescence caused by the background light in the laboratory.

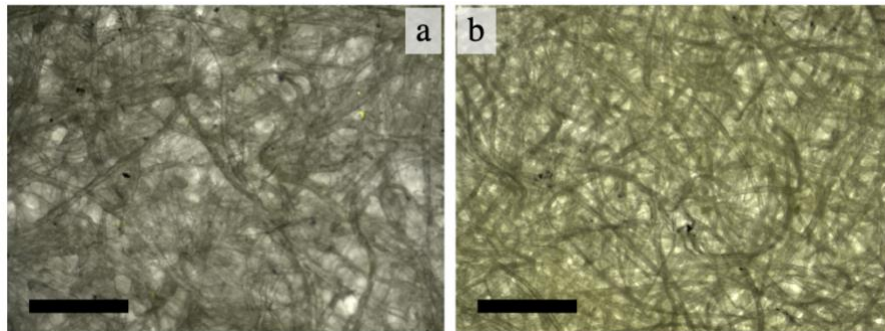


Figure 53: Fluorescence Microscopy images of the unmodified paper samples LP (a) and EP (b). The scale bar represents 300 μm .

5.3.3 Water uptake in plain and polymer coated fibre bundles

Raman measurements were performed to investigate the water uptake in the samples as a function of the moisture and incubation time by observation of the OH band. The reference Raman scans, including the normalised intensity versus Raman shift graphs with the respective vibrational motions, are given in Figure 54. A table of the peak assignments can be found in Table 9. Briefly, the vibrational motions of carbon and oxygen are located in the lower wavenumber regime ($379\text{-}1118\text{ cm}^{-1}$), while peaks at higher wavenumbers ($1290\text{-}3500\text{ cm}^{-1}$) are due to vibrations involving carbon, hydrogen, and oxygen.

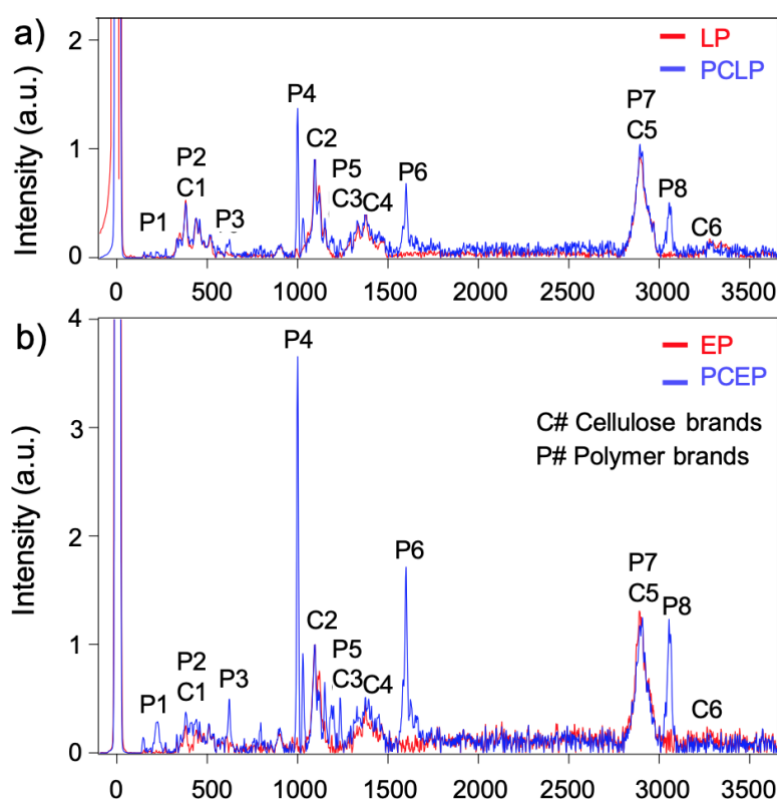


Figure 54: Raman spectra of (a) LP and PCLP and (b) EP and PCEP with assigned cellulose (C#) and polymer (P#) Raman bands. Unmodified paper is given in red, and polymer-coated paper is given in blue. The spectra were taken at $20\times/0.4$ with 10 accumulations and a 10-s integration time each. The measurements were taken on the paper surface where there was a crosslink of paper fibres. The peak assignments can be found in Table 9.

Raman spectra of polymer-coated samples (Figure 54, blue spectra) showed the superposed spectra of paper (Figure 54, red spectra, C# labels) and the polymer (Figure 6, P# labels). The Raman spectrum of the polymer blend P(S-co-MABP-co-PyMA) (Figure 83) shows the superposition of the components PS, benzophenone (BP), and pyrene. For the peak assignments, the peak positions were compared to Osterberg *et al.* for cellulose (179), Brun *et al.* and Hong *et al.* for PS (180, 181), Babkov *et al.* for BP (182), and Xie *et al.* for the pyrene

component (183). The peak positions for all materials are also listed in Table 9 (Supplementary information see chapter 8.3).

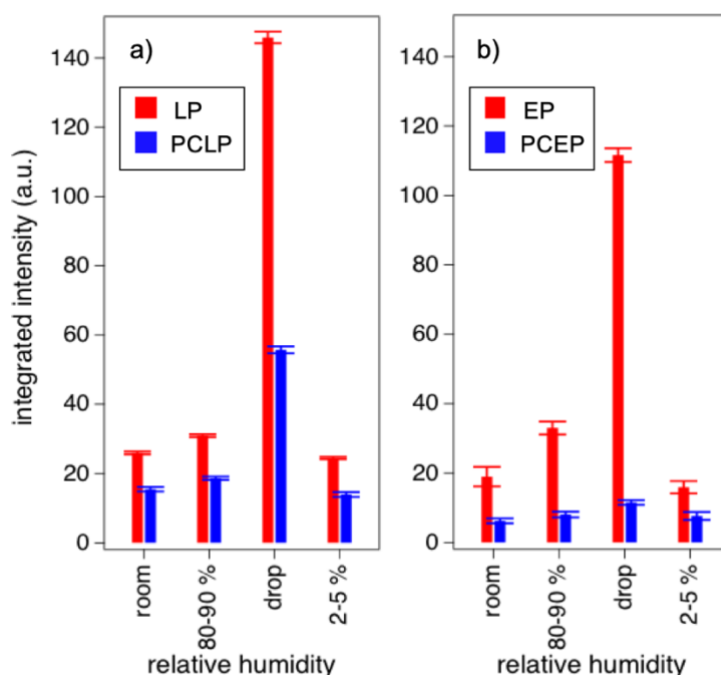


Figure 55: Relative peak intensities of the band assigned to OH stretching obtained in hydration experiments with in situ Raman spectroscopy for (a) LP and PCLP and (b) EP and PCEP. Data of the unmodified paper samples are represented in red (left bar), and the polymer-coated samples are represented in blue (right bar). The integrated intensity is the summed intensity of OH stretching in the spectral region of 3200-3500 cm^{-1} .

To characterise the water uptake, the integrated intensity of the OH band was monitored. Specifically, the OH band was monitored in a region of interest inside the paper fleece but close to the surface. The integrated intensity versus RH graphs in figure 7 and figure S4 correlate with the water uptake. In Figure 55 the integrated intensity is given for room conditions (50 % RH), 80-90 % RH, conditions in which the sample was fully wetted by a droplet and dry conditions at 2-5 % RH.

For the unmodified samples, the integrated intensity of the OH peak was substantially higher after adding the drop of water in comparison to measurements at 80-90 % RH for 60 min or 180 min. This led to the result that the time of exposure to 80-90 % RH was not long enough to fully wet the paper samples. Comparing the experiments after adding the water drop to unmodified samples, it was observed that the water uptake of EP was higher than that of LP, which agreed with the CA goniometry results. The more pronounced uptake of water for EP was explained by the high content of hemicellulose in comparison to LP (37).

For the modified samples, the change in the integrated intensity was predicted to be less distinct than in the unmodified samples because the water should not enter the paper through the polymer coating. In fact, the hydrophobicity of the coating could be confirmed by observing the sliding motion of drops over the sample surface, therefore not being imbibed. Thus, the addition of the water drop did not lead to as much of an increase in the OH peak intensity as that for the unmodified samples. For an increased RH, the change in integrated intensity was also smaller than for the unmodified samples.

The change in integrated intensity was larger for the unmodified samples than for the polymer-coated samples. The results supported the assumption of a hydrophobic character of the cellulose samples after the addition of the polymer coating.

5.3.4 Mechanical property changes in dry and humid states

5.3.4.1 Analysis via indentation experiments

To characterise the variation in the mechanical characteristics of the fibres in the different states of hydration, AFM indentation measurements were performed on individual fibres.

The indentation versus time diagrams were divided into three regions, according to three different states of hydration: (I) fibres under room conditions, (II) soaked fibres, and (III) nitrogen-dried fibres. A higher indentation depth at the fixed deflection point was correlated with fibre softening. The depicted changes in percentage were extracted from the average values of the respective region. The results are shown in Figure 56a) and b). EP fibres underwent softening (76 ± 13 %) from region I to region II with a consequent continuous increase in the indentation. In contrast, PCEP fibres not only showed an increased stiffness in region I but also a reduced softening in the hydrated state (12 ± 6 %) in comparison to EP. The direct comparison of EP and PCEP fibres showed that the polymer coating increased the stiffness of the fibre. The reduced softening was related to reduced water uptake. The indentation values for both samples returned to their respective values (region I) after dehydration (region III). Softening of the LP fibre (38 ± 15 %) when hydrated could be measured. The PCLP fibres were in the same range as the PCEP fibres (0.1 – 0.3 nm/nN) and showed the same softening behaviour (12 ± 5 %) upon hydration. LP fibres showed the highest stiffness among the samples, which was attributed to the higher content of cellulose contained in LP than in EP. This agrees with Baley *et al.* and Gassan *et al.*, who stated that the elastic modulus of natural fibres increases with increasing cellulose (13, 184, 185). Another possible reason for this result is the high portion of crystalline regions in linter, while eucalyptus mostly has amorphous sites. The crystalline regions are expected to be stiffer than

amorphous regions, which could explain the high resistance of the LP fibres against indentation compared to that of the EP fibres.

It can be concluded that the coated samples show less softening when exposed to water than the uncoated samples, which is correlated with less water uptake. Furthermore, the coated samples exhibited a very similar behaviour independent of the underlying fibre material. While the indentation experiments at a single point confirm the functionality of the polymer coating as a water barrier, further AFM experiments are necessary.

In comparison to earlier studies of AFM nanoindentation on fibres (*e.g.*, Ganser *et al.* 2015), the fibres presented here were freely suspended, and their surface was not supported. This setup introduced further degrees of freedom for the fibres to react towards a load, including bending and twisting. Although deflection versus separation curves that indicated movements of the fibre were not considered for evaluation, the combination of probe indentation with movement of the fibre could not be fully excluded. Thus, nanoindentation experiments were not used to calculate the reduced modulus but to show a force-dependent displacement as a measure of mechanical resistance. The results allowed for a qualitative rather than a quantitative comparison between the different states of hydration and thus supported the presented results of the further applied characterisation techniques.

A more comprehensive understanding of the samples requires two-dimensional maps that show the topography and its correlation with the mechanical properties. An identification of crystalline and amorphous regions and their respective modulus as a function of various states of hydration could support or refute the explanation of a stiffer LP due to crystallinity. Additionally, the acquired distribution of the modulus provided by two-dimensional maps can be used to evaluate the representativeness of the previously presented values. Thus, PeakForce-Tapping mode was applied to freely suspended fibres.

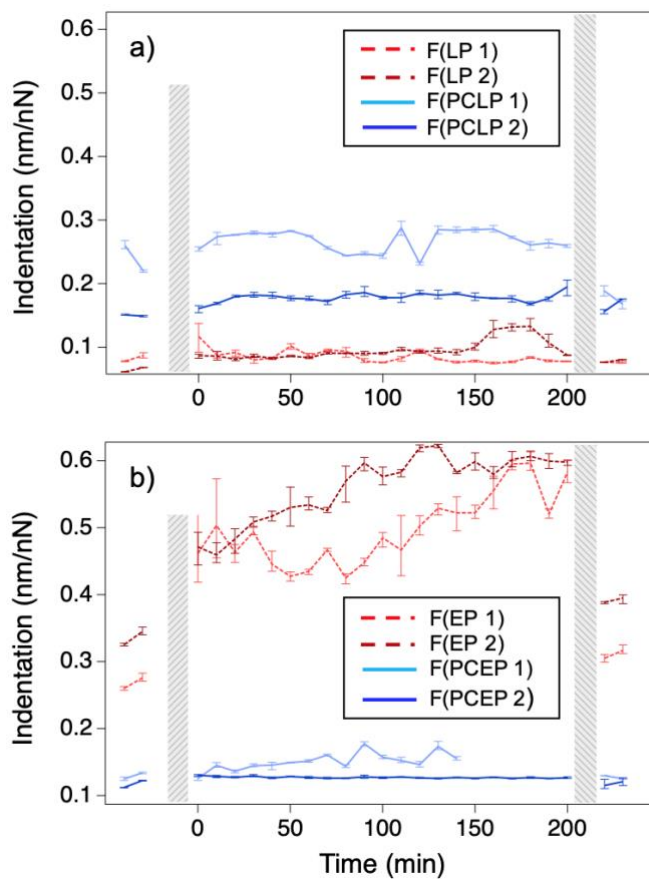


Figure 56: Mechanical resistance against indentation of the AFM probe into (a) LP and PCLP and (b) EP and PCEP in the setup with a fixed distance between attachment points (F). Region I depicts the state under room conditions, region II shows the soaked state and region III is the after-drying state.

5.3.4.2 Analysis via nano mechanical mapping

To investigate the mechanical properties of the paper fibres as a function of the RH, AFM measurements were performed on freely suspended single fibres. For the polymer-coated fibres, fluorescence microscopy was applied before the AFM measurements to identify homogeneously coated regions of interest on the paper fibre.

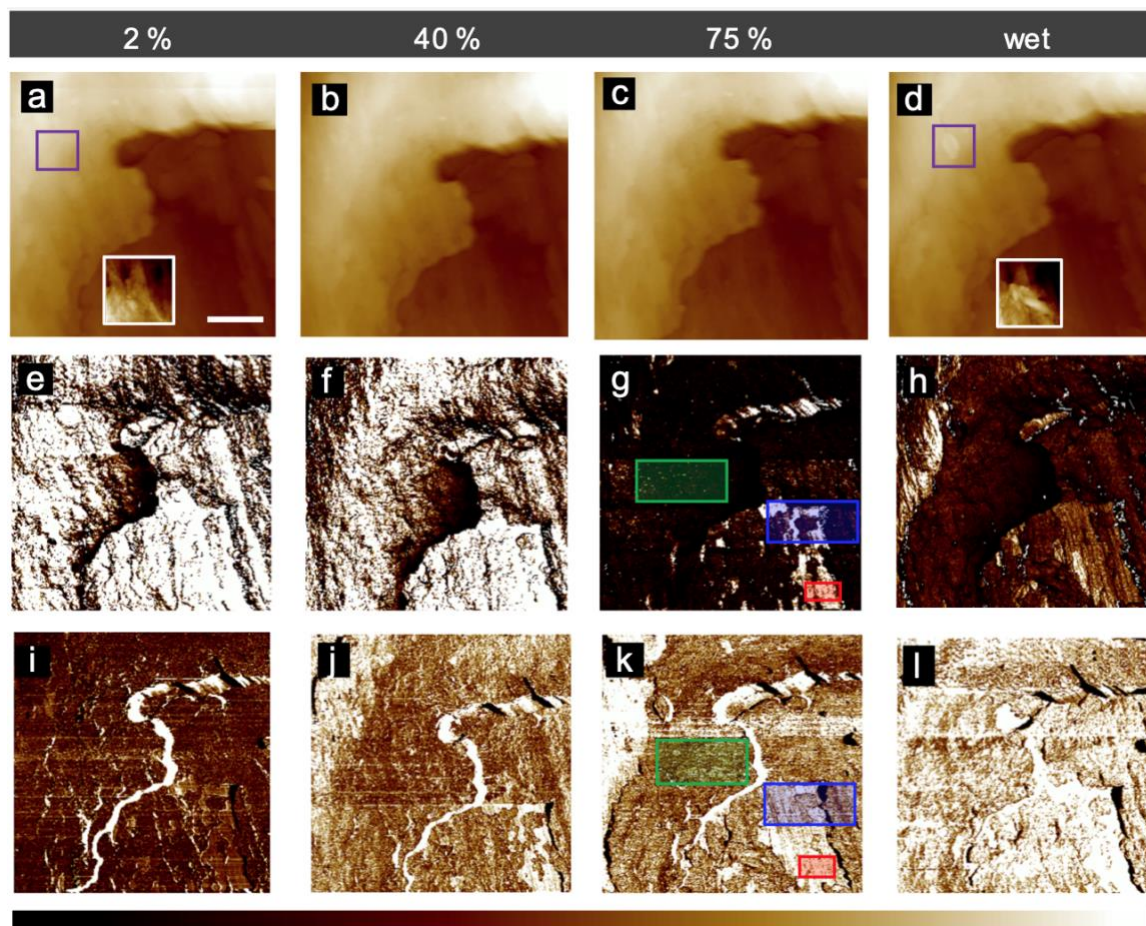


Figure 57: AFM images of LP fibres. The RH was varied from 2 % to a wet condition. (a-d) Topography images, (e-h) DMT modulus maps and (i-l) adhesion maps. The scale bar is 800 nm. The colour bar is -1 – 1.3 μm for topography images, 0 – 3 GPa for DMT modulus maps and 0 – 2 nN for adhesion maps. In the white framed topography images, the colour scale was modified to 0 – 250 nm. The white boxed images in a) and d) show the topography of the swollen microfibrils. An amorphous region of cellulose is highlighted in green, while the crystalline region is marked in red, and a transition between crystalline and amorphous regions is shown in blue.

The quasi-static PeakForce-Tapping mode allows for the simultaneous mapping of the topography and mechanical properties. Here, cumulative force versus distance curves were measured at every pixel in the recorded map. The mechanical properties were then directly

extracted from the force versus distance curves. While the adhesion force represents the minimum in the retraced curve, the DMT modulus was fitted, as shown in Figure 48b), with the prediction of the contact mechanics by Derjaguin, Muller, and Toporov (DMT) (186). In contrast to other contact mechanics models, such as the Johnson, Kendall and Roberts (JKR) model (87), the DMT model includes adhesion outside the contact area and is suitable for high elastic moduli, low adhesion and a small radius of indentation. Therefore, the DMT model was used for the contact mechanics in the measurements. As shown in Figure 57, the LP fibre exhibited crystalline and amorphous regions in the topography image, but especially in the mechanical property maps, such as the DMT modulus and adhesion, the differences in the crystal structure of cellulose were clearly distinguishable. In the mechanical property maps, the adhesion increased with increasing RH, while the DMT modulus decreased. Overall, swelling of microfibrils was observed in the AFM topography images as the RH was increased. Figure 57a) shows the topography image with the microfibrils at 2 % RH. Comparing the microfibrils in Figure 57a) to those in Figure 57d), which shows a fully hydrated fibre, the microfibrils appear to be swollen under wet conditions. The white box (Figure 57a, d) indicates in detail the swelling of microfibrils due to absorbed water inside the cellulose network. The insolubility of cellulose results in swelling of the microfibrils (16). Water infiltrates the network and diffuses through the pore space system by capillary condensation. Therefore, the volume increases, which leads to an expansion in the crystal structure and eventually breaks the hydrogen bonds in the cellulose network (13-15). Thus, variations in the RH can induce changes in the shape of a microfibril due to the not entirely connected cellulose molecules, as shown in Figure 57d), in the marked areas. Crystalline and amorphous regions showed different values for the DMT modulus, which is in agreement with Cabrera *et al.* (14). Cross sections of the DMT modulus versus the position over a crystalline and an amorphous region from Figure 57 are shown in Figure 58b) and c). The crystalline region showed a DMT modulus of 80-100 GPa, while the amorphous region exhibited a DMT modulus of 20-30 GPa. The transition from crystalline to amorphous structures, and thus the transition in the mechanical properties, seemed to be sharp and well defined according to Figure 58a).

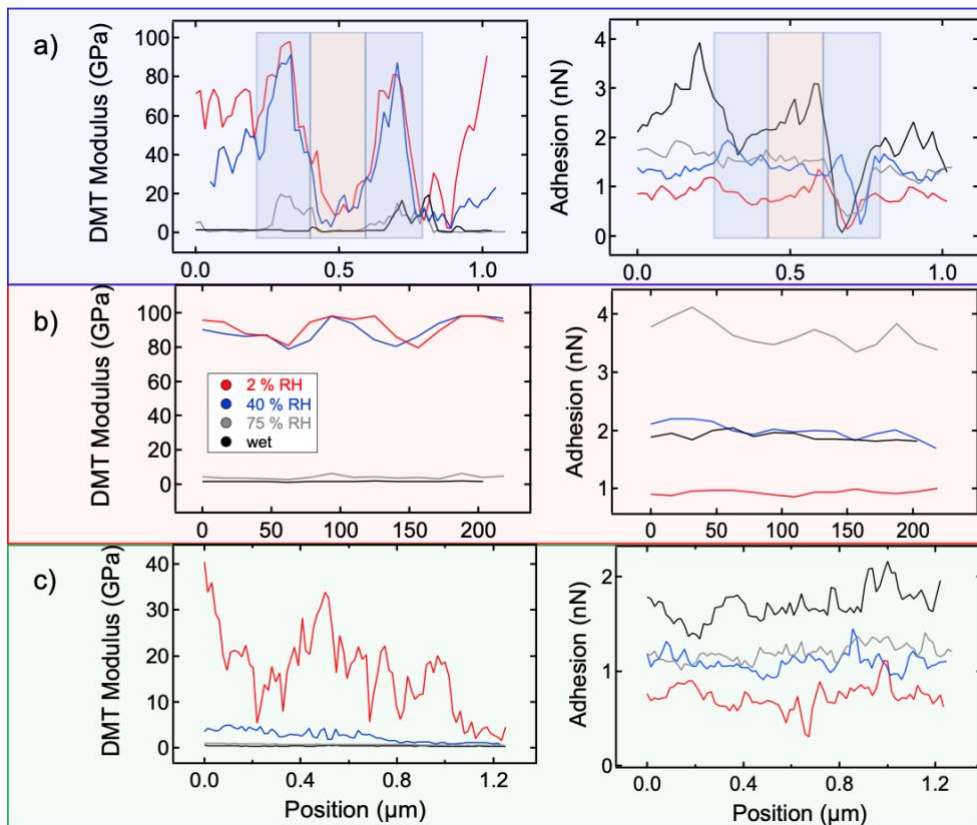


Figure 58: Cross sections corresponding to figure 8 of the DMT modulus in (a) a transition area between crystalline, amorphous and crystalline regions. The crystalline regions are highlighted in light blue, and the amorphous region is highlighted in light orange. The cross sections of the DMT modulus and adhesion of a crystalline region are represented in (b), whereas (c) illustrates this for an amorphous region.

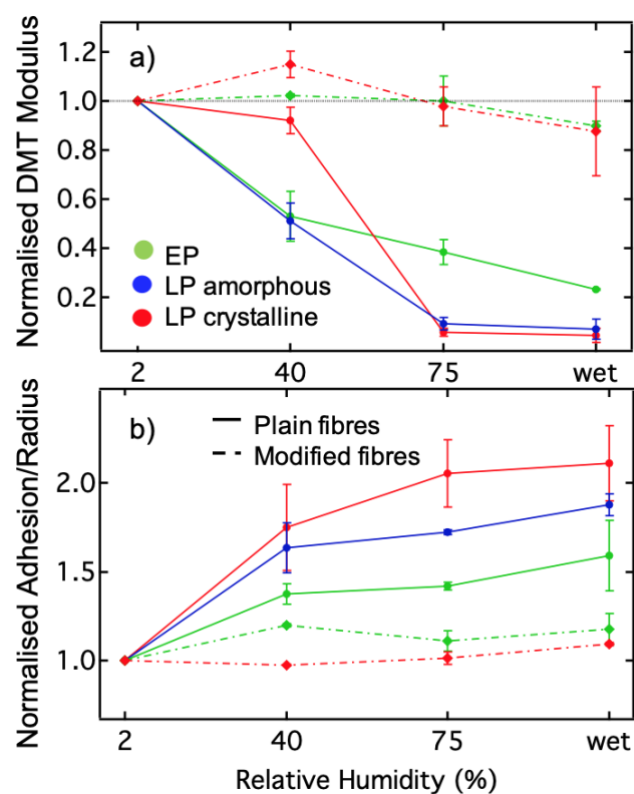


Figure 59: a) Normalised DMT modulus and b) normalised adhesion/radius plotted against the relative humidity in unmodified fibres and polymer-coated fibres.

A general decrease in the normalised DMT modulus with increasing RH was observed in crystalline and amorphous LP fibres, as well as in EP fibres (Figure 59a). Up to 40 % RH, the crystalline regions of the LP fibres did not show a significant decrease in the normalised DMT modulus, as recorded for the amorphous regions. If the RH was sufficiently high, softening of the crystalline regions was also initiated. More water molecules intrude the fibre network, diffuse to the crystalline areas and break the hydrogen bonds in these ordered areas (187). If the fibre reached a fully hydrated state, both the crystalline and amorphous regions lost their stability. A similar increase in the normalised adhesion/radius in crystalline and amorphous regions was observed, as shown in Figure 59b). When increasing the RH to wet conditions, the crystalline regions had a higher value in the normalised adhesion/radius than the amorphous regions. However, this deviation lies between the error bars and is therefore not interpreted as being distinct. With the increasing amount of water molecules inside the hydrophilic LP fibre, attractive capillary forces accumulate between the AFM tip and the LP fibre surface. Because of the softening the fibre, i.e., the decreasing DMT modulus, the tip was indented deeper into the surface, which led to the requirement of a higher reset force of the tip and therefore to a higher measured adhesion. The EP fibres consist of a more complex system than the LP fibres. While LP fibres possess a cellulose percentage of 95 %, EP fibres

also have portions of hemicellulose and lignin in their system (34, 37). Cellulose is embedded in an amorphous matrix of hemicellulose and lignin. Hemicellulose is bonded *via* hydrogen bonds to cellulose and acts as a cementing matrix. Additionally, hemicellulose is not crystalline and has a hydrophilic character. Lignin acts in EP fibres as a hydrophobic network, which increases the stiffness and is totally amorphous. Figure 59a) shows a decrease in EP fibres in the normalised DMT modulus when increasing the RH. At 40 % RH, the percentage of decrease in the normalised DMT modulus is similar to that of amorphous cellulose. Since the EP fibre mostly consists of non-crystalline parts, the fibre softens in large parts due to infusing water molecules breaking the hydrogen bonds between cellulose molecules. In contrast to simple amorphous cellulose, the EP fibres showed a linear decrease in the normalised DMT modulus when the RH was further increased to a wet condition, as indicated in Figure 59a) by the green line. This linear decrease was assumed to be caused by the lignin network. Since lignin has a hydrophobic network, the swelling of fibres and therefore the related decrease in the normalised DMT modulus was restricted. The green line in Figure 59b) shows an increase in the normalised adhesion/radius with an increasing RH for EP. Comparing these values to crystalline and amorphous cellulose, the increase is minor. It was interpreted that the more amorphous cellulose and its component parts are, the lower the increase in adhesion with increasing RH. Additionally, it was assumed that the hydrophobic lignin network reduced the attractive capillary forces between the tip and the EP fibre surface. Therefore, the adhesion increases in EP fibres were not as distinctive as those in LP fibres with amorphous and crystalline cellulose.

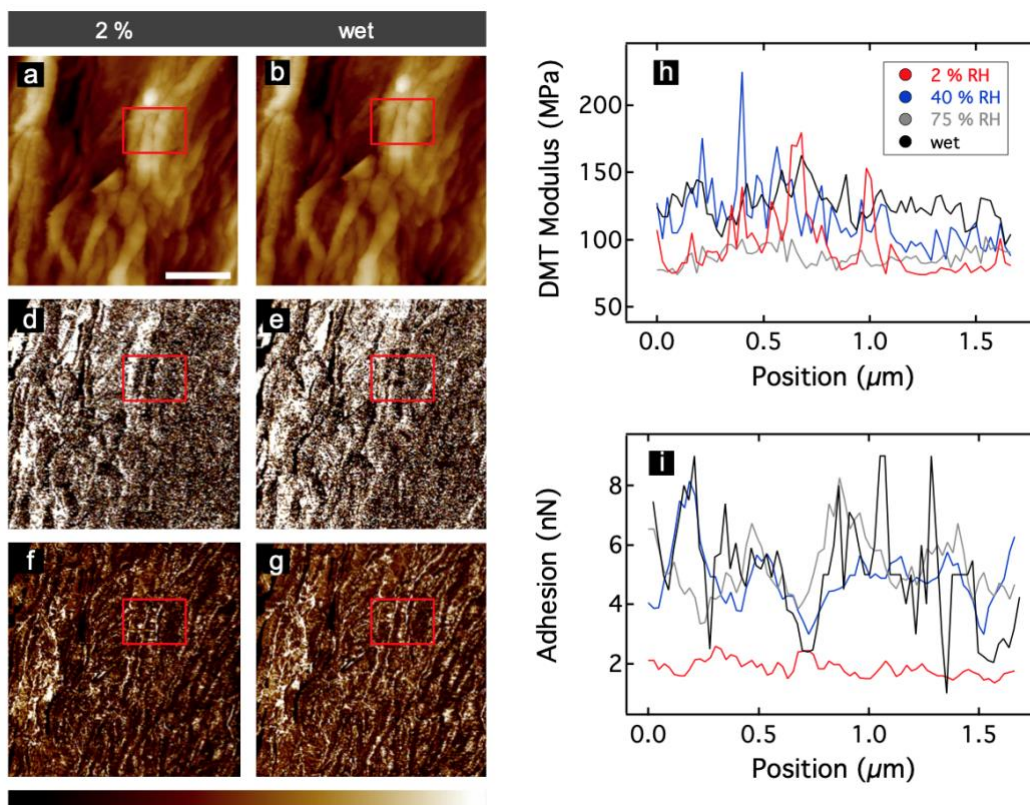


Figure 60: AFM images of a PCEP fibre with a homogeneously coated area. a) Topography image at 2 % RH with the corresponding mechanical properties of d) DMT modulus and f) adhesion. b) The topography image under wet conditions with the associated mechanical properties of e) DMT modulus and g) adhesion. The scale bar represents 2 μm . The colour scale ranges from -550 – 550 nm for topography images, from 0 – 300 MPa for DMT modulus maps and from 0 – 10 nN for adhesion maps. h) and i) The cross sections of the DMT modulus and adhesion of the PCEP fibre.

Figure 59 shows the AFM images of a PCEP fibre. As seen in figure 12a, for 2 % RH, and in Figure 59b), for the wet condition, there was no significant swelling of the microfibrils of the fibre in the topography images. This is interpreted as the first indicator of a hydrophobic polymer coating. By checking the mechanical properties such as the DMT modulus and adhesion in Figure 59d) and f) for 2 % RH and Figure 59e) and g) for the wet condition, they also revealed no significant changes when increasing the RH. Cross sections of the red framed areas in Figure 59a-g) are shown in Figure 59h) and i). These trends are pointed out in Figure 58b), where the PCEP fibres are represented by the dashed green line. Even under wet conditions, the normalised adhesion/radius in PCEP fibres is less than that in plain EP fibres. The normalised DMT modulus of the PCEP fibres in Figure 58a) with the dashed green line shows almost no change within the error and therefore differs clearly from the EP fibres. This is interpreted as a strong indicator of the hydrophobicity of the polymer coating. The PCLP

fibres are represented by dashed red lines in Figure 58. Similar to the PCEP fibres, the PCLP fibres also exhibited almost no decrease in the normalised DMT modulus and no increase in the normalised adhesion/radius with increasing RH. The changes in the normalised DMT modulus due to the hydration recorded for the polymer-coated fibres were comparable to the values measured during the indentation experiments. Thus, it is concluded that the presence of a homogenous and stable hydrophobic polymer coating can be inferred from AFM measurements. Unmodified fibres exhibit large changes in mechanical properties, such as the DMT modulus and adhesion, as well as the swelling of microfibrils in topographic images. Hydrophobic coated paper fibres show small changes in mechanical properties and almost no swelling in topographical images when the RH was increased.

5.4 Conclusion

The terpolymer P(S-co-MABP-co-PyMA) was used as a water-repellent coating on cotton linter, eucalyptus fibre bundles and individual fibres. The polymer coating could be identified in SE and fluorescence microscopy images. The CA revealed the hydrophobic character of the polymer coating at the macroscopic level. Fluorescence microscopy, however, showed an inhomogeneous distribution of the coating on the surface at the microscopic level. Raman spectroscopy revealed that the amount of water that was absorbed from a drop differed between the coated and uncoated samples. AFM experiments revealed mechanical differences between single LP or EP fibres and polymer-coated fibres in various states of hydration. On uncoated LP and EP fibres, an increased AFM indentation could be observed in the wet state, and the fibres became significantly softer. Compared with untreated fibres, fibres with a hydrophobic polymer coating showed a higher stiffness and less softening due to hydration.

The nanomechanical mapping also allowed for further insights into the local mechanics of coated and uncoated fibres. For uncoated LP fibres, crystalline and amorphous regions could be identified in the topography images, especially in the mechanical property maps. When increasing the RH, the topography images exhibited swollen microfibrils, and the microfibrils changed in size and shape. The swelling and therefore the softening of the fibre apparently started in the non-ordered regions. If both fibre types were coated with the hydrophobic polymer, no swelling of the microfibrils could be found in the topography images, and no significant changes in the mechanical properties occurred. In conclusion, Raman spectroscopy and AFM measurements revealed a softening of unmodified fibres in a humid environment due to an increased number of water molecules inside the cellulose network. The hydrophobization of the fibres with P(S-co-MABP-co-PyMA) effectively prevented swelling and mechanical weakening of the fibres. However, for the functionality of the coating, a uniform distribution of the polymer on the surface seems to be crucial.







6

Mechanical Characterisation of Plain and Polymer coated Fibre-Fibre Joints depending on the Relative Humidity

So far, the mechanical properties of single cellulosic fibres in dry, humid and wet state as well as the effect of a hydrophobic polymer coating on the mechanical properties were discussed and analysed with advanced AFM measurement techniques.

In this section, the strength of cellulosic fibre-fibre joints (FFJ) in dry and different RH states are going to be investigated. Furthermore, the wet strength of the joints is going to be increased via hydrophobic terpolymer P(DMAA-co-MABP-co-RhodBMA) diluted in H₂O and isopropanol and the changes are compared with the dry fibre-fibre joints.

The stability of paper is influenced by the amount of fibre joints, the strength and distribution as well as the contact area between the joints. Up to now, it is still not clearly identified which bonding mechanism is the dominant one to hold two fibres together. Therefore, an AFM-based method to explore the mechanical properties and the strength of the fibre joints is presented. Through static force-distance curves and a high spring constant cantilever it is possible to displace FFJs. The FFJ are not created artificially, but are pulled out of a finished cotton linter paper sheet. Additionally, the variation of the RH is included to investigate the behaviour of the joints under a humid environment. The maximum applied force on one fibre is related to the bonded area and the angle between the two fibres to identify the more important parameter for fibre joint strength. Therefore, suggestions are made which bonding mechanism could be the dominant one. Furthermore, new terpolymer coatings on the FFJs to prevent softening of the joints with increasing RH. The polymer coatings are tested on a H₂O and an IPA solution basis. The hydrophobicity of the polymers is investigated by CA measurements and the spatial distribution by fluorescence CLSM.

6.1 Introduction

The description of the mechanical properties of paper is difficult due to the high amount and the complex geometry of fibres. But the strength and stability of paper is significantly influenced by the FFJs. *Lindström et al.* predicted the most important bonding mechanisms between two fibres as mechanical interlocking, hydrogen bonds, electrostatic interactions, interdiffusion and induced dipoles (52). Furthermore, capillary bridges, micro compressions or pressure during drying are suggested as relevant bonding mechanisms (53-55). Which mechanism is how dominant is still not clearly identified. Mechanical interlocking, the entanglement of fibrils on both fibre surfaces, can lead to an increased strength and can be further increased by beating. Unbeaten fibres are often not able to form a paper sheet (53). Related to the mechanical interlocking mechanism is the size of the bonded area between two fibres. This area can also be increased by beating (53, 56, 57). The bonded area can be divided into the visible bonded area and the molecular bonded area. The molecular bonded area is the real area between two fibres and is depended on the elastic modulus of the wet fibres during the drying process, the roughness of the surface and the applied pressure during the sheet formation (55, 58). Van der Waals and hydrogen bonds are formed in the molecular bonded area, since the two fibre surfaces are brought closer than 1 nm together. The examination of the exact molecular bonded area counts as difficult, but can be accomplished via polarized light microscopy (59) or micro tomography (60). *Urstöger, Hirn et al.* as well as *Thomson et al.* used Förster Resonance Energy Transfer (FRET) to determine the degree of the molecular contact area (58, 61). The contribution of interdiffusion depends on the contact area. During sheet formation, polymer chains are moving and spreading from one fibre surface to the other fibre surface. Therefore, inter diffusion could be seen as a multiplier for the molecular bonding mechanisms as hydrogen bonds, van der Waals or coulomb interactions. Whereas in theoretical works the van der Waals interactions between the cellulose molecules are predicted to attach importance to the bonding strength (62-65), experimental works suppose hydrogen bonds have a higher relevance (67), which was predicted to be the most important bonding mechanism for a long time (68). The more carboxyl groups are present on the fibre surface, the stronger is the bonding between two fibres, as the coulomb interactions act attractive. (65) quantified the different bonding mechanisms, where they identified the energy for an individual bond of the van der Waals mechanism (6.8×10^{-24} kJ), hydrogen bonds (1.9×10^{-23} kJ) and coulomb interactions (1.2×10^{-20} kJ). An AFM-based method, which uses one opening mode only, to identify the breaking force of a fibre-fibre joint was presented by *Schmied et al.* (123, 124). They used a dynamic and a static loading to determine the elastic energy contributions and develop further insights in the dissipated energy. The breaking force was characterized to approximately 330 μ N. This

breaking force resulted also in tensile tests of (188). Both used kraft pulp at room conditions and an arrangement of an 90° angle between the fibres only. The tested breaking forces of latewood and earlywood fibres are 10-15 times higher (70, 189). Most of the authors used the suggested preparation method of *Stratton and Colson*, where the fibre-fibre joint is artificially created and are not pulled out of a finished paper sheet (70).

The influence of humid air or water on the mechanical properties of natural fibres is an important topic to be addressed in the application of cellulose-based materials. The impact of relative humidity on the elastic modulus, stiffness, or strength has been investigated by various authors (109-111).

Since cellulose and the associated produced paper products drastically reduce their strength and mechanical properties through the influence of solvents, wet strength agents are used to increase wet strength. This enables the use of paper products in new areas of application. Polyamidoarminepichlorohydrin resin (PAAE resin) is one of the most commonly used wet strength agents in this mechanism (19, 20), where the associated increase in strength can be seen in both dry and wet conditions. In addition to all the advantages of increasing strength in dry and wet conditions, PAAE resins in particular have some disadvantages. Such as: reusability is greatly reduced (17), by-products (such as organic halogen compounds) could cause severe environmental pollution (21) or high energy input during fabrication (41). The use of resins also restricts the possible applications.

Thus, new terpolymers can be introduced to enhance the wet-strength of cellulose based papers or fibres. The integration of fluorescence copolymers parts enables the investigation via fluorescence confocal laser scanning microscopy. For example, the distribution of coatings on fibres and the distribution in the fibre network can then be investigated (4, 11).

In the following, a static AFM-based method to detect the strength and flexibility of cellulose based FFJs depending on the RH is reported. First, the strength of plain FFJs with increasing RH is investigated. Then, the maximum applied force is related to the bonding area and the bonding angle between the fibres. Then FFJs which were coated with the hydrophobic terpolymer P(DMAA-co-MABP-co-RhodBMA) diluted in distilled H₂O and isopropanol (IPA) to check the increase of the wet-strength.

6.2 Materials and Methods

6.2.1 Materials

The cellulosic FFJs were manually extracted from a linter paper sheet which is prepared according to DIN 54358 and ISO 5269/2 (Rapid-Köthen process). The paper sheet was coloured beforehand with a 100 μmol calcofluor solution for the confocal fluorescence microscopy measurements. The extracted FFJ was mounted on a 3D printed sample holder, which supplied a fixed trench distance L of 1 mm between the two attachment points. Therefore, the FFJ was freely suspended to the relative humidity environment to exclude influences of a substrate or other connecting fibre bonds. The setup is schematically shown in Figure 61.

The used polymer P(DMAA-co-MABP-co-RhodBMA) was diluted in distilled H_2O and IPA (30 mg/mL). The polymer solution was sprayed onto to mounted FFJ. Then the FFJ was illuminated with UV light (365 nm) (UV light source: Carl Roth, Karlsruhe, Germany) for 17 minutes to bind the polymer coating to the fibres. After that the FFJ was dried for 24 hours according to (22, 48, 190). The polymer coated fibres are called PFFJ in the following.

The FFJ and PFFJ were placed in climate chamber. The RH was set at 2 %, 40 %, 75 %, and 90 %. The fibre was exposed to the RH for 45 minutes before measuring.

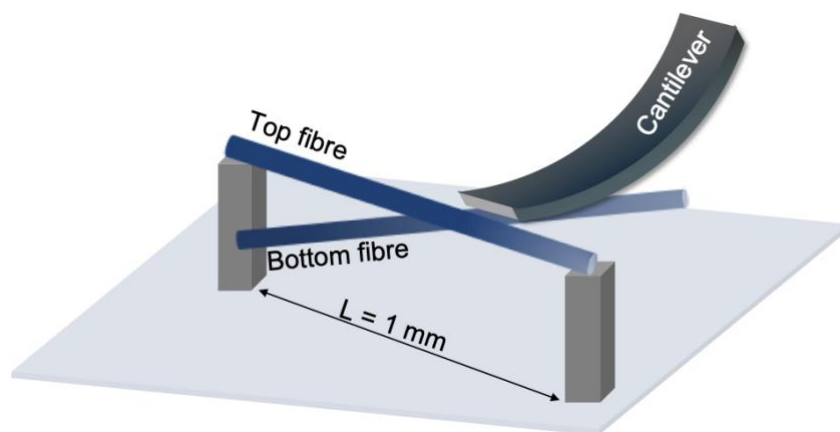


Figure 61: Schematic setup of the FFJ and the position of the cantilever. The cantilever is positioned on the bottom fibre, which is connected to the top fibre. The top fibre is attached to the sample holder.

6.2.2 Methods

6.2.2.1 Contact Angle Goniometry

For the contact angle goniometry (CA) measurements, a CA goniometer (OCA, DataPhysics Instruments, Filderstadt, Germany) was used. A static Milli-Q water droplet with a volume of 2 μl was placed on the sample. The CA was determined *via* Young-Laplace alignment 1 s after drop generation. For each polymer 30 measurements were executed.

6.2.2.2 Confocal fluorescence microscopy

The polymer-modified FFJs were analysed using fluorescence CLSM to study the spatial distribution of the copolymer/cellulose fibre network. Since cellulose exhibits intrinsic fluorescence across nearly the whole visible spectrum, plain FFJs were stained with Calcofluor White (CW) to improve the cellulose fibres visibility and allow its distinction from the rhodamine-labelled copolymer under fluorescence microscopy, this approach was prepared as described (2, 18, 73). A Leica TCS SP5II Confocal Laser Scanning Microscope (CLSM, Leica Microsystems GmbH, Germany) was used and sequentially excited each pixel line of the confocal scan with 561 nm and 405 nm lasers, corresponding to the excitation wavelengths of Rhodamine and Calcofluor White, respectively. The emission was subsequently detected between 575 nm and 630 nm for Rhodamine-labelled copolymer and 420 nm and 470 nm for CW. For each FFJ, images stacks of ~ 50 slices with widths of 0.6 to 1 μm were obtained and processed within the *Imaris Viewer software* to provide 3D images.

6.2.2.3 Atomic force microscopy

A Dimension ICON (Bruker, Santa Barbara, USA) was used for accomplishing static force-distance curves on the FFJ. A tipless cantilever with a spring constant of 800 N/m was employed. The cantilever was positioned on the bottom fibre close to the FFJ. The feedback was shut off. The maximum z-length of the piezo with 12.67 μm was pre set. Therefore, the maximum applied forces in every measurement according to Hook's law could be 10.136 mN. The recorded force-distance curves were background corrected. A Matlab (The MathWorks, Inc. Natick, Massachusetts, USA) code was used to detect the resulted maximum applied force in every measurement. The resulted maximum applied force was related to the bonded area and the angle between the two fibres. Both values are displayed in Figure 62a). All experiments were done in a climate chamber at the AFM. Hence, it was possible to vary the relative humidity (RH) during the experiments. The chosen RH were 2 %, 40 %, 75 % and 90 %. As the RH was adjusted, all the FFJ were suspended 45 minutes to the environment before

starting the measurements as done in literature (113, 191). After every 10th loading cycle the cantilever was completely retracted. This was done to investigate the recovering properties of the FFJ after loading. This is schematically shown in Figure 62b).

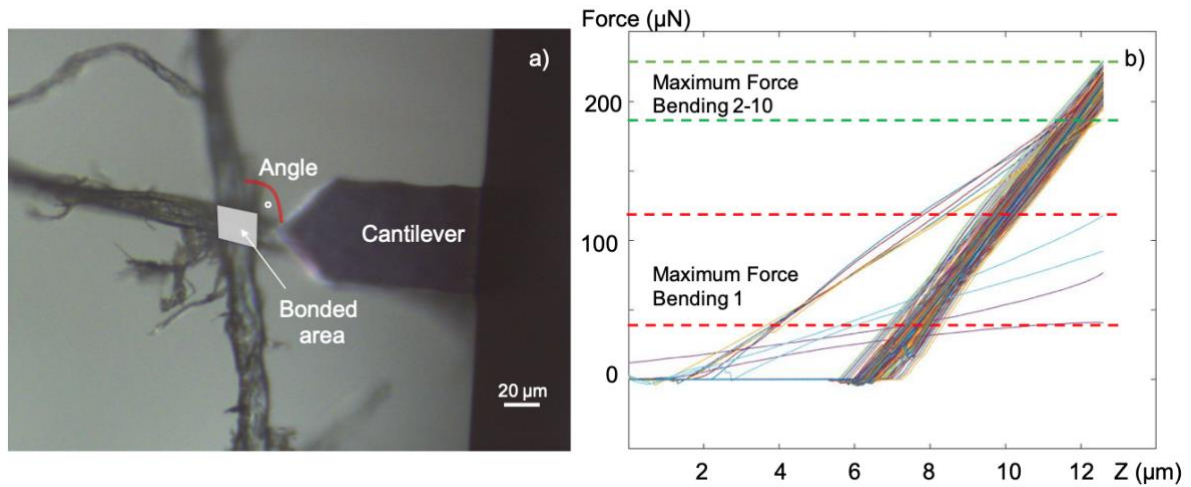


Figure 62: a) Optical image of a FFJ. The bonded area is marked in white and the angle between the fibres is marked in red. The cantilever is positioned next to the fibre-fibre crossing. b) Schematic force-bending displacement curve. The maximum force is the first bending is schematically marked for two cycles in the dashed red lines. Also, the maximum force for the 2nd -10th bending cycles is schematically marked for two cycles in the dashed green lines.

6.3 Results and discussion

6.3.1 Hydrophobicity and spatial distribution of the terpolymer P(DMAA-co-MABP-co-RhodBMA)

With the help of static CA measurements, the hydrophobic character of the polymer coating could be investigated. The images of sessile droplets (2 μl of deionised water) of the H₂O-based polymer and IPA-based polymer on a cotton linter sheet are shown in Figure 63.

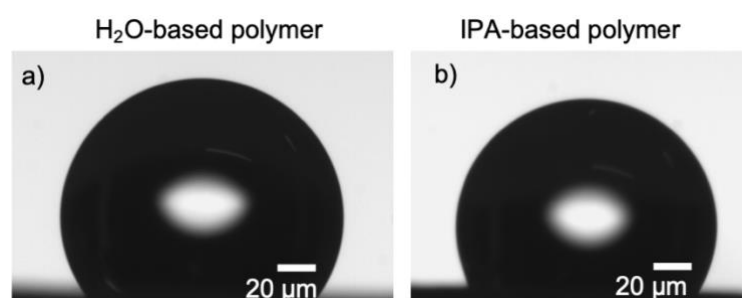


Figure 63: Images of 2 μL sessile drops of a) H₂O-based polymer and of b) IPA-based polymer on a cotton linter sheet.

The contact angle of the H₂O-based polymer exhibited a value of $134^\circ \pm 13^\circ$. The contact angle of the IPA-based polymer was $123^\circ \pm 9^\circ$. Thus, both polymer coatings showed on a coated cotton linter sheet a hydrophobic behaviour.

In the fluorescence CLSM measurements the homogeneous distribution of both polymer coatings was secured. A CLSM image is shown in Figure 64. The cellulose components are displayed in cyan and the polymer distribution in purple.

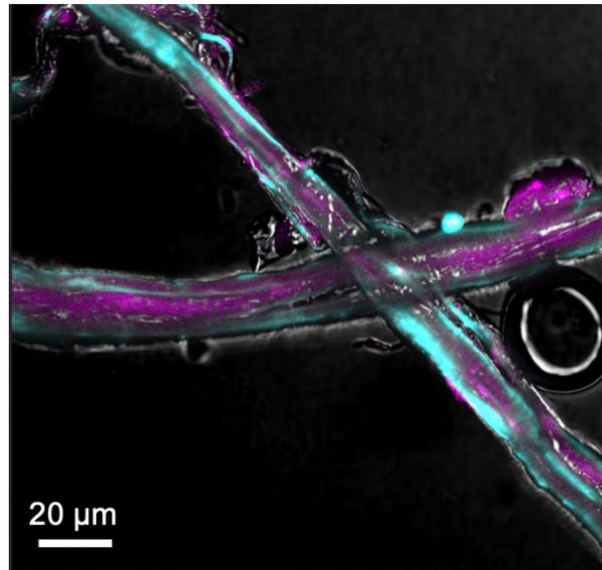


Figure 64: CLSM image of fibre-fibre joint modified with the polymer coating. The cellulose components are displayed in cyan and the polymer distribution in purple.

Note: All investigated FFJs had a uniform distribution of the terpolymer. This was ensured by the CLSM measurements.

Thus, the discussed polymer coatings should exhibit a hydrophobic behaviour in all parts of the PFFJs.

6.3.2 Stability of plain fibre-fibre joints depending on the RH

In Figure 65a) the maximum force value in μN are plotted over 50 bending cycles for the plain FFJ. The blue line represents 2% RH, the red line 40 % RH, the green line 75 % and the black line 90 % RH. A clearly subdivision of the different colours, RHs respectively, is visible. The highest maximum applied force exhibited the FFJ at 2 % RH, followed by 40 %, 75% and 90 % RH. This observation seems reasonable since paper fibres/FFJ become loose with increasing RH. The intruding water molecules with increasing RH break the hydrogen bonds and let slip the cellulose polymer chains along each other and therefore, the bond loose stability. Another observable thing is that the highest maximum force is at 2% RH at 310 μN in average. At 40 % RH it is 80 μN , respectively. But with the used AFM set up it was possible to apply approximately 10 mN ($k=800 \text{ N/m}$, $z= 12.67 \mu\text{m}$, see Equation (1)). From this fact it can be suggested that the FFJ are very flexible. The z-movement of the piezo of 12.76 μm was proceeded and reached in every measurement. The FFJ are not static bonds, but twist when a force is applied on one of the fibres, also observed by *Schmied et al.* (124). The breaking force of approximately 330 μN could be applied via our set up, but could not be reached because of the flexibility and the twisting of the fibres (123, 124, 188). A reason for that represents the fact, that in these measurements no artificially created FFJ were used, as usually in literature described by *Stratton and Colson* (70). The FFJ were pulled out of a finished processed linter paper sheet. Therefore, it is suggested that the papermaking process including beating or pressing strengthens the FFJ compared to creating the FFJ artificially or to extracting FFJ from a pulp. Hence, it was not possible to break the bonds properly. But in that way, it was possible to repeat the bending measurements for 50 cycles and thus, explore the bonding mechanisms further.

By applying 50 bending cycles to the fibre, a decay of the maximum force values after every 10th cycle was observable. This is a result of the measurement technique, as shown in Figure 65b). Firstly, the cantilever is approached towards the bottom fibre, then the bottom fibre is bend 10 times and then the cantilever is withdrawn. After that, the cantilever is again approached to the bottom fibre. In every first approach/first pressing of the fibre, the maximum applied force resulted lower in force than the rest of the 10 cycles. When withdrawing the cantilever, the bottom fibre of the FFJ could recover and could turn up to its original position. Hence, this technique could be used to explore the fatigue of the FFJ.

As seen Figure 65a) the maximum force is returning to the same maximum force as in the previous cycles after the first bending. The z-piezo was moved 12.67 μm in every measurement. But the FFJ were not separated by this distance as discussed before due to bending and twisting of the bottom fibre. But the tilting of the bottom fibre, which was still

attached to the top fibres, was a longer distance than the operation regime of short-range forces (van der Waals forces, hydrogen bonds, electrostatic interactions, induced dipoles or capillary bridges). Therefore, it can be deduced that the FFJ are dominantly held together not by short-range forces. As the maximum force could return after every withdraw and approach, it can be assumed that the FFJ could recover, too. In the recovering process during withdrawing and approaching the cantilever, it cannot be excluded that e.g. new electrostatic interactions between the separating fibrils of the two fibres occur due to the movement. However, overall, the mechanical interlocking of the fibrils or the interdiffusion process seem to play the most important role in a FFJ. They have a long operation distance and are therefore predicted to be dominant in the bonding mechanisms. Also, *Schmied et al.* attributed 55 % of the bond's energy to the mechanical interlocking (69).

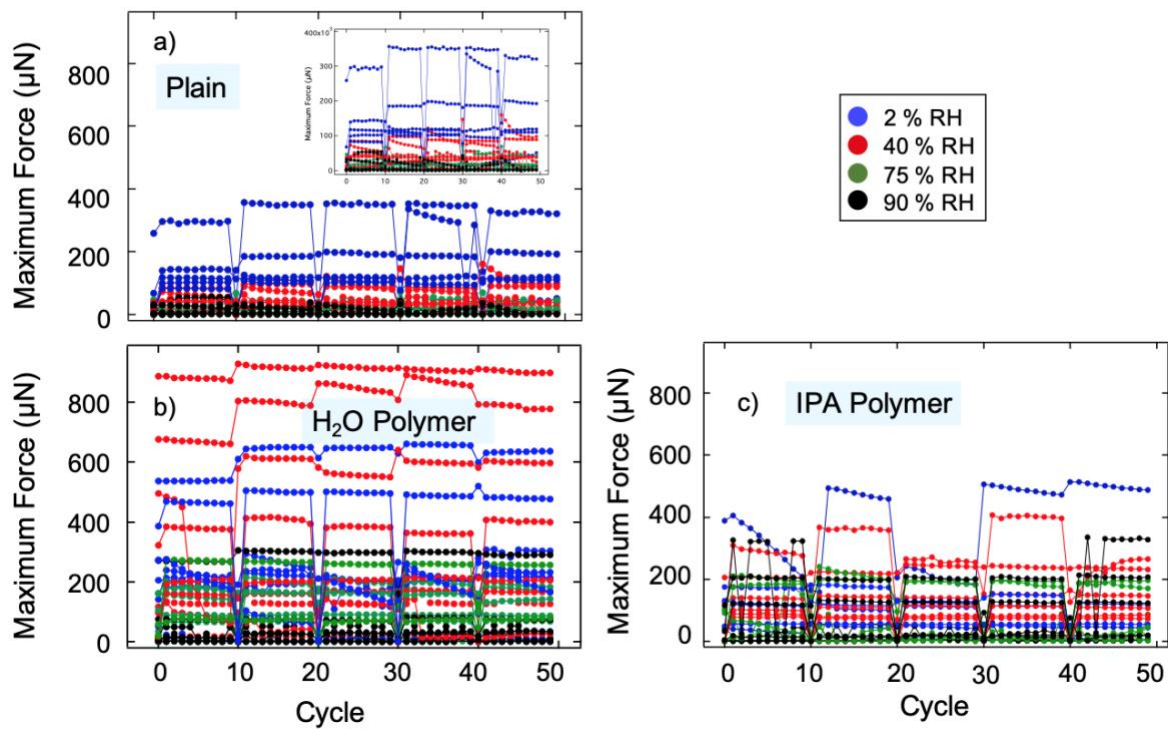


Figure 65: Maximum Force in μN over Cycles of the different FFJ. The blue points represent the force values at 2 % RH, the red points at 40 % RH, the green points at 75 % RH and the black points at 90% RH. a) Plain FFJ, b) H₂O based polymer coating and c) IPA based polymer coating.

6.3.3 Relation of maximum force to bonding area and bonding angle

After discussing the maximum applied force over 50 cycles, the maximum force is related to the bonded area and the bonding angle between the two fibres. It was shown that the maximum force returned to the maximum force valued before withdrawing and approaching the cantilever. Thus, the average value of the maximum force could be calculated without a high standard deviation. The results of the average maximum force values in μN plotted over the bonded area in μm^2 and the bonding angle in $^\circ$ are shown in Figure 67a) and b). The visible subdivision of the force values at the different RHs as seen in Figure 66 a) over cycle is also noticeable in Figure 67. To get a better observable relationship between the maximum force, angle and bonded area, the drawn surfaces are related to the force values. This is shown in Figure 67c)-f).

It can be seen that at 2% RH (blue surface) there is no obvious relationship between force, angle and bonded area. All maximum force values do not depend strongly on angle or bonded area either. The red surface displays 40 % RH. Here, a relationship of force and angle is visible. An increase in force is observable at 90 $^\circ$. FFJ with the identical bonded area, but different bonding angles exhibited different maximum forces. The close ups for 75 % and 90 % RH are shown in Figure 67g) and h). Here, the same relationship is noticeable. Close to 90 $^\circ$ the maximum force increases. Thus, it can be suggested that at 2 % RH the FFJ strength does not depend strongly on area or angle because of the non-humid environment. At 40 %, 75 % and 90 % RH a relationship dependency from force to bonding angle is visible. Therefore, it is suggested that the bonding angle between two fibres is more relevant for a high FFJ strength.

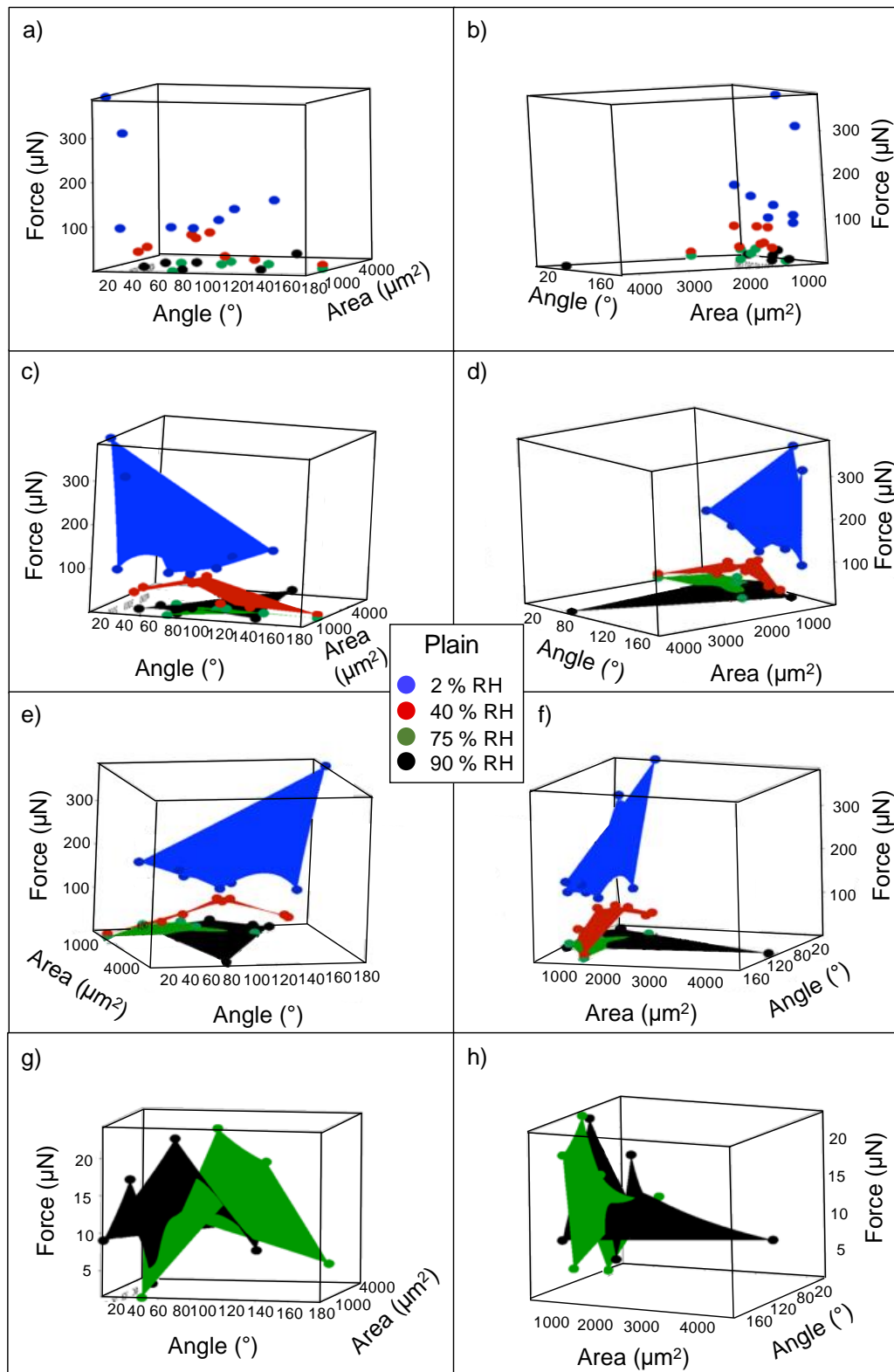


Figure 67: a) and b) 3D plots of the average force values of the plain FFJ over the angle and bonded area. The blue points represent the force values at 2 % RH, the red points at 40 % RH, the green points at 75 % RH and the black points at 90% RH. c-f) 3D Surface plots of the average force values of the plain FFJ over the angle and bonded area. g) and h) displays the close ups of 75 % and 90 % RH.

6.3.4 Stability of polymer coated fibre-fibre joints depending on the RH

To prevent the softening of the FFJ when increasing the, the polymer P(DMAA-co-MABP-co-RhodBMA) diluted in H₂O and IPA was sprayed onto FFJ. The maximum applied force over the 50 bending cycles for the polymer diluted in H₂O is shown in Figure 68b). In this plot there is no clear subdivision of the force values from the different RHs visible. This is a first indication that the hydrophobic polymer coating could be effective in protecting the FFJ against softening when the RH is increased. Another noticeable fact is that in most of the bending series over the 50 cycles did not have a decay in the maximum force value when withdrawing and approaching every 10th cycle the cantilever. This is a further indication that the polymer coating is effective and strengthens the FFJ, even in dry state. With the polymer coating the bottom fibre is not able to separate as much as without a coating from the fixed top fibre. Therefore, the bond did not have to recover from the bended status. The bending series with a distinctive decay is attributed to a not homogenous or incomplete polymer coating. This circumstance will be discussed later on.

Furthermore, it is noticeable that the maximum applied force values with the H₂O-based and IPA-based polymer coating are higher than without a coating. Thus, it is suggested that the polymer coating strengthens the FFJ bonds and therefore, the twisting of the fibres is reduced which leads to a higher applicable force on the bottom fibre. This fact strengthens the assumption of the effectiveness of the polymer coatings. As discussed before, the average of the maximum applied forces is calculated. The maximum force values are plotted against area and angle in Figure 69. From the first sight there is no observable relationship between the force and angle or area. This fact also speaks for a strengthening of the FFJ due to the polymer coating.

6.3.4.1 Mechanical stability differences between H₂O- and IPA-based polymers

Now, the effects with the H₂O- and IPA-based polymer coating on the FFJs is discussed. The maximum force is plotted over the 50 bending cycles is shown in Figure 65b) and c). In both figures there is not clear subdivision between the maximum forces of the different RHs. Thus, this fact is interpreted that the polymer coating strengthens the FFJ. Additionally, an identical circumstance to the polymer diluted in H₂O is that most of the bending series do not own a decay in maximum force after with the withdrawing and approaching the cantilever every 10th cycle in opposite to the IPA-based PFFJs. Compared to the maximum forces of the H₂O based polymer the maximum force values of the IPA based polymer coating appear to be lower. This is interpreted to be the first evidence that the polymer diluted in H₂O could be more effective in strengthening the FFJ in dry and humid environments. The average

maximum force values are plotted over the bonded area and angle. This can be seen in Figure 69.

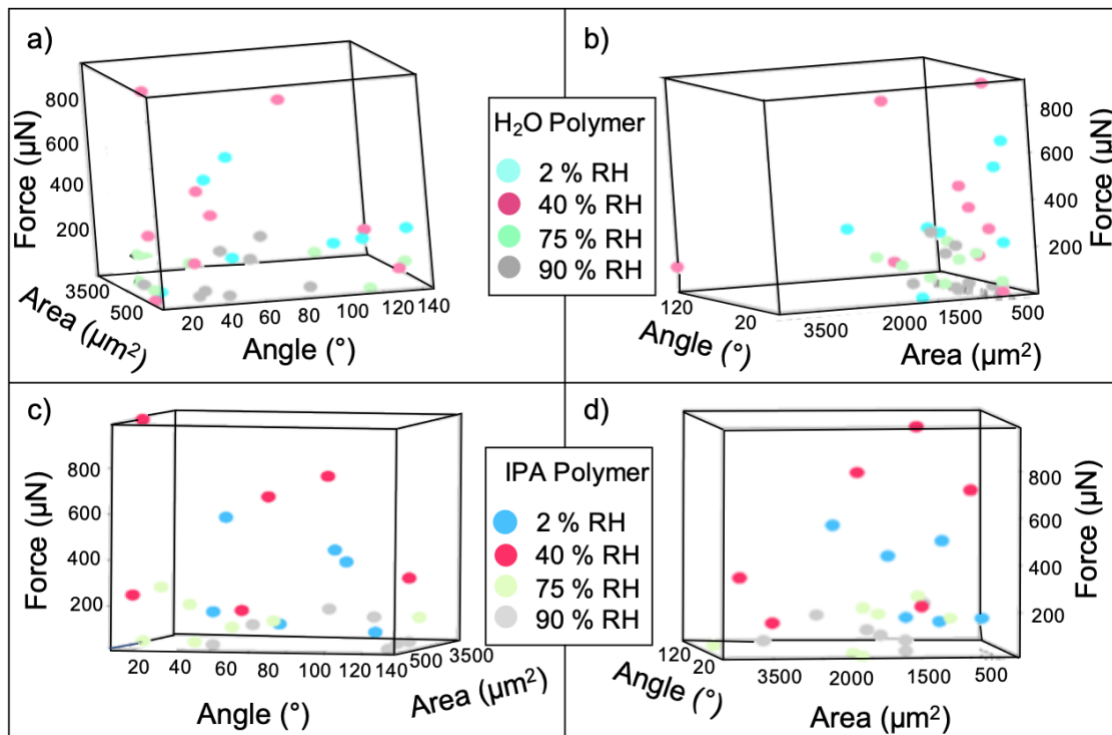


Figure 69: 3D plots of the average force values of the H₂O based und IPA based polymer coated FFJ over the angle and bonded area. H₂O polymer: The turquoise points represent the force values at 2 % RH, the pink points at 40 % RH, the light green points at 75 % RH and the grey points at 90% RH. IPA polymer: The light blue points represent the force values at 2 % RH, the magenta points at 40 % RH, the light green points at 75 % RH and the light grey points at 90% RH.

6.3.5 Comparison of stability of plain and polymer coated fibre-fibre joints

To compare the maximum force values of the plain FFJ with the polymer coated FFJ as well as establishing a relationship between the maximum force and the bonding angle or bonded area, the values are plotted separately as shown in Figure 70. Figure 70a) displays 2 % RH, b) 40 % RH, c) 75 % RH and d) 90 % RH. In Figure 70a) the dark blue points represent the values of plain FFJ, the turquoise points the values of the H₂O diluted polymer and the light blue points the values of the IPA diluted polymer FFJ. When interpreting the data points and relating the force to angle and area, there is no obvious relationship visible. This applies to all data points. Additionally, almost all data points are in average with the force value of 200-300 μ N. Also spikes of higher force values are observable. These values can be assumed to have a higher polymer coating concentration on the FFJ. Therefore, it is suggested that the 2 % RH plain FFJ as stable as the polymer coated FFJ due to the dry environment of the measurements. In Figure 70b) the values of the 40 % RH measurements are shown. The red points show the plain FFJ, the pink points the H₂O based polymer FFJ and the magenta points the IPA based polymer FFJ. Here, a clear subdivision between the polymer coated FFJ and the plain FFJ in force values is visible. The force values of the plain FFJ lied below the force values of the polymer coated FFJ. Additionally, there are some remarkable points with higher force values than the obvious average. This is attributed to a higher polymer concentration on the FFJ than the other FFJ. Furthermore, a few force values appear to be lower than the overage, which can be explained by an inhomogeneous polymer coating as addressed in Figure 70 with the decay of the maximum force values over the 50 cycles. Thus, it is interpreted that at 40 % RH the polymer coating based on H₂O and IPA are both effective against intruding water molecules and hence, softening of the FFJ. In Figure 70c) the values at 75 % RH are shown. The plain force values are displayed in dark green, the H₂O based polymer values in light green and the IPA based polymer values in turquoise. Again, a subdivision between the plain FFJ force values and the polymer coated FFJ force values can be seen. The plain FFJ force values appeared to be lower than the polymer coated ones. The polymer coated force values lied within 150-200 μ N. Hence, it is deduced that the polymer coating is also effective for protection of the FFJ against softening due to RH. Additionally, it is suggested from Figure 70c) that the polymer coating based on H₂O is more effective than the IPA based polymer coating at 75 % RH, since the force values appeared to be higher. This is in good agreement with *Schäfer et al.* (190). As the polymer solution with H₂O had the ability to swell the cellulose fibres, the copolymer could reinforce the fibres. As IPA does not swell the fibres, the copolymer could not penetrate into the fibres. Thus, the wet strength occurred to be lower here. Figure 70d) exhibits the force values related to angle and area at 90 % RH. The dark grey points display the plain FFJ, the grey points the H₂O based polymer coated FFJ and the

light grey points the IPA based polymer coated FFJ. As seen at 40 % and 75 % RH before, at 90 % RH a subdivision between the force values of the plain FFJ and the polymer coated FFJ is observable. But as indicated at 75 % RH the H₂O based polymer coating seemed to exhibited higher applicable force values than the IPA polymer coated FFJ. Over all, both polymer coatings appeared to be effective in the prevention of softening the FFJ due to increasing relative RH. The applicable forces with the polymer coating lied between 100-200 μ N. A few data points exhibited higher or lower force values, which was attributed to a higher or inhomogeneous polymer concentration on the FFJ. At gaps or vacancies in the coating the water molecules from the humid environment are able to intrude the FFJ. This could lead to breaking up hydrogen bonds and therefore, softening of the FFJ strength.

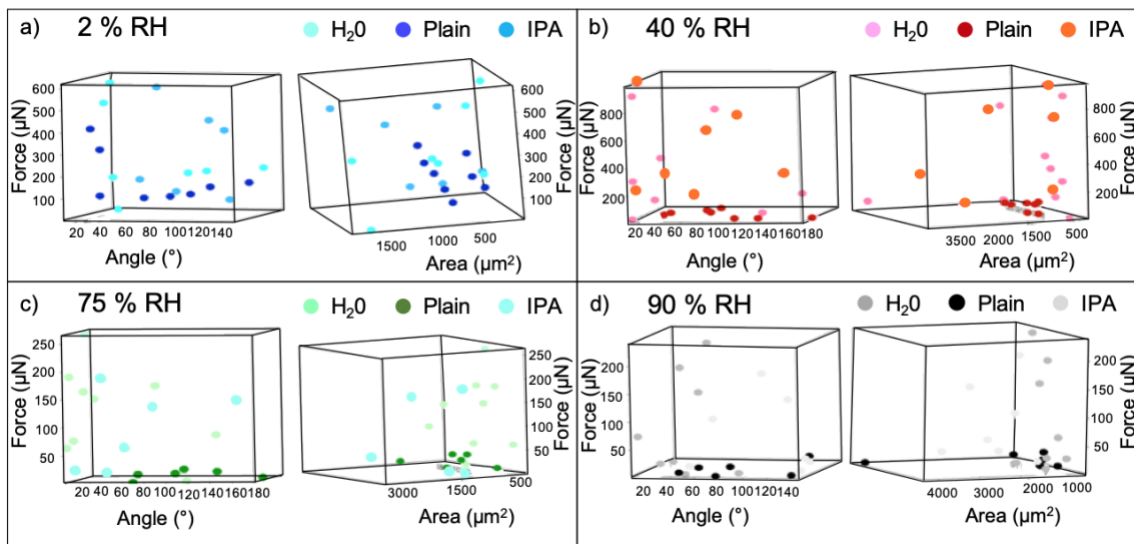


Figure 70: 3D plots of the average force values of the plain, H₂O based und IPA based polymer coated FFJ over the angle and bonded area. a) at 2 % RH, b) at 40 % RH, c) 75 % RH and d) 90 % RH.

6.4 Conclusion

The terpolymer P(DMAA-co-MABP-co-RhodBMA) was used to investigate via a static AFM-based method the improvement of the wet strength fibre-fibre joints. The plain and polymer coated FFJs were exposed to RH (2 % RH, 40 % RH, 75 % RH and 90 % RH) and the influence of the RH on the fibre joint stability was detected. The terpolymer was diluted in H₂O and IPA to observe potential differences in wet strength with both solutions. The spatial distribution of the polymer on the FFJs was ensured with investigation of the FFJ with CLSM. The maximum applied force on the FFJs were related to the visible bonding area and angle of both fibres.

At first, it could be observed that the strength of plain FFJs decreased with increasing RH. Additionally, the 3D plots of maximum applied force to the exhibited that the highest stability of the FFJ is reached close to a bonding angle of 90°. The visible bonding area played not such an important role. Also, it could be interpreted that the most important bonding mechanism between two fibres is the mechanical interlocking mechanism.

Compared to H₂O and IPA polymer coated FFJs, the plain FFJs exhibited a lower maximum applied force. The highest maximum applied force could be reached in H₂O polymer coated FFJs. Here, additionally, a segmentation of the maximum forces into the RHs were not observable. This also applied to the IPA polymer coated FFJs. Thus, the polymer coating had a positive effect on the wet strength of FFJs.

Furthermore, it was found that the polymer coated FFJs had no strong relationship between the maximum applied force and the bonding angle or area.

Both polymers (H₂O and IPA based) seemed to be effective in improving the wet strength of FFJs. The more effective one was the H₂O based polymer.

For future work it would be interesting to take the CLSM stack-measurements and use them for finite element method analysis. The AFM results on the strength of FFJs can be then used for reference to refine a finite element model on simulation a whole paper sheet.



7 Summary

In this thesis, a variety of novel scanning atomic force microscopy-based methods have been developed and demonstrated on single cellulosic fibres and on fibre-fibre joints.

First of all, a set up for an improved standard bending test, the scanning bending test, was developed. The scanning bending test method was performed at free hanging cotton linter fibres, which were clamped at both ends. *Via* colloidal probe atomic force microscopy measurements, the fibre was bent in sections along the longitudinal direction of the fibre. These measurements were analysed in combination with confocal laser scanning microscopy and scanning electron microscopy measurements. This combination allowed insights into the relative humidity depended swelling, bending ability, contact stress, and stress-strain curves of the fibre sections. Thus, it was possible to create a detailed mechanical image of a single paper fibre. The method introduces the analysis of multiple virtual set-points to allow a detection of a nonlinear local response of the fibre. The measurements to show the repeatability of this technique (two cycles of changing the relative humidity) of this method supported the results of an increased bending ability, the development of “soft spots” within the fibre, the increase in adhesion and dissipation with increasing relative humidity. It was also shown that the point-wise coefficient for adhesion and dissipation along the fibre could differ between the first and second cycle of the relative humidity change. However, as a cotton linter fibre is a natural occurring and processed material, it cannot be expected to obtain a highly reproduceable measurement.

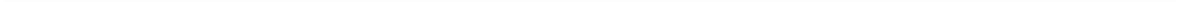
An atomic force microscopy-based method was introduced to assess the intrinsic mechanical properties of cellulosic fibres. The method includes the recording of static force distance curves and analysed them in a stepwise manner. As processed cotton linter and unprocessed cotton fibres were investigated it was possible to find out how the pulp treatment affects the mechanical properties near the surface of the fibres. It was shown that dry fibres possessed a stiffer outer layer with softer layers beneath. The unprocessed cotton fibre exhibited an even stiffer layer on the fibre surface. This shows that the pulp treatment process could lead to the removal of the C, P and S1 layer of the fibre. The results of the AFM measurements were combined with fluorescence confocal laser scanning microscopy. Here, carbohydrate-binding proteins were used to label pectin, semi-crystalline cellulose and crystalline cellulose, which are present in the different wall layers to verify the correlation between the wall layers and the measured elastic modulus in z-direction. Also, the mechanical properties of the fibres in wet state was investigated. It could be interpreted that the wax-containing layers such as C

and P can be assumed to be natural protection against intruding water molecules. Two different cantilever geometries (high aspect ratio tip and high spring constant) were used to probe the subsurface mechanical properties. It could be shown that the high spring constant cantilever provides more reliable data, as the Hertzian contact model fits were more accurate. Moreover, the influence of a water-repellent coating (terpolymer P(S-co-MABP-co-PyMA) on the mechanical properties on single cotton linter and eucalyptus fibres and small fibre bundles was investigated. The terpolymer should prevent the fibres/fibre bundles of the softening with increasing relative humidity and therefore the loss of the mechanical stability. The analysis of the nanomechanical properties was done *via* nanoindentation and nanomechanical mapping. The macroscopic analysis of the polymer properties was performed *via* scanning electron microscopy and fluorescence microscopy (revealed an inhomogeneous distribution of the polymer on the surfaces) and contact angle goniometry measurements (showed the hydrophobic character of the polymer coating). *Via* Raman spectroscopy the penetration of water into the fibres could be analysed. The amount of water that penetrated into the plain fibres was higher than the amount that penetrated into the coated fibres. The mechanical analysis via nanoindentation showed that the uncoated fibres became significantly softer than the coated fibres when increasing the relative humidity. In the nanomechanical mapping allowed insights into the softening procedure of crystalline and amorphous regions on single fibres. The softening started in the non-ordered regions. A difference between the decay of mechanical properties when increasing the relative humidity between both fibre types was detected based on the different composition of both fibre types. When coating both fibre types with the terpolymer a weak decrease in the mechanical properties could be shown.

Finally, the stability of plain and polymer coated (P(DMAA-co-MABP-co-RhodBMA)) fibre-fibre joints under the influence of relative humidity was investigated. It could be observed that the strength of plain fibre-fibre joints decreased with increasing relative humidity. In the 3D plots of the maximum applied force related to the bonding angle and bonding area, it became obvious that the highest stability of the fibre-fibre joints is reached close to a bonding angle of 90°. The visible bonding area seemed to play an important role. Also, it could be interpreted that the most important bonding mechanism between two fibres is the mechanical interlocking mechanism. The polymer coated (H₂O and isopropanol based) fibre-fibre joints both exhibited a higher dry and wet strength than the fibre-fibre joints. The highest maximum applied force was measured at the H₂O polymer coated fibre-fibre joints. Here, additionally, a dependency of the maximum forces depending on the relative humidity was not observable. This also applied to the isopropanol polymer coated fibre-fibre joints.

Thus, the polymer coating had a positive effect on the dry and wet strength of fibre-fibre joints.





8 Supplementary

8.1 Supplementary Information to chapter 3

8.1.1 Supplementary Figures

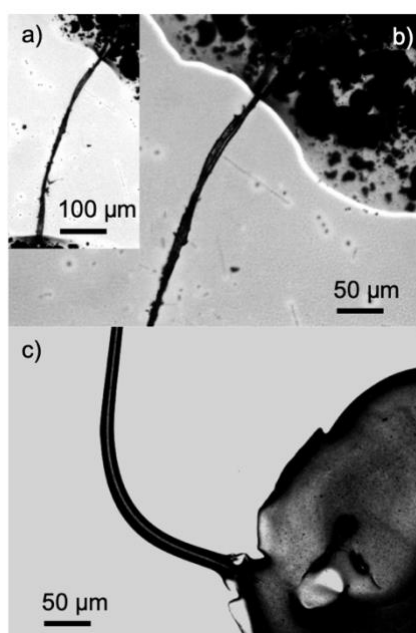


Figure 71: Use of different glues and imbibition of the glue into the fibre. a) Entire fibre, both ends fixed with the glue. No glue has been soaked into the fibre. b) Closeup of the fibre structure. c) Here a glue has been soaked into the fibre.



Figure 72: CLSM three-dimensional representation of the investigated paper fibre.

8.1.2 Strategy for calculation the eccentricity

This strategy is extracted from *J. R. Barber* (131).

I. Use equation to determine A and B

$$A + B = 0.5 \left(\frac{1}{R_x^1} + \frac{1}{R_y^1} + \frac{1}{R_x^2} + \frac{1}{R_y^2} \right) \quad (30)$$

R_x and R_y are the principal radii of curvature of the surface.

With

$$\frac{1}{R_x} = 2A = \frac{1}{R_x^1} + \frac{1}{R_x^2} \quad (31)$$

And

$$\frac{1}{R_y} = 2B = \frac{1}{R_y^1} + \frac{1}{R_y^2} \quad (32)$$

II. Read out e from the graph

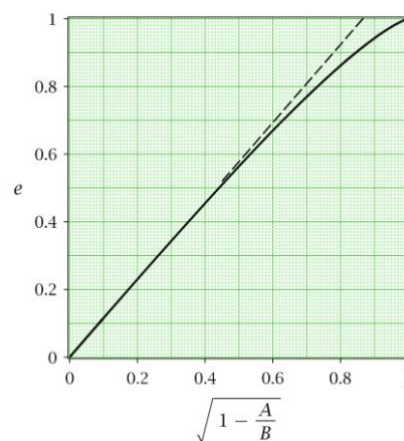


Figure 73: Eccentricity e of the contact area as a function of $\sqrt{(1-A/B)}$. From *J. R. Barber* (131).

III. Read out the elliptical integrals $K(e)$ and $E(e)$

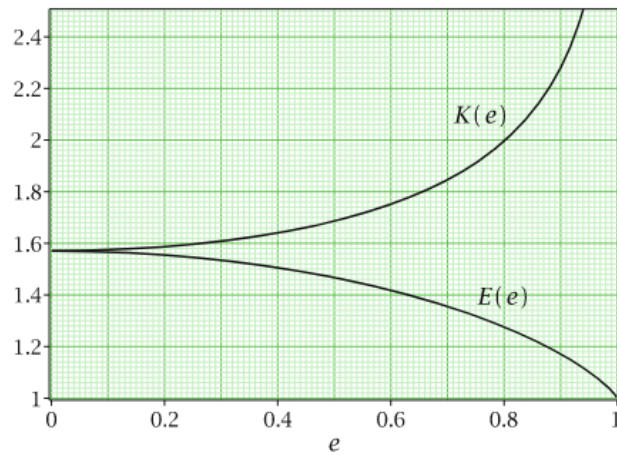


Figure 74: The complete elliptic integrals $K(e)$, $E(e)$ as functions of eccentricity e . From J. R. Barber (131).

IV. Calculate the ellipse major and minor axis a and b

$$a = \left(\frac{3P[K(e) - E(e)]}{2\pi e^2 E^* A} \right)^{\frac{1}{3}} \quad (33)$$

and

$$b = a\sqrt{1 - e^2} \quad (34)$$

P is the applied force.

V. Repeat

- Repeat these steps for every bending point and every applied force.
- Thus, one gets out elliptical contact areas for every applied force and every fibre surface curvature.

8.1.3 DMT moduli

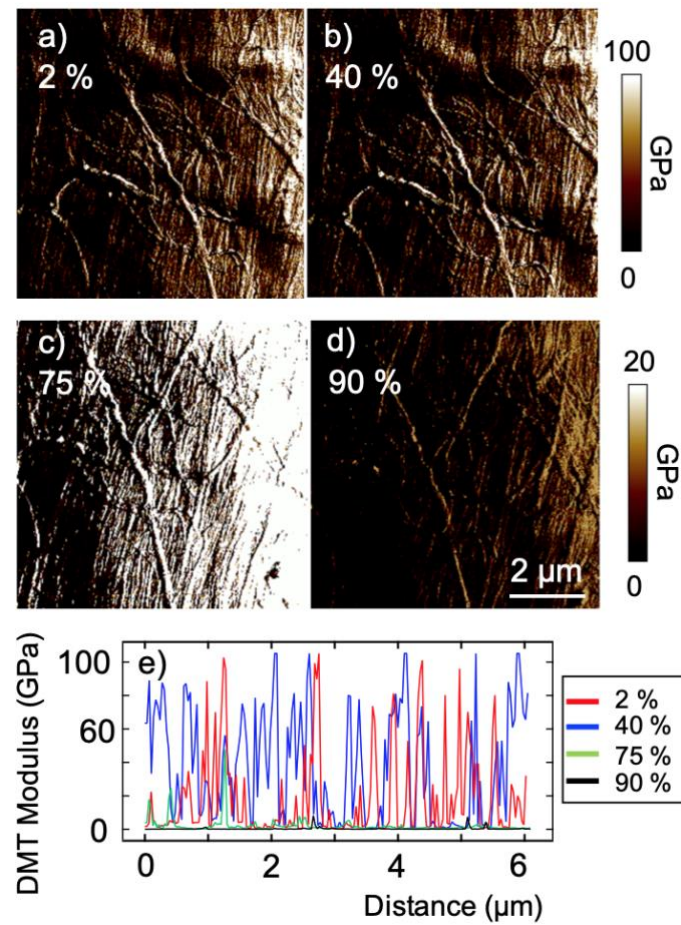


Figure 75: Typical DMT modulus maps in a-d) for 2%, 40%, 75% and 90% RH. e) Typical cross sections across a-d) highlighting the reduced stiffness variation in c) and d), i.e. for 75% and 90% RH.

8.1.4 Repeatability of measurement

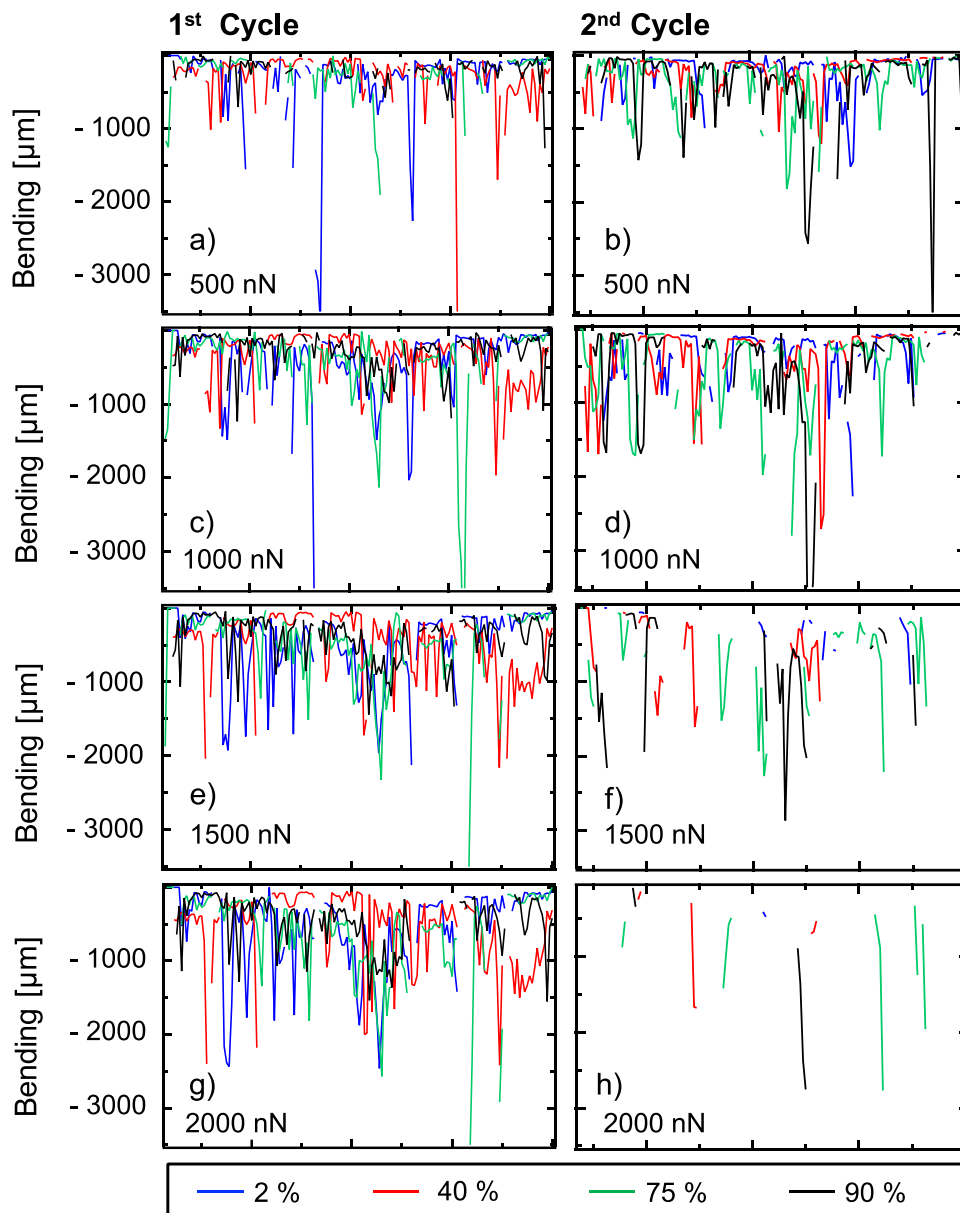


Figure 76: The first cycle of changing the RH is on the left side and the second cycle on the right. a), b) displays the bending at 500 nN, c), d) at 1000 nN, e), f) at 1500 nN and g), h) at 2000 nN. The blue lines are at 2 %, red at 40 %, green at 75 % and black at 90 % RH.

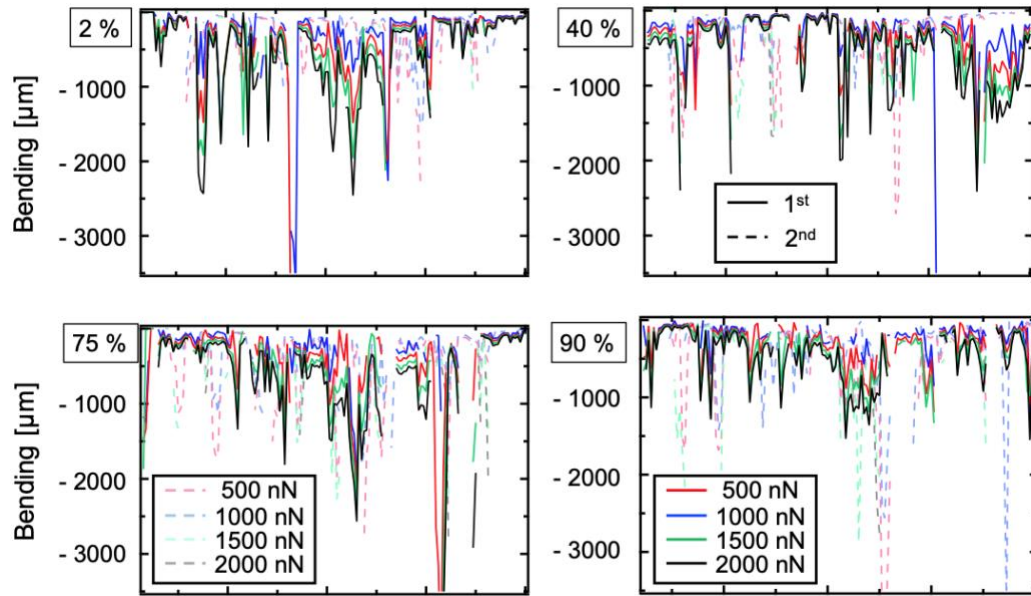


Figure 77: Bending along the longitudinal direction of the fibre at different RHs in both cycles. a) at 2 % RH, b) at 40 % RH, c) at 75 % RH and d) at 90 % RH. The first cycle is plotted in solid lines and the second cycle in dashed lines.

8.2 Supplementary information to chapter 4

8.2.1 Force-distance curves with local fits

In the following force-distance curves with their local $\delta^{3/2}$ and δ fits are shown.

The force-distance curves with their fits are representative curves for the measurements. For the comparison of the tip geometries (HSC and HAR), similar appearing force curves of both measurements are shown to compare both local fits.

The local fits of $\delta^{3/2}$ and δ (images b), c) for HSC cantilevers and e), f) for HAR cantilevers) are shown in the black curves. The blue points are the recorded indentation points for the applied forces.

Figure 78a, b and c) shows the graphs for the PF fibres mapped with the HSC cantilever in and d, e and f) mapped with the HAR cantilever.

Figure 79a, b and c) shows the graphs for the wet PF fibres mapped with the HSC cantilever in and d, e and f) mapped with the HAR cantilever.

Figure 80a, b and c) shows the graphs for the UPF fibres mapped with the HSC cantilever in and d, e and f) mapped with the HAR cantilever.

Figure 81a, b and c) shows the graphs for the wet UPF fibres mapped with the HSC cantilever in and d, e and f) mapped with the HAR cantilever.

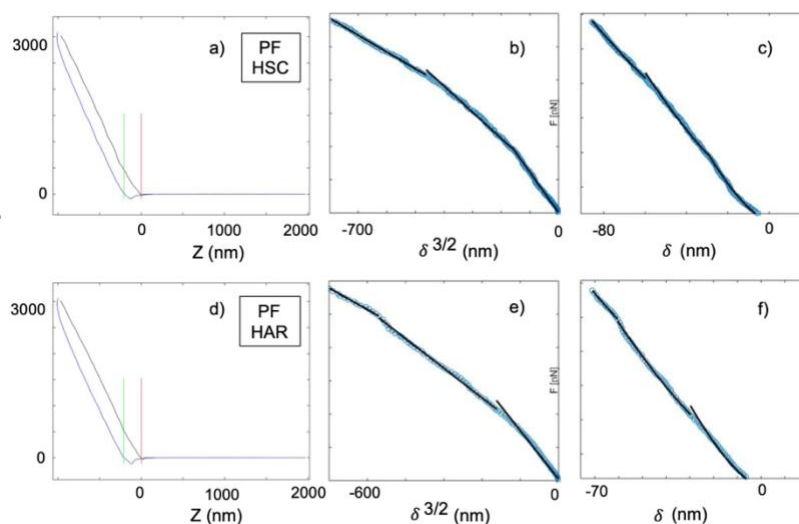


Figure 78: Force-distance curves with corresponding fits of $\delta^{3/2}$ in nm and of δ in nm of the PF. a, b and c) are recorded with the HSC cantilever and d, e and f) are recorded with the HAR cantilever. The contact point in a) and d) are marked with vertical red lines. The fits of the Hertzian contact model in b, c, e and f) are shown in the black curves.

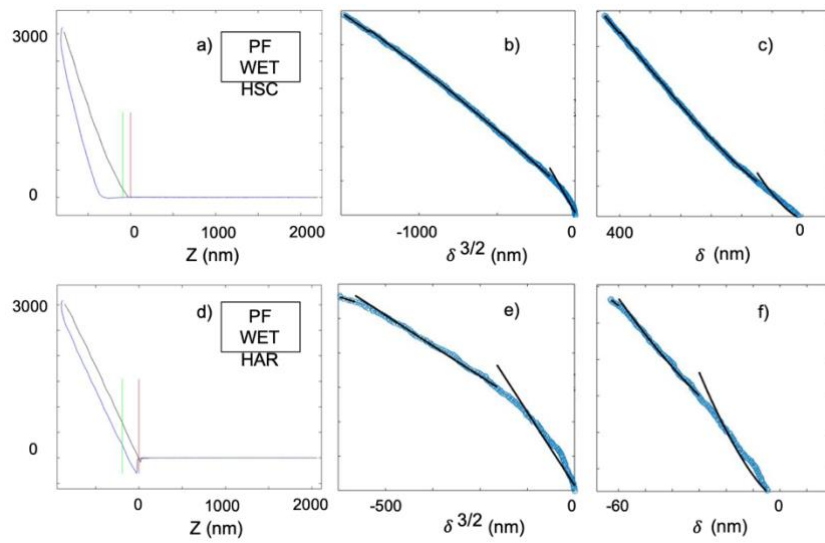


Figure 79: Force-distance curves with corresponding fits of $\delta^{3/2}$ in nm and of δ in nm of the PF in wet state. a, b and c) are recorded with the HSC cantilever and d, e and f) are recorded with the HAR cantilever. The contact point in a) and d) are marked with vertical red lines. The fits of the Hertzian contact model in b, c, e and f) are shown in the black curves.

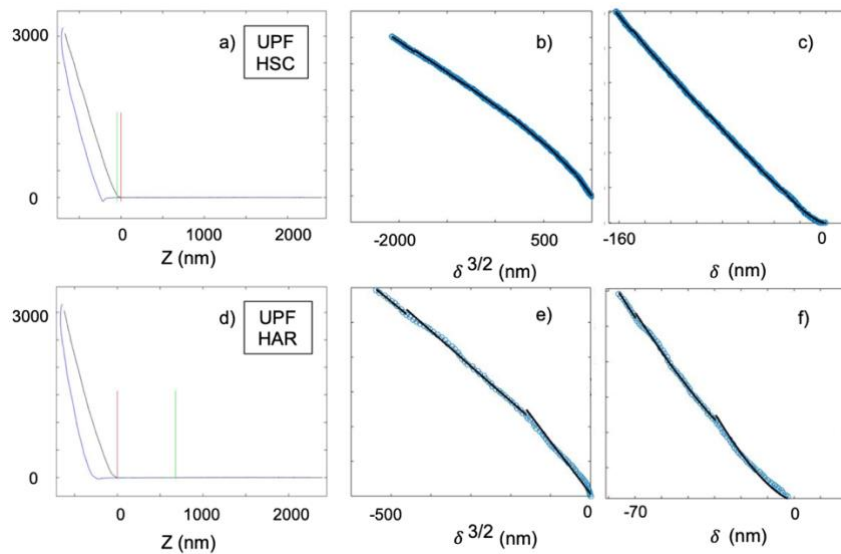


Figure 80: Force-distance curves with corresponding fits of $\delta^{3/2}$ in nm and of δ in nm of the UPF. a, b and c) are recorded with the HSC cantilever and d, e and f) are recorded with the HAR cantilever. The contact point in a) and d) are marked with vertical red lines. The fits of the Hertzian contact model in b, c, e and f) are shown in the black curves.

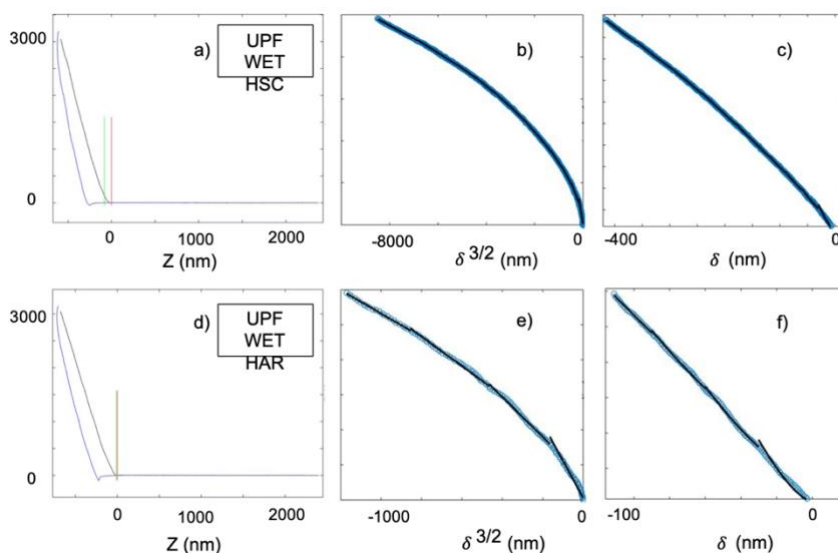


Figure 81: Force-distance curves with corresponding fits of $\delta^{3/2}$ in nm and of δ in nm of the UPF in wet state. a, b and c) are recorded with the HSC cantilever and d, e and f) are recorded with the HAR cantilever. The contact point in a) and d) are marked with vertical red lines. The fits of the Hertzian contact model in b, c, e and f) are shown in the black curves.

8.2.2 Imprints in force-volume mapping

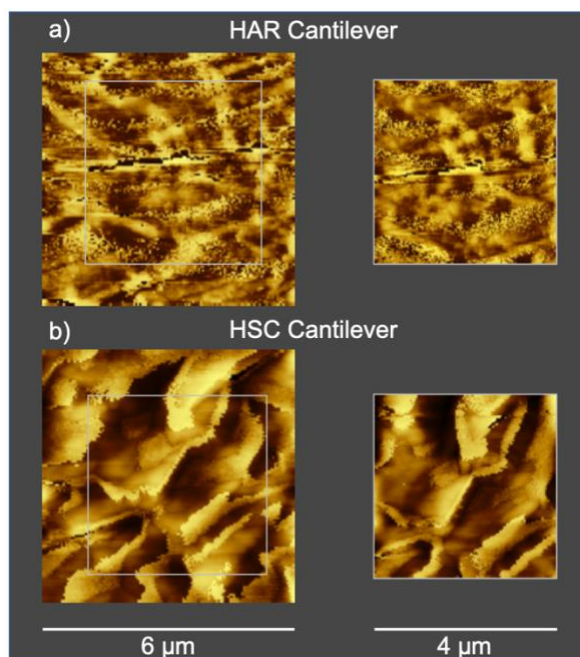


Figure 82: AFM topography maps. a) Maps with a HAR cantilever in dry state. b) Maps with a HSC cantilever in wet state.

As seen in Figure 82 the applied force-volume mapping is not destroying the fibres surface as no imprint of the $4 \times 4 \mu\text{m}$ scan shape is visible in the $6 \times 6 \mu\text{m}$ scan. This applies also in wet state.

8.3 Supplementary Information to chapter 5

The Raman spectrum of the terpolymer P(s-co-MABP-co-PyMA) in Figure 83 showed a superposition of the Raman spectra of the single components PS, BP, and Pyrene. The green labeled peaks in the Raman spectrum are listed in Table 9.

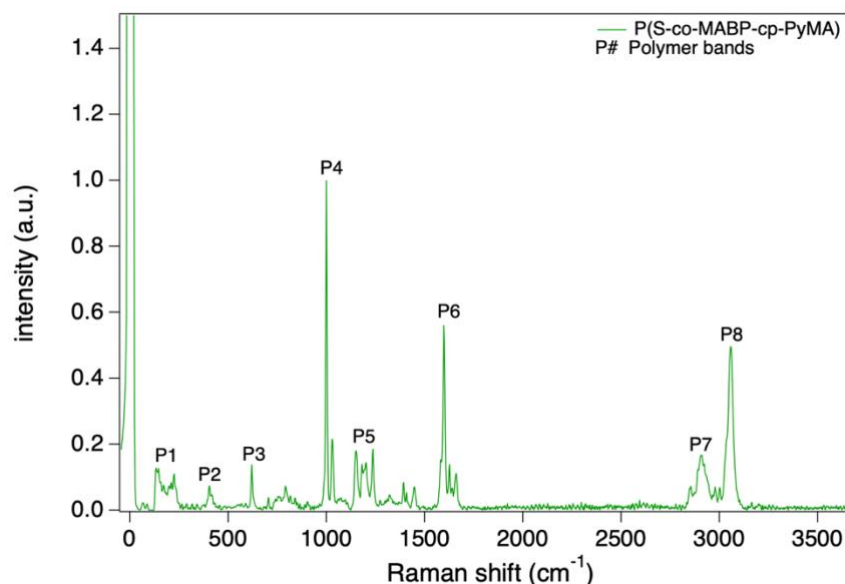


Figure 83: Raman spectrum of P(S-co-MABP-co-PyMA) with the labeled polymer bands. The spectrum was taken with 10 accumulation and 10s integration time each.

Table 9: Characteristic vibrational motions of cellulose (179), PS (180, 181), BP (182), and Pyrene (183).

Label (Fig. 5 and Fig. S3)	Raman shift (cm ⁻¹)	Bond	Movement	Material
P1	137-225	Carbonyl group	Deformation and Torsion	Benzophenone (BP)
C1	379-516	CC, COC OCC, OCO	Skeletal bend	Cellulose
P2	405		Skeletal stretching	Pyrene, BP
P3	619	Phenyl ring	Deformation	BP
P4	1000	CH, CC	Rocking, Stretching	PS, BP
C2	1095, 1118	CC, CO	Stretching	Cellulose
C3	1290	HCC, HCO	Bending	Cellulose
P5	1151-1392	CH, CCC, CH	Stretching, Bending	Pyrene, BP, PS

C4	1334, 1376, 1476	HCC, HCO, HOC, HCH	Bending	Cellulose
P6	1598	CC, Ring	Stretching	Pyrene, PS, BP
C5	2800-3000	CH, CH ₂	Stretching	Cellulose
P7	2800-3000	CH, CH ₂	Stretching	PS, BP
P8	3058	CH	Stretching	PS, BP
C6	3200-3500	OH	Stretching	Cellulose

Hydration experiments with *in situ* Raman spectroscopy using point scans are shown in Figure 84a) and b) for linter and eucalyptus, respectively. The results of the humidity experiments with an extended adjustment time of 180 min are given in Figure 84c) and d). For the adjustment times of 60 min point Raman measurements were used, while for the extended humidity adjustment times (180 min) mapsans were used.

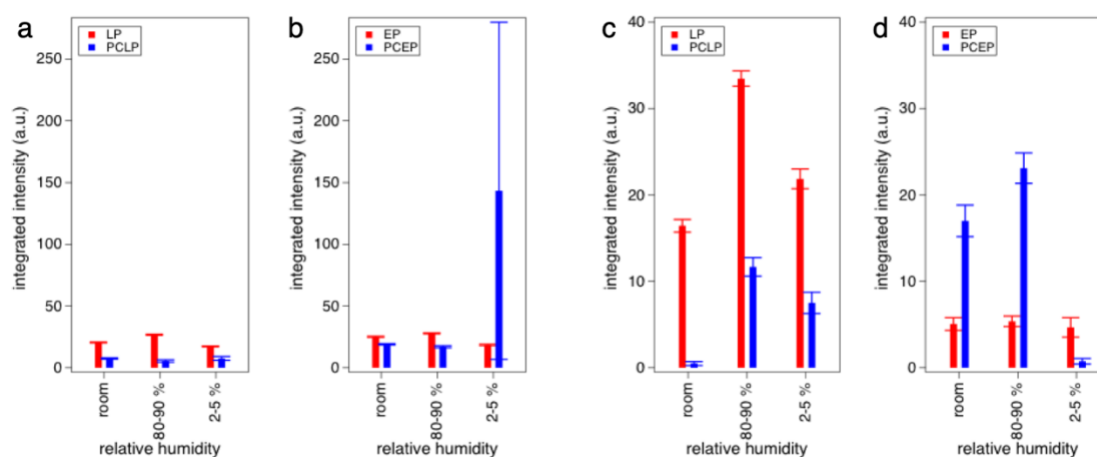
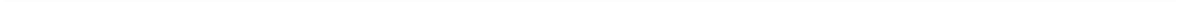


Figure 84: Results from hydration experiments with *in situ* Raman spectroscopy for different humidity adjustment times: 60 min (a and b) and 180min (c and d) and different materials: LP and PCLP (a and c), EP and PCEP (b and d). The unmodified paper samples are represented in red (left bar), the polymer coated ones in blue (right bar). The integrated intensity is the summed intensity in the OH stretching spectral region (3200-3500 cm⁻¹)





9 Table of Figures

Figure 1: Molecular structure of cellulose. The hydrogen bonds are indicated in the dashed blue lines. N displays the degree of polymerisation.....	5
Figure 2: Schematic composition of a paper fibre. The elementary fibrils are formed by the cellulose molecules. They are connecting to microfibrils, which form together the macrofibrils. Those are forming the final paper fibre.	7
Figure 3: Schematic composition of the layer structure of a cotton fibre. The lines within the different layers represent the arrangement of the fibrils.....	7
Figure 4: Mechanisms for increasing the wet strength of cellulose. The wet strengthening agents is presented in red before the thermal induced linking and in light blue afterwards. The linking points in the protection mechanism and in the reinforcement mechanism are indicated in blue.....	10
Figure 5: Reaction scheme and representation of the terpolymer P(S-co-MABP-co-PyMA).	11
Figure 6: Reaction scheme and representation of the terpolymer P(S-co-MABP-co-RhodBMA).	14
Figure 7: Schematics of the contact area between two fibres. It is divided in visible and molecular contact area. The visible contact area is marked in yellow and the molecular contact area in red.....	18
Figure 8: Schematic set up of an atomic force microscope (AFM).....	21
Figure 9: Mode of operation of the feedback mechanism.....	22
Figure 10: Schematics of long- and short range forces between the tip and the sample surface.	23
Figure 11: Power spectral density plotted over the frequency.....	24
Figure 12: Schematics of a force-distance curve with mechanical properties.	26
Figure 13: Contact mechanics of the Hertz model, DMT model and JKR model. F is the applied force, F_{AD} the adhesion force and R the tip radius.....	27
Figure 14: Schematics of the confocal principle in a confocal laser scanning microscope.....	32
Figure 15: Set up of a Raman spectrometer and beam path. The laser beam path is shown in green.....	33
Figure 16: Scattering processes in Raman spectroscopy. In blue the inelastic Stokes scattering is shown. The elastic Rayleigh scattering is shown in turquoise and the inelastic Anti-Stokes scattering shown in red.....	34
Figure 17: Schematics of the interaction of a liquid drop with a hydrophobic surface in a) and a hydrophilic surface in b).....	35
Figure 18: Schematic set up of an SEM.....	36

Figure 19: Excitation bulb and different types of interactions with the electron beams and the area where they originate.....	37
Figure 20: A representative CLSM measurement of the cross section of the fibre surface of a loading point of the fibre. The estimated fibre surface curvature radius is indicated in red. Note that R_{Fibre} parameterises a local curvature and not the cross section of the fibre.	46
Figure 21: Schematics of the section-wise scanning process along the longitudinal direction of the fibre. At every section, the scanning trajectory was realigned to the fibre axis....	47
Figure 22: a) Schematic force-distance curve with extracted mechanical properties. b) Force-bending curve with visualization of multiple virtual setpoint forces F	48
Figure 23: a-d) Force-bending curves measured at different RHs. The curves from loading point #15 (from left to right in figure 9) are shown. In blue: trace curve, in red: retrace curve. The force-bending curves exhibited a slightly non-linear force-bending relationship. Therefore, the bending at different forces to create a map which highlights strongly non-linear regions were read out. e-h) Force-time plots of the corresponding force-bending curves at the different RHs.....	48
Figure 24: a) Schematic of a conventional three-point bending test. b) Cross section of a fibre and the corresponding equations for a three-point bending test. c) Principle of a scanning three-point bending test.....	50
Figure 25: Schematics of the contact mechanics between the colloidal probe and the fibre. a) Before contact and b) in contact. The elliptical contact area is illustrated in c). In d) the geometrical relations between the colloidal probe and the fibre are shown.....	53
Figure 26: Schematics of the calculation of the elongation ΔL	54
Figure 27: a) CLSM microscopy image of the investigated fibre. The coloured boxed indicate the ROIs. b) The normalised change in $R_{\text{Fibre}}/RRH=2$ is displayed over the relative humidity in % of the marked regions of a).....	55
Figure 28: SE images of fibre sections. a) ROI I b) ROI II c) ROI III, d) ROI IV.	56
Figure 29: Mechanical characterisation of a cellulose fibre along the longitudinal direction of the fibre. From top to bottom: CSLM image of the fibre with the local adhesion and dissipation maps along the fibre beneath. The scale bars are -800 to 0 nN (adhesion) and 1 to 1×10^5 J (dissipation). Beneath: bending behaviour, contact stress (error 30 %) and strain (error 25 %) along the fibre. The mechanical properties in a) are at 2 % RH, b) at 40 % RH, c) 75 % RH and d) 90 % RH. The discussed ROIs are marked with II, IV, and V.	58
Figure 30: Adhesion and dissipation maps along the longitudinal direction of the fibre. a) CLSM image of the fibre, b) of adhesion maps and c) corresponding cross-sections along	

the fibre at different RHs. d) CLSM image of the fibre (same as a), b) dissipation map and c) corresponding cross sections along the fibre at different RHs.....	59
Figure 31: Bending along the longitudinal direction of the fibre at different RHs. a) at 500 nN, b) at 1000 nN, c) at 1500 nN and d) at 2000 nN. The ROI V is marked in yellow. Data close to the fibre attachment (red) can be attributed to experimental noise (probe slippage).	60
Figure 32: Stress-strain diagrams of ROI I in a) of ROI II in b) and of ROI III in c).....	61
Figure 33: Young's modulus (normalised to the modulus at RH = 2 %) versus the RH for ROIs I-III.....	63
Figure 34: a) and b) displays a CLSM image of the first and second cycle of changing the RH with the respective ROIs of interest. c) and d) show the normalised change in RFibre over the RH for the first and second cycle of changing the RH (colour coded with respect to the ROI)	64
Figure 35: The CLSM images as well as the mechanical properties such as adhesion, dissipation and the bending abilities for two cycles of changing the RH are shown.....	65
Figure 36: a-d) Adhesion properties along the longitudinal direction of the fibre of both RH cycles. The 1st cycle is plotted in solid lines and the 2nd cycle in dashed lines. e-h) Dissipation properties along the longitudinal direction of the fibre of both RH cycles. The 1st cycle is plotted in solid lines and the 2nd cycle in dashed lines.	66
Figure 37: a) Point-wise adhesion coefficient: Adhesion of the 1st cycle divided by the 2nd cycle properties along the longitudinal direction of the fibre at the different RHs. b) Point-wise dissipation coefficient: Dissipation of the 1st cycle divided by the 2nd cycle properties along the longitudinal direction of the fibre at the different RHs.	67
Figure 38: Principle of the stepwise analysis of a force-distance curve. The local fits are indicated in red. The indentation depth is calculated as the distance from the contact point.....	77
Figure 39: SE images of the tip geometry for a) the HSC cantilever and b) the HAR cantilever.	78
Figure 40: a) 3D representation of the surface profile of a PF recorded with a HSC cantilever. The colour in the z-direction encodes the local stiffness beneath the surface. b) A cross-sectional profile of Elok(z) in the xz- and yz-directions as indicated.....	81
Figure 41: Depth profile of Elok(z) in the xz-direction of a PF mapped with an HSC cantilever in a) and an HSC cantilever in b) and of UPF mapped with an HSC cantilever in c) and an HAR cantilever in d).....	82
Figure 42: Depth profiles of this Elok(z) of a) a UPF, b) a PF and c) a combined graph of UPF and PF. In c), the UPF profiles are plotted in red, and the PF profiles are plotted in blue.	

The suggested corresponding wall layers are indicated with different colours. The C layer is highlighted in dark blue, the P wall in blue, the S1 layer in light blue and the S2 layer in grey. The error bars are $\pm 30\%$ of the values. The 3 profiles in a) and b) were extracted from cross sections with a HSC cantilever. The profiles in c) were extracted with both cantilever types.....	84
Figure 43: 3D images of confocal fluorescence microscopy imaging. The fibres are labelled with CBM77 in green (binds to pectin), with CBM3a in cyan (binds to “semi-crystalline” cellulose) and with CBM1Cel6a in red (binds to crystalline cellulose). a) UPF fibre and b) PF fibre.	85
Figure 44: a) Image slice of the confocal fluorescence imaging of a UPF. The intensity peaks over the distance of the CMBs in the UPF are shown in b) for CBM1Cel6a, in c) for CBM3a and in d) for CBM77. In e), an image slice of the confocal fluorescence imaging of a PF is shown. The intensity peaks over the distance of the CMBs in the PF are shown in f) for CBM1Cel6a, in g) for CBM3a and in h) for CBM77. The peaks of the corresponding CBMs are marked in the green (CBM77), blue (CBM3a) and red (CBM1Cel6a) boxes.....	86
Figure 45: Fibril orientation in the applied load direction in a) the tensile test and b) force-volume mapping. In the tensile test, the fibrils of the S2 layer are oriented parallel to the applied force. In the Force-Volume Mapping, the fibrils of the S2 layer are oriented perpendicular to the applied force. Thus, the fibrils from the S2 layers can be bend down locally as shown in figure b).	88
Figure 46: Cross section of Elok(z) in the xz-direction of a hydrated PF mapped with a) an HSC cantilever and b) an HAR cantilever. Cross section of Elok(z) in the xz-direction of a hydrated UPF mapped with c) an HSC cantilever and d) an HAR cantilever.	89
Figure 47: Experimental setup for humidity experiments including a water wash bottle, a N2 gas inlet, a hygrometer, and a small tooth comb as the sample holder with the fibre bundles.	98
Figure 48: Schematic setup of AFM experiments. (a) Schematics of nanoindentation experiments, (b) deflection versus separation curve with InvOLS shown, (c) schematics of nanomechanical mapping and (d) force versus distance curve with extracted mechanical properties.....	102
Figure 49: Images of 2 μl water drops on (a) LP, (b) EP, (c) PCLP, and (d) PCEP for CA measurements. The scale bar is 500 μm	103
Figure 50: SEM images of sheets made of (a) LP, (b) (EP), (c) PCLP, and (d) PCEP. (scale bar: (a,b,d) 5 μm and (c) 10 μm).....	104
Figure 51: SEM images of a) LP, b) EP, c) PCLP and d) PCEP at 1500x magnification.	105

Figure 52: Overlay of bright field microscopy (grey) and fluorescence microscopy images (yellow) at 5x and 10x, showing sheets of (a) PCLP and (d) PCEP, as well as near-surface fibres of (b,c) PCLP and (e,f) PCEP. The scale bar represents 300 μm . The red areas shows regions without a polymer coating, therefore revealing the inhomogeneous coating distribution.....	105
Figure 53: Fluorescence Microscopy images of the unmodified paper samples LP (a) and EP (b). The scale bar represents 300 μm	106
Figure 54: Raman spectra of (a) LP and PCLP and (b) EP and PCEP with assigned cellulose (C#) and polymer (P#) Raman bands. Unmodified paper is given in red, and polymer-coated paper is given in blue. The spectra were taken at 20x/0.4 with 10 accumulations and a 10-s integration time each. The measurements werke taken on the paper surface where there was a crosslink of paper fibres. The peak assignments can be found in Table 9.	107
Figure 55: Relative peak intensities of the band assigned to OH stretching obtained in hydration experiments with in situ Raman spectroscopy for (a) LP and PCLP and (b) EP and PCEP. Data of the unmodified paper samples are represented in red (left bar), and the polymer-coated samples are represented in blue (right bar). The integrated intensity is the summed intensity of OH stretching in the spectral region of 3200-3500 cm^{-1} . .	108
Figure 56: Mechanical resistance against indentation of the AFM probe into (a) LP and PCLP and (b) EP and PCEP in the setup with a fixed distance between attachment points (F). Region I depicts the state under room conditions, region II shows the soaked state and region III is the after-drying state.....	111
Figure 57: AFM images of LP fibres. The RH was varied from 2 % to a wet condition. (a-d) Topography images, (e-h) DMT modulus maps and (i-l) adhesion maps. The scale bar is 800 nm. The colour bar is -1 – 1.3 μm for topography images, 0 – 3 GPa for DMT modulus maps and 0 – 2 nN for adhesion maps. In the white framed topography images, the colour scale was modified to 0 – 250 nm. The white boxed images in a) and d) show the topography of the swollen microfibrils. An amorphous region of cellulose is highlighted in green, while the crystalline region is marked in red, and a transition between crystalline and amorphous regions is shown in blue.	112
Figure 58: Cross sections corresponding to figure 8 of the DMT modulus in (a) a transition area between crystalline, amorphous and crystalline regions. The crystalline regions are highlighted in light blue, and the amorphous region is highlighted in light orange. The cross sections of the DMT modulus and adhesion of a crystalline region are represented in (b), whereas (c) illustrates this for an amorphous region.	114

Figure 59: a) Normalised DMT modulus and b) normalised adhesion/radius plotted against the relative humidity in unmodified fibres and polymer-coated fibres.	115
Figure 60: AFM images of a PCEP fibre with a homogeneously coated area. a) Topography image at 2 % RH with the corresponding mechanical properties of d) DMT modulus and f) adhesion. b) The topography image under wet conditions with the associated mechanical properties of e) DMT modulus and g) adhesion. The scale bar represents 2 μm . The colour scale ranges from -550 – 550 nm for topography images, from 0 – 300 MPa for DMT modulus maps and from 0 – 10 nN for adhesion maps. h) and i) The cross sections of the DMT modulus and adhesion of the PCEP fibre.	117
Figure 61: Schematic setup of the FFJ and the position of the cantilever. The cantilever is positioned on the bottom fibre, which is connected to the top fibre. The top fibre is attached to the sample holder.....	126
Figure 62: a) Optical image of a FFJ. The bonded area is marked in white and the angle between the fibres is marked in red. The cantilever is positioned next to the fibre-fibre crossing. b) Schematic force-bending curve. The maximum force is the first bending is schematically marked for two cycles in the dashed red lines. Also, the maximum force for the 2nd -10th bending cycles is schematically marked for two cycles in the dashed green lines.....	128
Figure 63: Images of 2 μL sessile drops of a) H ₂ O-based polymer and of b) IPA-based polymer on a cotton linter sheet.....	129
Figure 64: CLSM image of fibre-fibre joint modified with the polymer coating. The cellulose components are displayed in cyan and the polymer distribution in purple.	130
Figure 65: Maximum Force in μN over Cycles of the different FFJ. The blue points represent the force values at 2 % RH, the red points at 40 % RH, the green points at 75 % RH and the black points at 90% RH. a) Plain FFJ, b) H ₂ O based polymer coating and c) IPA based polymer coating.....	132
After discussing the maximum applied force over 50 cycles, the maximum force is related to the bonded area and the bonding angle between the two fibres. It was shown that the maximum force returned to the maximum force valued before withdrawing and approaching the cantilever. Thus, the average value of the maximum force could be calculated without a high standard deviation. The results of the average maximum force values in μN plotted over the bonded area in μm^2 and the bonding angle in $^\circ$ are shown in Figure 67a) and b). The visible subdivision of the force values at the different RHs as seen in Figure 66 a) over cycle is also noticeable in Figure 67. To get a better observable relationship between the maximum force, angle and bonded area, the drawn surfaces are related to the force values. This is shown in Figure 67c)-f).	133

Figure 67: a) and b) 3D plots of the average force values of the plain FFJ over the angle and bonded area. The blue points represent the force values at 2 % RH, the red points at 40 % RH, the green points at 75 % RH and the black points at 90% RH. c-f) 3D Surface plots of the average force values of the plain FFJ over the angle and bonded area. g) and h) displays the close ups of 75 % and 90 % RH. 134

To prevent the softening of the FFJ when increasing the, the polymer P(DMAA-co-MABP-co-RhodBMA) diluted in H₂O and IPA was sprayed onto FFJ. The maximum applied force over the 50 bending cycles for the polymer diluted in H₂O is shown in Figure 68b). In this plot there is no clear subdivision of the force values from the different RHs visible. This is a first indication that the hydrophobic polymer coating could be effective in protecting the FFJ against softening when the RH is increased. Another noticeable fact is that in most of the bending series over the 50 cycles did not have a decay in the maximum force value when withdrawing and approaching every 10th cycle the cantilever. This is a further indication that the polymer coating is effective and strengthens the FFJ, even in dry state. With the polymer coating the bottom fibre is not able to separate as much as without a coating from the fixed top fibre. Therefore, the bond did not have to recover from the bended status. The bending series with a distinctive decay is attributed to a not homogenous or incomplete polymer coating. This circumstance will be discussed later on. 135

Figure 69: 3D plots of the average force values of the H₂O based und IPA based polymer coated FFJ over the angle and bonded area. H₂O polymer: The turquoise points represent the force values at 2 % RH, the pink points at 40 % RH, the light green points at 75 % RH and the grey points at 90% RH. IPA polymer: The light blue points represent the force values at 2 % RH, the magenta points at 40 % RH, the light green points at 75 % RH and the light grey points at 90% RH. 136

Figure 70: 3D plots of the average force values of the plain, H₂O based und IPA based polymer coated FFJ over the angle and bonded area. a) at 2 % RH, b) at 40 % RH, c) 75 % RH and d) 90 % RH..... 138

Figure 71: Use of different glues and imbibition of the glue into the fibre. a) Entire fibre, both ends fixed with the glue. No glue has been soaked into the fibre. b) Closeup of the fibre structure. c) Here a glue has been soaked into the fibre. 146

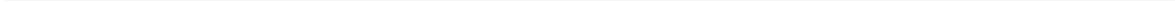
Figure 72: CLSM three-dimensional representation of the investigated paper fibre..... 146

Figure 73: Eccentricity e of the contact area as a function of $\sqrt{(1-A/B)}$. From J. R. Barber (130). 147

Figure 74: The complete elliptic integrals $K(e)$, $E(e)$ as functions of eccentricity e . From J. R. Barber (130). 148

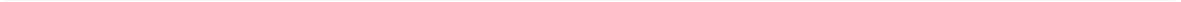
Figure 75: Typical DMT modulus maps in a-d) for 2%, 40%, 75% and 90% RH. e) Typical cross sections across a-d) highlighting the reduced stiffness variation in c) and d), i.e. for 75% and 90% RH.....	149
Figure 76: The first cycle of changing the RH is on the left side and the second cycle on the right. a), b) displays the bending at 500 nN, c), d) at 1000 nN, e), f) at 1500 nN and g), h) at 2000 nN. The blue lines are at 2 %, red at 40 %, green at 75 % and black at 90 % RH.	150
Figure 77: Bending along the longitudinal direction of the fibre at different RHs in both cycles. a) at 2 % RH, b) at 40 % RH, c) at 75 % RH and d) at 90 % RH. The first cycle is plotted in solid lines and the second cycle in dashed lines.	151
Figure 78: Force-distance curves with corresponding fits of $\sqrt[3]{\delta^3/2}$ in nm and of δ in nm of the PF. a, b and c) are recorded with the HSC cantilever and d, e and f) are recorded with the HAR cantilever. The contact point in a) and d) are marked with vertical red lines. The fits of the Hertzian contact model in b, c, e and f) are shown in the black curves.	152
Figure 79: Force-distance curves with corresponding fits of $\sqrt[3]{\delta^3/2}$ in nm and of δ in nm of the PF in wet state. a, b and c) are recorded with the HSC cantilever and d, e and f) are recorded with the HAR cantilever. The contact point in a) and d) are marked with vertical red lines. The fits of the Hertzian contact model in b, c, e and f) are shown in the black curves.....	153
Figure 80: Force-distance curves with corresponding fits of $\sqrt[3]{\delta^3/2}$ in nm and of δ in nm of the UPF. a, b and c) are recorded with the HSC cantilever and d, e and f) are recorded with the HAR cantilever. The contact point in a) and d) are marked with vertical red lines. The fits of the Hertzian contact model in b, c, e and f) are shown in the black curves.....	153
Figure 81: Force-distance curves with corresponding fits of $\sqrt[3]{\delta^3/2}$ in nm and of δ in nm of the UPF in wet state. a, b and c) are recorded with the HSC cantilever and d, e and f) are recorded with the HAR cantilever. The contact point in a) and d) are marked with vertical red lines. The fits of the Hertzian contact model in b, c, e and f) are shown in the black curves.....	154
Figure 82: AFM topography maps. a) Maps with a HAR cantilever in dry state. b) Maps with a HSC cantilever in wet state.....	154
Figure 83: Raman spectrum of P(S-co-MABP-co-PyMA) with the labeled polymer bands. The spectrum was taken with 10 accumulation and 10s integration time each.	155
Figure 84: Results from hydration experiments with in situ Raman spectroscopy for different humidity adjustment times: 60 min (a and b) and 180min (c and d) and different materials: LP and PCLP (a and c), EP and PCEP (b and d). The unmodified paper samples are represented in red (left bar), the polymer coated ones in blue (right bar). The	

integrated intensity is the summed intensity in the OH stretching spectral region (3200-3500 cm⁻¹) 156



10 List of Abbreviations

AFM	Atomic Force Microscopy
CLSM	Confocal Laser Scanning Microscopy
SEM	Scanning Electron Microscopy
RH	Relative Humidity
C	Cuticula
P	Primary wall
S1	Secondary Wall 1
S2	Secondary Wall 2
S3	Secondary Wall 3
HAR	High Aspect Ratio
HSC	High Spring Constant
PF	Processed Fibre
UPF	Unprocessed Fibre
LF	Linter Fibre
LP	Coated Linter Fibre
EF	Eucalyptus Fibre
EP	Coated Eucalyptus Fibre
FFJ	Fibre-Fibre Joint
PFFJ	Polymer Coated Fibre-Fibre Joint
CW	Calcofluor White



11 References

1. J. Blechschmidt, Taschenbuch der Papiertechnik. *Fachbuchverlag Leipzig im Carl Hanser Verlag, München* **2. Auflage** (2013).
2. Statista.com (Zugriff am 18.06.2020) VDP. n.d. Weltweiter Verbrauch von Papier, Karton und Pappe
3. V. D. P. (VDP) (April 2020) Statistische Kurzinformation Zellstoff- und Papierindustrie in Deutschland.
4. S. Bump *et al.*, Spatial, spectral, radiometric, and temporal analysis of polymer-modified paper substrates using fluorescence microscopy. *Cellulose* **22**, 73-88 (2015).
5. C. Ruettiger *et al.*, Redox-mediated flux control in functional paper. *Polymer* **98**, 429-436 (2016).
6. N. Gurnagul, D. H. Page, The difference between dry and rewetted zero-span tensile-strength of paper. *Tappi J.* **72**, 164-167 (1989).
7. J. L. Delaney, C. F. Hogan, J. F. Tian, W. Shen, Electrogenated Chemiluminescence Detection in Paper-Based Microfluidic Sensors. *Anal. Chem.* **83**, 1300-1306 (2011).
8. D. D. Liana, B. Raguse, J. J. Gooding, E. Chow, Recent Advances in Paper-Based Sensors. *Sensors* **12**, 11505-11526 (2012).
9. R. A. Hayes, B. J. Feenstra, Video-speed electronic paper based on electrowetting. *Nature* **425**, 383-385 (2003).
10. V. L. LM. Hillscher, O. Avrutina, M. Biesalski, H. Kolmar, Functional paper-based materials for diagnostics. *ChemTexts* **7** (2021).
11. M. Janko *et al.*, Cross-Linking Cellulosic Fibers with Photoreactive Polymers: Visualization with Confocal Raman and Fluorescence Microscopy. *Biomacromolecules* **16**, 2179-2187 (2015).
12. Z. A. Rogovin, L. S. Gal'brajch, *Die chemische Behandlung und Modifizierung der Zellulose* (Stuttgart u.a., 1983).
13. M. J. John, S. Thomas, Biofibres and biocomposites. *Carbohydr. Polym.* **71**, 343-364 (2008).
14. R. Q. Cabrera, F. Meersman, P. F. McMillan, V. Dmitriev, Nanomechanical and Structural Properties of Native Cellulose Under Compressive Stress. *Biomacromolecules* **12**, 2178-2183 (2011).
15. E. Gumuskaya, M. Usta, H. Kirci, The effects of various pulping conditions on crystalline structure of cellulose in cotton linters. *Polym Degrad Stabil* **81**, 559-564 (2003).
16. B. Lindman, G. Karlstrom, L. Stigsson, On the mechanism of dissolution of cellulose. *J. Mol. Liq.* **156**, 76-81 (2010).
17. N. Dunlop-Jones, Wet-strength chemistry. *Paper Chemistry*, 98 - 119 (1996).
18. L. C. Fidale, N. Ruiz, T. Heinze, O. A. El Seoud, Cellulose swelling by aprotic and protic solvents: What are the similarities and differences? *Macromol. Chem. Phys.* **209**, 1240-1254 (2008).
19. T. Yano, H. Ohtani, S. Tsuge, T. Obokata, DETERMINATION OF WET-STRENGTH RESIN IN PAPER BY PYROLYSIS-GAS CHROMATOGRAPHY. *Tappi J.* **74**, 197-201 (1991).
20. B. E. H. Pahl, Use of polyamide resins in board. *Tappi Wet and Dry Short Course* (1988).
21. W. Baumann, Papierchemikalien: Daten und Fakten zum Umweltschutz. *Springer Verlag* (2013).
22. M. Jocher, Photoreaktive Copolymere als neue, funktionelle Nassfestmittel in der Papiertechnologie. *Ph.D. Thesis, Technische Universität Darmstadt* (2018).
23. S. Wendenburg, Analyse und Steuerung des Retentionsverhaltens verschiedener Modellanalyte in mikrostrukturierten Papieren. *Ph.D. Thesis, Technische Universität Darmstadt* (2018).
24. K. Kamide, *Cellulose and Cellulose Derivatives* (Elsevier, 2005).
25. V. D. Papierfabriken, *Papier Kompakt* ((2020).

26. V. D. Papierfabriken, *Rohstoffe und ihre Aufbereitung* ((2020).
27. D. Roy, M. Semsarilar, J. T. Guthrie, S. Perrier, Cellulose modification by polymer grafting: a review. *Chem. Soc. Rev.* **38**, 2046-2064 (2009).
28. G. O. P. J. F. Kennedy, D. J. Wedlock and P. A. Williams, Ellis Horwood, *Cellulose and its derivatives: Chemistry, biochemistry and applications* (1985).
29. D. Klemm, B. Heublein, H. P. Fink, A. Bohn, Cellulose: Fascinating biopolymer and sustainable raw material. *Angew. Chem.-Int. Edit.* **44**, 3358-3393 (2005).
30. T. D. Arnaud Lejeune, *Cellulose: Structure and Properties, Derivatives and Industrial Uses*, Cellulose allomorphs - Overview and perspectives (Nova Science Publishers, Inc, 2010).
31. W. Blaschek, *Pharmazie in unserer Zeit*, Cellulose, ein interessanter Grundstoff für die pharmazeutische Nutzung (VCH Verlagsgesellschaft mbH, 1990), vol. 02.r0/0.
32. D. H. H. J. P. H.P. Fink, Zur Fibrillarstruktur nativer Cellulose. *Acta Polymerica* **41** (1990).
33. M. W. Ott, *Tailor-made cellulose graft copolymers by controlled radical polymerization techniques*, Ph.D. Thesis (Technische Universität Darmstadt, 2017).
34. R. R. Mather, R. H. Wardman, *The chemistry of textile fibres* (Royal Society of Chemistry, 2015).
35. A. Sctostak, *Cotton Linters: An Alternative Cellulosic Raw Material* (WILEY-VCH Verlag GmbH & Co.KGaA, Weinheim, 2009).
36. K. G. Satyanarayana *et al.*, Structure and Properties of Some Vegetable Fibers .3. Talipot and Palmyrah Fibers. *J. Mater. Sci.* **21**, 57-63 (1986).
37. R. A. Young, R. M. Rowell, *Cellulose : structure, modification and hydrolysis* (New York u.a., 1986).
38. Y. Müller, *Untersuchung von Bindemechanismen bei der Vernetzung von Cellulose* (Dresden, 2010).
39. J. Peters, *Strukturuntersuchungen an Cellulose und Cellulosederivaten aus ionischen Lösungsmitteln* (2004), vol. Dissertation.
40. H. H. Espy, THE MECHANISM OF WET-STRENGTH DEVELOPMENT IN PAPER - A REVIEW. *Tappi J.* **78**, 90-99 (1995).
41. B. D. Podd, The third generation of neutrally hardening polyamide-epichlorhydrin wet strength agents. *Wochenbl. Papierfabr.* **127**, 1388-1390 (1999).
42. M. G. A. Böhm, F. Carstens, S. Schabel, and M. Biesa, Designing microfabricated paper devices through tailored polymer attachment. *FRC – The Pulp and Paper Fundamental Research Society, Cambridge* (2013).
43. A. Boehm, Grafting Photo-reactive Copolymers to Cellulose Fibers for the Design of Microfluidic Papers. *PhD thesis, Technische Universität Darmstadt* (2014).
44. A. Böhm, Grafting photo-reactive copolymers to cellulose fibers for the design of microfluidic papers *TU Darmstadt* (2015).
45. A. Bohm, F. Carstens, C. Trieb, S. Schabel, M. Biesalski, Engineering microfluidic papers: effect of fiber source and paper sheet properties on capillary-driven fluid flow. *Microfluid. Nanofluid.* **16**, 789-799 (2014).
46. A. K. Bell, In situ Raman Spectroscopy on Paper Fibres during Tensile Testing and during Hydration. *Masterthesis, TU Darmstadt* (2017).
47. A. Boehm (2014) Grafting Photo-reactive Copolymers to Cellulose Fibers for the Design of Microfluidic Papers.
48. J.-L. Schäfer, Untersuchung von photovernetzbaeren Copolymeren in Papier zum besseren Verständnis von Nassfestmitteln. *Masterthesis, TU Darmstadt* (2018).
49. B. P. D. Klemm, T. Heinze, U. Heinze, and W. Wagenknecht, *Comprehensive Cellulose Chemistry. Volume 1. Fundamentals and Analytical Methods* (Wiley: Weinheim, Germany., 1998), vol. Volume 1.
50. R. A. C. B. Flávia P.Moraisa, Joana M.R.Curtoac, Maria E.C.C.Amarala, Ana M.M.S.Cartab, Dmitry V.Evtyugind, Comparative characterization of eucalyptus fibers and softwood fibers for tissue papers applications. *Materials Letters: X* **4** (2019).

51. K. M. Bhat, K. V. Bhat, T. K. Dhamodaran, WOOD DENSITY AND FIBER LENGTH OF EUCALYPTUS-GRANDIS GROWN IN KERALA, INDIA. *Wood Fiber Sci.* **22**, 54-61 (1990).
52. T. Lindström, L. Wagberg, T. Larsson, On the nature of joint strength in paper - A review of dry and wet strength resins used in paper manufacturing *Transactions of the 13th Fundamental Research Symposium, Cambridge*, 457-562 (2005).
53. A. K. Vainio, H. Paulapuro, Interfibre bonding and fibre segment activation in paper. *BioResources* **2**, 442-458 (2007).
54. H. W. Haslach, The moisture and rate-dependent mechanical properties of paper: A review. *Mech. Time-Depend. Mater.* **4**, 169-210 (2000).
55. B. N. J. Persson *et al.*, Adhesion of cellulose fibers in paper. *Journal of Physics-Condensed Matter* **25**, 11 (2013).
56. S. Rohm, U. Hirn, C. Ganser, C. Teichert, R. Schennach, Thin cellulose films as a model system for paper fibre bonds. *Cellulose* **21**, 237-249 (2014).
57. J. Rennel, Opacity in relation to strength properties of pulps. Effect of beating and wet pressing. *Pulp and Paper Magazine of Canada* **70**, 73-& (1969).
58. G. Urstoger, M. G. Simoes, A. Steinegger, R. Schennach, U. Hirn, Evaluating the degree of molecular contact between cellulose fiber surfaces using FRET microscopy. *Cellulose* **26**, 7037-7050 (2019).
59. L. Kappel, U. Hirn, E. Gilli, W. Bauer, R. Schennach, Revisiting polarized light microscopy for fiber-fiber bond area measurement - Part II: Proving the applicability. *Nord. Pulp Paper Res. J.* **25**, 71-75 (2010).
60. C. Marulier, P. J. J. Dumont, L. Orgeas, D. Caillerie, S. R. du Roscoat, Towards 3D analysis of pulp fibre networks at the fibre and bond levels. *Nord. Pulp Paper Res. J.* **27**, 245-255 (2012).
61. R. L. Thomson, and A. Ragauskas, Imaging cellulose fibre interfaces with fluorescence microscopy and resonance energy transfer. *Carbohydr. Polym.* **69**, 799-804 (2007).
62. Y. M. Haddad, A THEORETICAL APPROACH TO INTERFIBER BONDING OF CELLULOSE. *Journal of Colloid and Interface Science* **76**, 490-501 (1980).
63. A. D. French, M. Concha, M. K. Dowd, E. D. Stevens, Electron (charge) density studies of cellulose models. *Cellulose* **21**, 1051-1063 (2014).
64. R. Parthasarathi *et al.*, Insights into Hydrogen Bonding and Stacking Interactions in Cellulose. *J. Phys. Chem. A* **115**, 14191-14202 (2011).
65. U. Hirn, R. Schennach, Comprehensive analysis of individual pulp fiber bonds quantifies the mechanisms of fiber bonding in paper. *Sci Rep* **5**, 9 (2015).
66. R. Pelton, On the design of polymers for increased paper dry strength - A review. *Appita J.* **57**, 181-190 (2004).
67. P. Przybysz, M. Dubowik, M. A. Kucner, K. Przybysz, K. Przybysz Buzala, Contribution of Hydrogen Bonds to Paper Strength Properties. *Plos One* **11**, 10 (2016).
68. A. K. Vainio, General principles of adhesion with particular reference to the hydrogen bond. *F. Bolam Trans. 2nd Fund. Res. Symp. Oxford*, 119-130 (1961).
69. F. J. Schmied *et al.*, What holds paper together: Nanometre scale exploration of bonding between paper fibres. *Sci Rep* **3**, 6 (2013).
70. R. A. a. C. Stratton, N.L., Dependence of fibre/fibre bonding on some papermaking variables. *IPST Technical Paper Series* **357** (1990).
71. V. D. Papierfabriken, *Papier machen* ((2020).
72. D. T. Campbell, D. W. Fiske, CONVERGENT AND DISCRIMINANT VALIDATION BY THE MULTITRAIT-MULTIMETHOD MATRIX. *Psychol. Bull.* **56**, 81-105 (1959).
73. B. W. T. W. N. Kermann, First practical results using new high efficiency synthetic dry strength agents. *Wochenbl Papierfabr* **137**, 711-715 (2009).
74. G. Binnig, H. Rohrer, C. Gerber, E. Weibel, TUNNELING THROUGH A CONTROLLABLE VACUUM GAP. *Applied Physics Letters* **40**, 178-180 (1982).
75. D. W. Pohl, W. Denk, M. Lanz, OPTICAL STETHOSCOPY - IMAGE RECORDING WITH RESOLUTION LAMBDA/20. *Applied Physics Letters* **44**, 651-653 (1984).

76. R. Garcia, Amplitude Modulation Atomic Force Microscopy. *Wiley-VCH, Weinheim, Germany* (2010).
77. J. E. Sader, J. W. M. Chon, P. Mulvaney, Calibration of rectangular atomic force microscope cantilevers. *Rev. Sci. Instrum.* **70**, 3967-3969 (1999).
78. J. L. Hutter, J. Bechhoefer, CALIBRATION OF ATOMIC-FORCE MICROSCOPE TIPS. *Rev. Sci. Instrum.* **64**, 1868-1873 (1993).
79. N. F. Martinez, R. Garcia, Measuring phase shifts and energy dissipation with amplitude modulation atomic force microscopy. *Nanotechnology* **17**, S167-S172 (2006).
80. J. P. Cleveland, B. Anczykowski, A. E. Schmid, V. B. Elings, Energy dissipation in tapping-mode atomic force microscopy. *Applied Physics Letters* **72**, 2613-2615 (1998).
81. R. Garcia *et al.*, Identification of nanoscale dissipation processes by dynamic atomic force microscopy. *Physical Review Letters* **97**, 4 (2006).
82. P. Trtik, J. Kaufmann, U. Volz, On the use of peak-force tapping atomic force microscopy for quantification of the local elastic modulus in hardened cement paste. *Cem. Concr. Res.* **42**, 215-221 (2012).
83. N. E. B. Pittenger, and C. Su, Quantitative mechanical property mapping at the nanoscale with Peak-Force QNM. *Application Note 128, Bruker Nano Surfaces Division* (2012).
84. A. S. B. Pittenger, A. Berquand, P. Milani, A. Boudaoud, O. Hamant, and M. Radmacher, Toward quantitative nanomechanical measurements on live cells with peakforce QNM. *Application Note 141, Bruker Nano Surfaces Division* (2013).
85. B. V. Derjaguin, V. M. Muller, Y. P. Toporov, Effect of contact deformations on adhesion of particles. *Journal of Colloid and Interface Science* **53**, 314-326 (1975).
86. H. Hertz, Über die Berührung fester elastischer Körper (on the contact of elastic solids),. *Journal für die reine und angewandte Mathematik* **92**, 156-171 (1881).
87. K. L. Johnson, K. Kendall, A. D. Roberts, SURFACE ENERGY AND CONTACT OF ELASTIC SOLIDS. *Proceedings of the Royal Society of London Series a-Mathematical and Physical Sciences* **324**, 301-& (1971).
88. E. Placidi, Introduction to Atomic Force Microscopy. **ISBN: 978-0-224-62108-7** (2017).
89. L. Stuhn, A. Fritschen, J. Choy, M. Dehnert, C. Dietz, Nanomechanical sub-surface mapping of living biological cells by force microscopy. *Nanoscale* **11**, 13089-13097 (2019).
90. K. Sumetpipat, D. Baowan, B. J. Cox, J. M. Hill, Mathematical methods on atomic force microscope cantilever systems. *RSC Adv.* **6**, 46658-46667 (2016).
91. K. L. Westra, A. W. Mitchell, D. J. Thomson, TIP ARTIFACTS IN ATOMIC-FORCE MICROSCOPE IMAGING OF THIN-FILM SURFACES. *J. Appl. Phys.* **74**, 3608-3610 (1993).
92. T. R. Albrecht, S. Akamine, T. E. Carver, C. F. Quate, MICROFABRICATION OF CANTILEVER STYLI FOR THE ATOMIC FORCE MICROSCOPE. *J. Vac. Sci. Technol. A-Vac. Surf. Films* **8**, 3386-3396 (1990).
93. K. Raman C., K., The Optical Analogue of the Compton Effect. *Nature* **121**, 711 (1928).
94. C. Raman, A Change of Wave-length in Light Scattering. *Nature* **121**, 611 (1928).
95. E. Ruska, Ernst Ruska autobiography. *Nobel Foundation, Stockholm* (1986).
96. B. A. Jayne, Mechanische Eigenschaften von Holzfaser *Tappi J.* **42**, 416-467 (1959).
97. D. H. Page, F. Elhosseiny, K. Winkler, A. P. S. Lancaster, Elastic-modulus of sible wood pulp fibres. *Tappi* **60**, 114-117 (1977).
98. C. Lorbach, W. J. Fischer, A. Gregorova, U. Hirn, W. Bauer, Pulp Fiber Bending Stiffness in Wet and Dry State Measured from Moment of Inertia and Modulus of Elasticity. *BioResources* **9**, 5511-5528 (2014).

99. L. Groom, L. Mott, S. Shaler, Mechanical properties of individual southern pine fibers. Part I. Determination and variability of stress-strain curves with respect to tree height and juvenility. *Wood Fiber Sci.* **34**, 14-27 (2002).
100. S. Fernando, C. F. Mallinson, C. Phanopolous, D. A. Jesson, J. F. Watts, Mechanical characterisation of fibres for engineered wood products: a scanning force microscopy study. *J. Mater. Sci.* **52**, 5072-5082 (2017).
101. J. Müssig, *Industrial application of natural fibres* (Wiley, Chichester, West Sussex, U.K, 2010).
102. L. G. Samuelsson, Measurement of the stiffness of fibres. *Sven. Papperstidn.-Nord. Cellul.* **66**, 541-546 (1963).
103. D. B. Yan, K. C. Li, Wet fiber shear flexibility and its contribution to the overall transverse deformation of fibers. *J. Mater. Sci.* **43**, 7210-7218 (2008).
104. R. A. Forgacs OL, Mason SG, The hydrodynamic behaviour of paper-making fibres. *Pulp Pap Mag* **59**, 117-128 (1958).
105. F. O. Arlov AP, Mason SG, Particle motions in sheared suspensions. *Sven. Papperstidn.-Nord. Cellul.* **61**, 61-67 (1958).
106. N. Navaranjan, R. J. Blaikie, A. N. Parbhu, J. D. Richardson, A. R. Dickson, Atomic force microscopy for the measurement of flexibility of single softwood pulp fibres. *J. Mater. Sci.* **43**, 4323-4329 (2008).
107. T. Pettersson, J. Hellwig, P. J. Gustafsson, S. Stenstrom, Measurement of the flexibility of wet cellulose fibres using atomic force microscopy. *Cellulose* **24**, 4139-4149 (2017).
108. A. P. Schniewind, G. Ifju, D. L. and Brink, Effect of drying on the flexural rigidity of single fibres. *in: Consolidation of the Paper Web* **1**, 538-543 (1966).
109. N. L. Salmen, E. L. Back, Moisture-dependent thermal softening of paper, evaluated by its elastic-modulus. *Tappi* **63**, 117-120 (1980).
110. V. Placet, O. Cisse, M. L. Boubakar, Influence of environmental relative humidity on the tensile and rotational behaviour of hemp fibres. *J. Mater. Sci.* **47**, 3435-3446 (2012).
111. C. Ganser *et al.*, The effects of water uptake on mechanical properties of viscose fibers. *Cellulose* **22**, 2777-2786 (2015).
112. J. Hellwig, V. L. Duran, T. Pettersson, Measuring elasticity of wet cellulose fibres with AFM using indentation and a linearized Hertz model. *Anal. Methods* **10**, 5 (2018).
113. J. Auernhammer *et al.*, Nanomechanical characterisation of a water-repelling terpolymer coating of cellulosic fibres. *Cellulose* 10.1007/s10570-020-03675-9 (2021).
114. C. Czibula, C. Ganser, T. Seidlhofer, C. Teichert, U. Hirn, Transverse viscoelastic properties of pulp fibers investigated with an atomic force microscopy method. *J. Mater. Sci.* **54**, 11448-11461 (2019).
115. J. Hellwig, R. M. P. Karlsson, L. Wagberg, T. Pettersson, Measuring elasticity of wet cellulose beads with an AFM colloidal probe using a linearized DMT model. *Anal. Methods* **9**, 4019-4022 (2017).
116. M. Jajcinovic, W. J. Fischer, A. Mautner, W. Bauer, U. Hirn, Influence of relative humidity on the strength of hardwood and softwood pulp fibres and fibre to fibre joints. *Cellulose* **25**, 2681-2690 (2018).
117. O. A. El Seoud, L. C. Fidale, N. Ruiz, M. L. O. D'Almeida, E. Frollini, Cellulose swelling by protic solvents: which properties of the biopolymer and the solvent matter? *Cellulose* **15**, 371-392 (2008).
118. G. Buschlediller, S. H. Zeronian, Enhancing the reactivity and strength of cotton fibres. *Journal of Applied Polymer Science* **45**, 967-979 (1992).
119. G. I. Mantanis, R. A. Young, R. M. Rowell, Swelling of compressed cellulose fibre webs in organic liquids. *Cellulose* **2**, 1-22 (1995).
120. S. Biswas, Q. Ahsan, A. Genna, M. Hasan, A. Hassan, Physical and Mechanical Properties of Jute, Bamboo and Coir Natural Fiber. *Fiber. Polym.* **14**, 1762-1767 (2013).
121. J. M. Chard, G. Creech, D. A. Jesson, P. A. Smith, Green composites: sustainability and mechanical performance. *Plast. Rubber Compos.* **42**, 421-426 (2013).

122. B. Lin, Humidity Influence on Mechanics and Failure of Paper Materials: Joint Numerical and Experimental Study on Fiber and Fiber Network Scale. *arXiv submit/3516584 identifier 2012.08597* (2020).
123. F. J. Schmied *et al.*, What holds paper together: Nanometre scale exploration of bonding between paper fibres. *Sci Rep* **3** (2013).
124. F. J. Schmied, C. Teichert, L. Kappel, U. Hirn, R. Schennach, Joint strength measurements of individual fiber-fiber bonds: An atomic force microscopy based method. *Rev. Sci. Instrum.* **83**, 8 (2012).
125. H. J. Butt, M. Jaschke, CALCULATION OF THERMAL NOISE IN ATOMIC-FORCE MICROSCOPY. *Nanotechnology* **6**, 1-7 (1995).
126. N. Gavara, Combined strategies for optimal detection of the contact point in AFM force-indentation curves obtained on thin samples and adherent cells. *Sci Rep* **6**, 13 (2016).
127. R. Benitez, S. Moreno-flores, V. J. Bolos, J. L. Toca-Herrera, A new automatic contact point detection algorithm for AFM force curves. *Microsc. Res. Tech.* **76**, 870-876 (2013).
128. D. Rudoy, S. G. Yuen, R. D. Howe, P. J. Wolfe, Bayesian change-point analysis for atomic force microscopy and soft material indentation. *J. R. Stat. Soc. Ser. C-Appl. Stat.* **59**, 573-593 (2010).
129. D. C. Lin, E. K. Dimitriadis, F. Horkay, Robust strategies for automated AFM force curve analysis - I. Non-adhesive indentation of soft, inhomogeneous materials. *J. Biomech. Eng.-Trans. ASME* **129**, 430-440 (2007).
130. L. W. McKeen, L. W. McKeen, *THE EFFECT OF CREEP AND OTHER TIME RELATED FACTORS ON PLASTICS AND ELASTOMERS Foreword*, Effect of Creep and Other Time Related Factors on Plastics and Elastomers, 3rd Edition (Elsevier Science Bv, Amsterdam, 2015), pp. XI-XI.
131. J. R. Barber, A. Arbor, K. A., Contact Mechanics - Solid Mechanics and Its Applications. *Springer Verlag* **250** (2018).
132. AZoMaterials, Silica - Silicon Dioxide (SiO₂). <https://www.azom.com/properties.aspx?ArticleID=1114> **09. November 2020** (2020).
133. K. Elsayad *et al.*, Mechanical Properties of cellulose fibers measured by Brillouin spectroscopy. *Cellulose* **27**, 4209-4220 (2020).
134. S. J. Eichhorn, R. J. Young, The Young's modulus of a microcrystalline cellulose. *Cellulose* **8**, 197-207 (2001).
135. K. Kolln *et al.*, Mechanical properties of cellulose fibres and wood. Orientational aspects in situ investigated with synchrotron radiation. *J. Synchrot. Radiat.* **12**, 739-744 (2005).
136. T. Nishino *et al.*, Elastic-modulus of the crystalline regions of cellulose triesters. *J. Polym. Sci. Pt. B-Polym. Phys.* **33**, 611-618 (1995).
137. B. Lin *et al.*, Humidity influence on mechanics of paper materials: joint numerical and experimental study on fiber and fiber network scale. *Cellulose* 10.1007/s10570-021-04355-y (2021).
138. R. E. Mark, P. P. Gillis, Relationship between fibre modulus and S₂ angle. *Tappi* **56**, 164-167 (1973).
139. L. Salmen, A. Deruvo, A model for the prediction of fibre elasticity. *Wood Fiber Sci.* **17**, 336-350 (1985).
140. J. R. Barnett, V. A. Bonham, Cellulose microfibril angle in the cell wall of wood fibres. *Biol. Rev.* **79**, 461-472 (2004).
141. A. V. Spokevicius *et al.*, beta-tubulin affects cellulose microfibril orientation in plant secondary fibre cell walls. *Plant J.* **51**, 717-726 (2007).
142. A. Bergander, L. Salmen, Variations in transverse fibre wall properties: Relations between elastic properties and structure. *Holzforschung* **54**, 654-660 (2000).

143. R. Wimmer, B. N. Lucas, T. Y. Tsui, W. C. Oliver, Longitudinal hardness and Young's modulus of spruce tracheid secondary walls using nanoindentation technique. *Wood Sci. Technol.* **31**, 131-141 (1997).
144. W. Gindl, T. Schoberl, The significance of the elastic modulus of wood cell walls obtained from nanoindentation measurements. *Compos. Pt. A-Appl. Sci. Manuf.* **35**, 1345-1349 (2004).
145. W. J. Fischer *et al.*, Imaging of the formerly bonded area of individual fibre to fibre joints with SEM and AFM. *Cellulose* **21**, 251-260 (2014).
146. G. Piantanida, M. Bicchieri, C. Coluzza, Atomic force microscopy characterization of the ageing of pure cellulose paper. *Polymer* **46**, 12313-12321 (2005).
147. C. Roduit *et al.*, Stiffness Tomography by Atomic Force Microscopy. *Biophysical Journal* **97**, 674-677 (2009).
148. M. Dehnert, R. Magerle, 3D depth profiling of the interaction between an AFM tip and fluid polymer solutions. *Nanoscale* **10**, 5695-5707 (2018).
149. G. Longo *et al.*, Antibiotic-induced modifications of the stiffness of bacterial membranes. *J. Microbiol. Methods* **93**, 80-84 (2013).
150. M. Dehnert, E. C. Spitzner, F. Beckert, C. Friedrich, R. Magerle, Subsurface Imaging of Functionalized and Polymer-Grafted Graphene Oxide. *Macromolecules* **49**, 7415-7425 (2016).
151. R. Magerle, M. Dehnert, D. Voigt, A. Bernstein, Nanomechanical 3D Depth Profiling of Collagen Fibrils in Native Tendon. *Anal. Chem.* **92**, 8741-8749 (2020).
152. F. Carstens, J. A. F. Gamelas, S. Schabel, Engineering microfluidic papers: determination of fibre source and paper sheet properties and their influence on capillary-driven fluid flow. *Cellulose* **24**, 295-309 (2017).
153. M. A. Hubbe, A. Ayoub, J. S. Daystar, R. A. Venditti, J. J. Pawlak, Enhanced Absorbent Products Incorporating Cellulose and Its Derivatives: A Review. *BioResources* **8**, 6556-+ (2013).
154. K. Olejnik, Effect of the Free Swelling of Refined Cellulose Fibres on the Mechanical Properties of Paper. *Fibres & Textiles in Eastern Europe* **20**, 113-116 (2012).
155. D. Necas, P. Klapetek, Gwyddion: an open-source software for SPM data analysis. *Cent. Eur. J. Phys.* **10**, 181-188 (2012).
156. B. O. Community, Blender - a 3D modelling and rendering package. *Blender Foundation* (2018).
157. A. W. Blake *et al.*, Understanding the biological rationale for the diversity of cellulose-directed carbohydrate-binding modules in prokaryotic enzymes. *J. Biol. Chem.* **281**, 29321-29329 (2006).
158. J. M. Fox *et al.*, A single-molecule analysis reveals morphological targets for cellulase synergy. *Nature Chemical Biology* **9**, 356-+ (2013).
159. I. Venditto *et al.*, Complexity of the *Ruminococcus flavefaciens* cellulosome reflects an expansion in glycan recognition. *Proceedings of the National Academy of Sciences of the United States of America* **113**, 7136-7141 (2016).
160. O. Yaniv *et al.*, Structure of a family 3a carbohydrate-binding module from the cellulosomal scaffoldin CipA of *Clostridium thermocellum* with flanking linkers: implications for cellulosome structure. *Acta Crystallogr. F-Struct. Biol. Commun.* **69**, 733-737 (2013).
161. M. Beauregard, Meddeb-mouelhi, F., Hebert-ouellet, Y., Janse, B. and Macdonald, K. J., Polymer Probes And Methods. *US Patent* (2017).
162. M. M. Hartzell-Lawson, Y. L. Hsieh, Characterizing the noncellulosics in developing cotton fibers. *Text. Res. J.* **70**, 810-819 (2000).
163. M. E. Dokukin, I. Sokolov, On the Measurements of Rigidity Modulus of Soft Materials in Nanoindentation Experiments at Small Depth. *Macromolecules* **45**, 4277-4288 (2012).

164. M. Jocher, M. Gattermayer, H. J. Kleebe, S. Kleemann, M. Biesalski, Enhancing the wet strength of lignocellulosic fibrous networks using photo-crosslinkable polymers. *Cellulose* **22**, 581-591 (2015).
165. P. Chauhan, A. Kumar, B. Bhushan, Self-cleaning, stain-resistant and anti-bacterial superhydrophobic cotton fabric prepared by simple immersion technique. *Journal of Colloid and Interface Science* **535**, 66-74 (2019).
166. B. K. Tudu, A. Kumar, B. Bhushan, Fabrication of superoleophobic cotton fabric for multi-purpose applications. *Philosophical Transactions of the Royal Society A* **377**, 20190129 (2019).
167. B. K. Tudu, A. Sinhamahapatra, A. Kumar, Surface Modification of Cotton Fabric Using TiO₂ Nanoparticles for Self-Cleaning, Oil-Water Separation, Antistain, Anti-Water Absorption, and Antibacterial Properties. *ACS Omega* **5**, 7850-7860 (2020).
168. M. Satapathy *et al.*, Fabrication of superhydrophobic and superoleophilic polymer composite coatings on cellulosic filter paper for oil-water separation. *Cellulose* **24**, 4405-4418 (2017).
169. P. Fechner *et al.*, Interaction of water with different cellulose ethers: a Raman spectroscopy and environmental scanning electron microscopy study. *Journal of pharmacy and pharmacology* **57**, 689-698 (2005).
170. P. Eronen, M. Osterberg, A. S. Jaaskelainen, Effect of alkaline treatment on cellulose supramolecular structure studied with combined confocal Raman spectroscopy and atomic force microscopy. *Cellulose* **16**, 167-178 (2009).
171. H. L. Li, K. Mystek, L. Wagberg, T. Pettersson, Development of mechanical properties of regenerated cellulose beads during drying as investigated by atomic force microscopy. *Soft Matter* **16**, 6457-6462 (2020).
172. N. Chhabra, J. Spelt, C. M. Yip, M. T. Kortschot, An investigation of pulp fibre surfaces by atomic force microscopy. *J. Pulp Pap. Sci.* **31**, 52-56 (2005).
173. R. B. Adusumalli, W. M. Mook, R. Passas, P. Schwaller, J. Michler, Nanoindentation of single pulp fibre cell walls. *J. Mater. Sci.* **45**, 2558-2563 (2010).
174. W. C. Oliver, G. M. Pharr, AN IMPROVED TECHNIQUE FOR DETERMINING HARDNESS AND ELASTIC-MODULUS USING LOAD AND DISPLACEMENT SENSING INDENTATION EXPERIMENTS. *J. Mater. Res.* **7**, 1564-1583 (1992).
175. D. B. Yan, K. C. Li, Conformability of wood fiber surface determined by AFM indentation. *J. Mater. Sci.* **48**, 322-331 (2013).
176. C. Ganser, U. Hirn, S. Rohm, R. Schennach, C. Teichert, AFM nanoindentation of pulp fibers and thin cellulose films at varying relative humidity. *Holzforschung* **68**, 53-60 (2014).
177. A. Böhm, M. Gattermayer, F. Carstens (2013) Designing microfabricated paper devices through tailored polymer attachment. in *I'Anson Sj Trans XVth Fundam Res Symp*, pp 599-618.
178. S. Wendenburg, M. L. Nachbar, M. Biesalski, Tailoring the Retention of Charged Model Compounds in Polymer Functionalized Paper-Based Microfluidic Devices. *Macromol. Chem. Phys.* **218** (2017).
179. M. Osterberg, U. Schmidt, A. S. Jaaskelainen, Combining confocal Raman spectroscopy and atomic force microscopy to study wood extractives on cellulose surfaces. *Colloid Surface A* **291**, 197-201 (2006).
180. N. Brun *et al.*, In situ monitoring of styrene polymerization using Raman spectroscopy. Multi-scale approach of homogeneous and heterogeneous polymerization processes. *J Raman Spectrosc* **44**, 909-915 (2013).
181. P. P. Hong, F. J. Boerio, S. J. Clarson, S. D. Smith, An Investigation of the Interdiffusion of Polystyrene and Deuterated Polystyrene Using Surface-Enhanced Raman-Scattering. *Macromolecules* **24**, 4770-4776 (1991).
182. L. Babkov, J. Baran, N. Davydova, V. Mel'nik, K. Uspenskiy, Raman spectra of metastable phase of benzophenone. *Journal of molecular structure* **792**, 73-77 (2006).

-
183. Y. Xie *et al.*, Sensing of polycyclic aromatic hydrocarbons with cyclodextrin inclusion complexes on silver nanoparticles by surface-enhanced Raman scattering. *Analyst* **135**, 1389-1394 (2010).
 184. C. Baley, Analysis of the flax fibres tensile behaviour and analysis of the tensile stiffness increase. *Composites Part A: Applied Science and Manufacturing* **33**, 939-948 (2002).
 185. J. Gassan, A. Chate, A. K. Bledzki, Calculation of elastic properties of natural fibers. *J. Mater. Sci.* **36**, 3715-3720 (2001).
 186. B. V. Derjaguin, V. M. Muller, Y. P. Toporov, EFFECT OF CONTACT DEFORMATIONS ON ADHESION OF PARTICLES. *J. Colloid Interface Sci.* **53**, 314-326 (1975).
 187. B. N. J. Persson *et al.*, Adhesion of cellulose fibers in paper. *J Phys-Condens Mat* **25** (2013).
 188. A. Torgnysdotter, L. Wagberg, Tailoring of fibre/fibre joints in order to avoid the negative impacts of drying on paper properties. *Nord. Pulp Paper Res. J.* **21**, 411-418 (2006).
 189. J. Mayhood, O. Kallmes, and M. Cauley, *Tappi* **45** (1962).
 190. J. L. Schäfer *et al.*, Accessibility of fiber surface sites for polymeric additives determines dry and wet tensile strength of paper sheets. *Cellulose* **28**, 5775-5791 (2021).
 191. J. Auernhammer *et al.*, Mapping humidity-dependent mechanical properties of a single cellulose fibre. *Cellulose* 10.1007/s10570-021-04058-4 (2021).

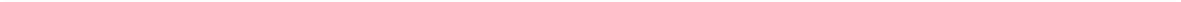




12 Publications

- **Stühn, L***, **Auernhammer, J.*** & Dietz, C. pH-depended protein shell dis- and reassembly of ferritin nanoparticles revealed by atomic force microscopy. *Sci Rep* **9**, 17755 (2019). <https://doi.org/10.1038/s41598-019-53943-3>
- **Auernhammer, J.***, **Bell, A.K***, Schulze, M. *et al.* Nanomechanical characterisation of a water-repelling terpolymer coating of cellulosic fibres. *Cellulose* **28**, 2149–2165 (2021). <https://doi.org/10.1007/s10570-020-03675-9>
- **Auernhammer, J.**, Keil, T., Lin, B. *et al.* Mapping humidity-dependent mechanical properties of a single cellulose fibre. *Cellulose* **28**, 8313–8332 (2021). <https://doi.org/10.1007/s10570-021-04058-4>
- **Auernhammer, J.**, Stark, RW. Mechanical characterisation of single cellulosic fibres. *Paper Technology International Journal, December 2021 release*
- **Auernhammer, J.**, Langhans, M., Schäfer JL. *et al.* Nanomechanical subsurface characterisation of cellulosic fibres. *Springer Nature Applied Sciences - Under Review*
- **Lin, B.**, **Auernhammer, J.**, Schäfer, JL. *et al.* Humidity influence on mechanics of paper materials: joint numerical and experimental study on fiber and fiber network scale. *Cellulose* (2021). <https://doi.org/10.1007/s10570-021-04355-y>

*Contributed equally to this work



13 Acknowledgement

Zuerst möchte ich mich bei Robert Stark bedanken!

Vielen Dank, dass du es mir ermöglicht hast in deine Gruppe zu promovieren!

Besonders bedanke ich mich für die tolle Unterstützung beim wissenschaftlichen Arbeiten und Schreiben. Dadurch habe ich unglaublich viel gelernt, unter anderem Sachverhalte präzise und korrekt auszudrücken.

Außerdem war mir immer ein sehr angenehmes Arbeitsumfeld gegeben!

Vielen Dank!

Vielen Dank auch an meine weiteren Prüferinnen und Prüfer, die sich für mich die Zeit genommen haben.

Danke an Regine von Klitzing, Karsten Durst und Wolfgang Ensinger!

Dann möchte ich mich bei der gesamten „Physics of Surfaces“ Gruppe bedanken!

Vielen Dank für eure ganze Unterstützung in den letzten Jahren – egal wie diese mir entgegengebracht wurde!

Weiterhin danke ich meinen Kooperationspartnern im ganzen FiPre Projekt!

Durch viele spannende Diskussionen sind so viele neue Erkenntnisse entstanden, die ohne euch nicht möglich gewesen wären!

Last but not least:

Ich bedanke mich bei meiner Familie und natürlich meinem gesamten Freundeskreis für jegliche Unterstützung – und das quasi schon immer!

Der Dank für die finanzielle Unterstützung geht an die Deutsche Forschungsgemeinschaft (DFG). Das Projekt wurde im FiPre PAK Projekt unter der Sachbeihilfe STA1026/8-1 gefördert.

